

博士論文

Doctoral Dissertation

Time Dependent Charge-Parity Violation in $B^0 \rightarrow K_s^0 K_s^0 K_s^0$ in Belle

II early operation

(Belle II 初期データを使った $B^0 \rightarrow K_S^0 K_S^0 K_S^0$ 崩壊の時間に依存する
荷電・パリティ非保存の研究)

令和2年12月博士(理学)申請

A Dissertation Submitted for the Degree of Doctor of Philosophy

December 22nd, 2020

東京大学大学院理学系研究科物理学専攻

Department of Physics, Graduate School of Science,
The University of Tokyo

万 琏

Wan Kun

**Time Dependent Charge-Parity Violation in $B^0 \rightarrow K_s^0 K_s^0 K_s^0$ in
Belle II early operation**

by

Kun Wan

Submitted to the Department of Physics
on December 22nd, 2020, in partial fulfillment of the
requirements for the degree of
Doctor of Philosophy

Abstract

Belle II experiment is a next-generation super B-factory experiment. The targeted instantaneous luminosity is $8 \times 10^{35} \text{ cm}^{-2}\text{s}^{-1}$ and the expected integrated luminosity is 50 ab^{-1} by 2030 with the majority of data collected at the $\Upsilon(4S)$ resonance using SuperKEKB accelerator.

The thesis is based on the time-dependent CP violation study of $B^0 \rightarrow K_S^0 K_S^0 K_S^0$ decay to precisely measure the CP parameters \mathcal{S} and \mathcal{A} in penguin-dominated $b \rightarrow s$ transition, which is sensitive to New Physics effects. Such a precise measurement mainly depends on determination of the distance between two vertices of two neutral B mesons. The blind analysis and fit by a unbinned maximum likelihood method are performed using about 62.8 fb^{-1} recorded experiment data from Belle II detector 2019 and 2020 (spring and summer) operation. The measurement results: $\mathcal{S} = -\sin(2\phi_1) = -0.82 \pm 0.85 \text{ (stat)} \pm 0.07 \text{ (syst)}$ and $\mathcal{A} = -0.21 \pm 0.28 \text{ (stat)} \pm 0.06 \text{ (syst)}$ are obtained.

Thesis Supervisor: Hiroaki Aihara

Title: Professor

Contents

1	Introduction	9
1.1	The Standard Model	9
1.2	Symmetry Violation	10
1.3	CKM mechanism	12
1.4	Time Dependent CP violation	17
1.4.1	CP violation in neutral B system	17
1.4.2	ϕ_1 from $B^0 \rightarrow J/\psi K_S^0$	20
1.4.3	ϕ_1 from penguin-dominated mode $b \rightarrow q\bar{q}s$	21
1.4.4	ϕ_1 from $B^0 \rightarrow K_S^0 K_S^0 K_S^0$	22
2	Belle II experiment	25
2.1	Belle II and SuperKEKB overview	25
2.2	Vertex detector (VXD)	27
2.3	Central drift chamber (CDC)	29
2.4	TOP and ARICH detectors	30
2.5	Electromagnetic calorimeter (ECL)	32
2.6	K_L^0 muon detector (KLM)	33
2.7	Trigger and DAQ system	33
2.8	Analysis Software	35
2.8.1	BASF2 Core Structure	36
2.8.2	Event Processing Workflow	37
2.8.3	mDST structure	39
2.8.4	Conditional Database	40

2.9	Belle II simulation	42
2.10	Belle II data taking	45
3	K_S^0 reconstruction study	47
3.1	Cut-based K_S^0 Reconstruction	48
3.2	MVA-based K_S^0 Identification: KsFinder	51
3.2.1	Belle II K_S^0 classification	51
3.2.2	FastBDT algorithm	54
3.2.3	Decay Topology of $K_S^0 \rightarrow \pi^+ \pi^-$	56
3.2.4	Determination of training observables from K_S^0 decay	58
3.2.5	Training, Applying and Testing of KsFinder	60
3.2.6	The Performance and Over-fitting check	62
3.2.7	Data Validation for Classifier	65
3.2.8	KsFinder Effects on Kinematics Evaluation	67
4	Analysis strategies	71
4.1	Data Sample and Event Selection	71
4.1.1	K_S^0 Selection	71
4.1.2	B^0 Reconstruction	74
4.1.3	Continuum Suppression	75
4.1.4	Resonance Background	82
4.1.5	$B\bar{B}$ background and self-cross feed	83
4.1.6	Signal Extraction	83
4.1.7	Kinematics and Vertexing Dependence on KsFinder	88
5	CP parameters measurement	97
5.1	Vertex Resolution Model	98
5.1.1	CP -side resolution function	99
5.1.2	Tag-side resolution function	100
5.1.3	Background events Δt distribution	104
5.2	Flavor Tagging	105

5.3	<i>CP</i> Fitter	107
5.4	Blind analysis and fit	108
5.4.1	<i>CP</i> fit on MC samples	108
5.4.2	Linearity Test	110
5.4.3	Toy MC Fit Pull	111
5.4.4	Lifetime and Δm_d Fit	112
5.5	<i>CP</i> fit on data	114
5.6	Systematic Uncertainty	114
6	Conclusion and Prospect	119
A	Training Observables for K_S^0 Classifier	123
B	Data Validation Plots for K_S^0	127
C	K_S^0 mass fit with varied cut value	131
D	$2K_S^0$ invariant mass distribution	137

Chapter 1

Introduction

1.1 The Standard Model

The Standard Model (SM) was built in the late 70th of 20th century to describe the matter compositions and interactions using a group of fundamental particles - fermions and bosons. In the Standard Model, there are three generations of quarks and leptons, along with their anti-particles, which are all fermions. On the other hand, the bosons in the Standard Model consist of gluons, photons, W^\pm and Z^0 bosons that are all gauge bosons and one Higgs boson that is a scalar boson. This group of particles are summarized in Figure 1-1. The Standard Model depicts the interactions between elementary particles as the exchange of the bosons. The strong interaction requires the exchange of gluons. Photons, W^\pm and Z^0 bosons carry the electromagnetic force and weak force, which are unified as electroweak interaction in the Standard Model. Higgs boson is responsible for the generation of masses for the gauge bosons through electroweak symmetry breaking[1]. The Standard Model has been proved to be an excellent theoretical model that can be used to explain many experimental observations, but sadly not all of them. For instance, neutrino mass is expected to be zero in the Standard Model but the flavor oscillation indicates non-zero mass of neutrinos. The observation of Charge-Parity (CP) asymmetry in universe presented by the absence of antimatter can not be fully explained by the CP violation sources within the Standard Model. These experimental observations

require further researches beyond the Standard Model, which is called New Physics (NP) studies.

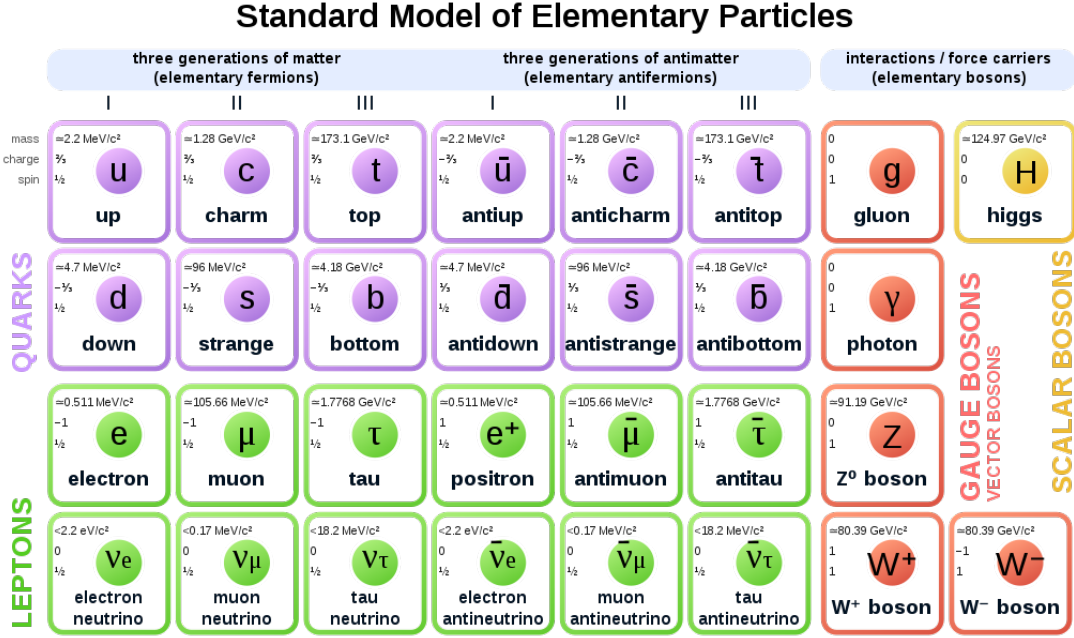


Figure 1-1: Elementary particles in the Standard Model.[2]

1.2 Symmetry Violation

Symmetry violation has been one of the focuses in NP studies due to the internal link between symmetries and conservation laws, which makes it a good probe for possible NP theories beyond the SM. When a known symmetry is found to be broken, it usually leads to the discovery of a new theory.

There are three types of discrete symmetric operations which play important roles in particle physics. Charge-conjugation C is the operation that turns particle to its anti-particle. Parity transformation P is the one that puts a negative sign before all the spatial related vector such as $\vec{r} \rightarrow -\vec{r}$. The time-reversing operation T is to reversely proceed a physical process backward time. Physicists were convinced that each of these three symmetric operations makes no change to any physics system. However, in 1950s, Lee and Yang [3] first questioned that parity symmetry might be

broken in weak interactions. They offered a few possible ways to test it and then by Wu [4], an observation on the β decay of ^{60}Co was presented that the electrons emitted from ^{60}Co decay prefer the direction of nuclear spin that can be controlled by the external magnetic field. The violation of P symmetry was discovered by this clear evidence.

The first evidence of CP violation was discovered in neutral K^0 system by Cronin and Fitch's experiment[5]. The neutral K^0 mesons can be observed as two states that have significantly different lifetime (called as " K_S^0 " and " K_L^0 " for short and long lifetime particles) with opposite CP . The experiment measured the decay products at 57 foot of a neutral K^0 beamline assuming all the particle at the end of the beam should be long lifetime K_L^0 , nearly no K_S^0 . But 0.002% of K_L^0 were found to decay into $\pi^+\pi^-$ which is the main decay process of K_S^0 . ($CP = 1$ in $\pi^+\pi^-$ final states, while K_L has $CP = -1$). Given that the expected distance to have 0.002% of K_S^0 at about speed of light is no more than 1 meter in the beamline, such a deviation at 57 foot is an obvious evidence that $K_L^0 \rightarrow \pi^+\pi^-$ exists and therefore CP symmetry is violated in the neutral K^0 system.

In 1973, Kobayashi and Maskawa introduced a quark mixing matrix called CKM matrix for three or more generations of quarks before the discovery of the third generation of the quark family[6]. The theory naturally explained an irreducible complex phase in CKM matrix and it accounts for the origin of CP asymmetries of weak interactions in the Standard Model. The experimental evidence of CP violation in B meson system was observed in 2001 by Belle and Babar experiments[7][8]. They measured the time-dependent decay time difference of B and \bar{B} in the decay of $B \rightarrow J/\psi K_S^0$. This channel provided a good clearness in theoretical prediction and has relatively large branching fraction, thus it's called the "golden mode"[9]. In 2008, Kobayashi and Maskawa were rewarded the Nobel Prize to highly value their contribution to CP violation mechanism in the SM, to which Belle experiment contributes greatly. Later in 2010, the upgrade of Belle, Belle II and the upgrade of KEK accelerator, SuperKEKB, were approved to further push the understanding of CP violation along with other topics in New Physics researches.

1.3 CKM mechanism

$$\Phi = \begin{pmatrix} \phi^+ \\ \nu + \frac{H+i\chi}{\sqrt{2}} \end{pmatrix} \quad (1.1)$$

Equation 1.1 is the Higgs potential doublets in the SM, where the value of H is 174 GeV as the expected Higgs potential for vacuum[10]. The ϕ and χ are the psuedo-Goldstone fields which are appearing when introducing Higgs field ϕ without breaking the gauge symmetry. The Lagrangian for Yukawa interaction of the quark fields[11] can be presented by Equation 1.2.

$$\mathcal{L}_{Yuk}^q = -Q^\dagger Y^d \Phi d'_R - Q^\dagger Y^u \epsilon \Phi^* u'_R + h.c. \quad (1.2)$$

where the primed fields stand for the weak eigenstates of quarks. The ϵ is a 2×2 matrix and Q^\dagger is the left-handed doublets that stand for weak eigenstates of up and down types quarks, see Equation 1.3 and 1.4.

$$\epsilon = \begin{pmatrix} 0 & 1 \\ -1 & 0 \end{pmatrix} \quad (1.3)$$

$$Q = \begin{pmatrix} u' & d' \\ c' & s' \\ t' & b' \end{pmatrix}_L \quad (1.4)$$

Yukawa matrix is an arbitrary 3×3 complex matrix $Y^{u,d}$ which gives the rise of up and down type massive quark field $M^{u,d} = Y^{u,d} \nu$ according to Equation 1.2. The representation of the quark fields using weak eigenstates can be transformed to mass eigenstates by Equation 1.5 and 1.6.

$$S_{L,R}^u \begin{pmatrix} u' \\ c' \\ t' \end{pmatrix}_{L,R} = \begin{pmatrix} u \\ c \\ t \end{pmatrix}_{L,R} \quad (1.5)$$

$$S_{L,R}^d \begin{pmatrix} d' \\ s' \\ b' \end{pmatrix}_{L,R} = \begin{pmatrix} d \\ s \\ b \end{pmatrix}_{L,R} \quad (1.6)$$

In Equation 1.5 and 1.6, $S_{L,R}^{u,d}$ are all unitary matrices since they are generated by the normalized eigenstate states of Yukawa matrix. The mass item in the Lagrangian can be presented as Equation 1.7

$$\mathcal{L}_m = - \sum_{q=u,c,t,d,s,b} M_q q^\dagger q \quad (1.7)$$

where the $q = (q_L + q_R)$ is four-component Dirac field, and $q_L^\dagger q_L = q_R^\dagger q_R = 0$. As a result of diagonalizing $Y^{u,d}$, the charged current W^\pm interactions couple to the physical quarks and the Lagrangian is written as Equation 1.8, where $V_{CKM} \equiv S_L^u S_L^{d\dagger}$.

$$\mathcal{L}_W^q = \frac{g}{\sqrt{2}} \left[\begin{pmatrix} \bar{u} & \bar{c} & \bar{t} \end{pmatrix}_L \gamma^\mu W_\mu^+ V_{CKM} \begin{pmatrix} d \\ s \\ b \end{pmatrix}_L + \begin{pmatrix} \bar{d} & \bar{s} & \bar{b} \end{pmatrix}_L \gamma^\mu W_\mu^- V_{CKM}^\dagger \begin{pmatrix} u \\ c \\ t \end{pmatrix}_L \right] \quad (1.8)$$

The Lagrangian hereby clearly declares the transition of different charged quarks through the coupling of charged current W^\pm , where such a coupling only applies for the left-handed quarks. For example, a left-handed charm quark only transits to left-handed strange quark by a W boson. By only applying C or P conjugation, the Lagrangian is not invariant, indicating the non-conservation of C or P individually. However, if the CP conjugation is applied, the Equation 1.8 transits as Equation 1.9 shows.

$$\begin{pmatrix} \bar{u} & \bar{c} & \bar{t} \end{pmatrix}_L \gamma^\mu W_\mu^+ V_{CKM} \begin{pmatrix} d \\ s \\ b \end{pmatrix}_L \Leftrightarrow \begin{pmatrix} u & c & t \end{pmatrix}_L \gamma^\mu W_\mu^- V_{CKM} \begin{pmatrix} \bar{d} \\ \bar{s} \\ \bar{b} \end{pmatrix}_L \quad (1.9)$$

Comparing Equation 1.9 and 1.8, the CP symmetry requires the invariance before and after CP conjugation, meaning that Equation 1.10 is expected.

$$u_L^i V_{ij} \bar{d}_L^j \gamma^\mu W_\mu^- = u_L^n V_{nm}^* \bar{d}_L^m \gamma^\mu W_\mu^- \quad (1.10)$$

The same indices ij and nm are summed over on both side. This is equivalent to Equation 1.11:

$$V_{ij} = V_{ij}^* \quad (1.11)$$

On the one hand, if the CKM matrix is real, CP will be conserved in the weak interaction in the SM due to the natural hold of Equation 1.11. On the other hand, from Equation 1.10, it's still possible to make Lagrangian invariant even if V_{CKM} is not real, which can be achieved by introducing non-physical phases for each quark field $u_L^k e^{(i\phi_{uk})}$ and $d_L^j e^{(i\phi_{dj})}$, the Equation 1.11 becomes Equation 1.12.

$$V_{kj} e^{i(\phi_{dj} - \phi_{uk})} = V_{kj}^* e^{i(\phi_{uk} - \phi_{dj})} \quad (1.12)$$

Assuming the complex phase of the kj -th element in CKM matrix is θ_{kj} , it's obviously required Equation 1.13 to be hold.

$$\theta_{kj} = \phi_{uk} - \phi_{dj} \quad (1.13)$$

If the number of generations in quark family is 3 or more, the non-physical phases can not render proper values to ensure the hold of Equation 1.13, and there will always be one irreducible complex phase parameter in the CKM matrix in the existence of 3 generations of quarks, which means CP symmetry is no longer conserved in the weak interactions.

The 3×3 unitary CKM matrix can be written as Equation 1.14 based on the

quark fields it connects using Equation 1.5 and 1.6.

$$V_{CKM} = \begin{pmatrix} V_{ud} & V_{us} & V_{ub} \\ V_{cd} & V_{cs} & V_{cb} \\ V_{td} & V_{ts} & V_{tb} \end{pmatrix} \quad (1.14)$$

It can be parameterized into the form of Equation 1.15.

$$V_{CKM} = \begin{pmatrix} c_{12}c_{13} & s_{12}c_{13} & s_{13}e^{-i\delta} \\ -s_{12}c_{23} - c_{12}s_{23}s_{13}e^{-i\delta} & c_{12}c_{23} - s_{12}s_{23}s_{13}e^{-i\delta} & s_{23}c_{13} \\ s_{12}s_{23} - c_{12}s_{23}s_{13}e^{-i\delta} & -c_{12}c_{23} - s_{12}s_{23}s_{13}e^{-i\delta} & c_{23}c_{13} \end{pmatrix} \quad (1.15)$$

where the $c_{jk} = \cos(\theta_{jk})$ and $s_{jk} = \sin(\theta_{jk})$, δ is the irreducible complex phase. By measuring the relative branching ratio of $b \rightarrow c$, $s \rightarrow u$ and $b \rightarrow u$ in a tree level transitions as shown in Equation 1.16.

$$|V_{ub}| \ll |V_{cb}| \ll |V_{us}| \quad (1.16)$$

and the relations in Equation 1.17 are often used to simplify CKM matrix presentation.

$$s_{13} = \lambda, s_{23} = A\lambda^2, s_{13}e^{i\delta} = A\lambda^3(\rho - i\eta) \quad (1.17)$$

By using Equation 1.17, CKM matrix is parameterized as Equation 1.18.

$$V_{CKM} = \begin{pmatrix} 1 - 1/2\lambda^2 & \lambda & A\lambda^3(\rho - i\eta) \\ -\lambda & 1 - 1/2\lambda^2 & A\lambda^2 \\ A\lambda^3(\rho - i\eta) & -A\lambda^2 & 1 \end{pmatrix} + \mathcal{O}(\lambda^4) \quad (1.18)$$

Using the unitary condition, the Equation 1.19 is obtained.

$$1 + \frac{V_{ud}V_{ub}^*}{V_{cd}V_{cb}^*} + \frac{V_{td}V_{tb}^*}{V_{cd}V_{cb}^*} = 0 \quad (1.19)$$

Using Equation 1.19, 1.20 and 1.21, the shape of CKM triangle can be defined on the

complex plane in Figure 1-2.

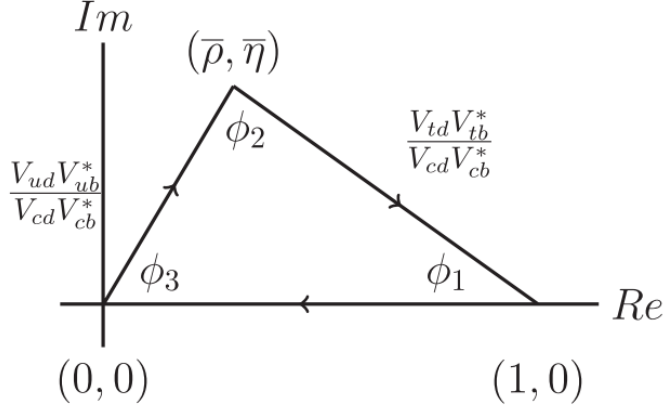


Figure 1-2: The unitary triangles of CKM[12].

$$\bar{\rho} + i\bar{\eta} = -\frac{V_{ud}V_{ub}^*}{V_{cd}V_{cb}^*} \quad (1.20)$$

$$1 - (\bar{\rho} + i\bar{\eta}) = -\frac{V_{td}V_{tb}^*}{V_{cd}V_{cb}^*} \quad (1.21)$$

These angles are obtained by drawing the $(\bar{\rho}, \bar{\eta})$ on the complex coordinates, and they are also well-known in the names as: $\phi_1 = \beta, \phi_2 = \alpha, \phi_3 = \gamma$. The results presenting the measurement of CKM angles or $(\bar{\rho}, \bar{\eta})$ in 2019 are shown in Figure 1-3.

The measurement of ϕ_1 and ϕ_2 are mainly obtained from the time-dependent CP violations (TDCPV) measurement. The ϕ_1 in the tree-level dominated decays has been precisely measured due to the small hadronic uncertainties. Flavor-Changing-Neutral-Current (FCNC) processes can rise through the $B_d^0 - \bar{B}_d^0$ mixing in box diagram, and it's believed that potential NP processes might contribute to the difference in between results of CKM angles measured from experiments, such as ϕ_1 value in tree-dominated processes and penguin-dominated processes, where both involve $b \rightarrow s$ transition. It requires the precise measurements on multiple decay channels to search for the potential NP effects. The prospective large Belle II data and improved detector performance will be much useful to help the discovery of NP in future.

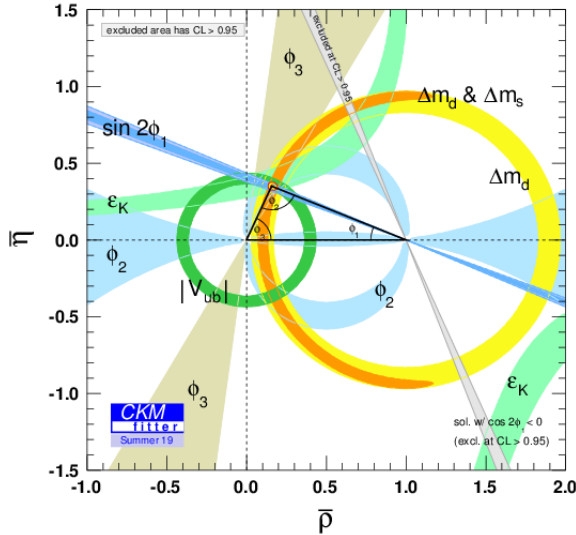


Figure 1-3: The CKM triangle fit in the complex plane of $\bar{\rho} - \bar{\eta}$.[12]

1.4 Time Dependent CP violation

1.4.1 CP violation in neutral B system

The ϕ_1 , ϕ_2 and ϕ_3 are essentially measuring the CKM CP violating phase since there's only one complex phase in the CKM matrix and it can be determined by these three angles. For determining the value of ϕ_1 , TDCPV measurements provide a good experimental environment. From Figure 1-2, one can obtain ϕ_1 and ϕ_2 by Equation 1.22 and 1.23.

$$\phi_1 = \text{Arg}\left(-\frac{V_{td}V_{tb}^*}{V_{cd}V_{cb}^*}\right) \quad (1.22)$$

$$\phi_2 = \text{Arg}\left(-\frac{V_{td}V_{tb}^*}{V_{ud}V_{ub}^*}\right) \quad (1.23)$$

The time-dependent CP violation comes from the interference of neutral B mixing phase and the weak phase in the decay amplitude. The mass eigenstates which are driving the propagation of neutral B meson states with mixing are: $|B\rangle_{H,L} = p|B\rangle \pm q|\bar{B}\rangle$, where H and L stand for the heavier and lighter mass eigenvalues. The $|B\rangle$ and $|\bar{B}\rangle$ present the flavor eigenstates of neutral B mesons. The Hamiltonian

matrix can be written using flavor eigenstates as shown in Equation 1.24.

$$M_\Gamma = \begin{bmatrix} m - i/2\Gamma & M_{12} - i/2\Gamma_{12} \\ M_{12}^* - i/2\Gamma_{12}^* & m - i/2\Gamma \end{bmatrix} \quad (1.24)$$

Considering the time evolution of mass eigenstates, the time-dependent states can be shown as Equation 1.25 and 1.26 by using the notation of $B_{H,L}$ as physical states at $t = 0$.

$$B_H(t) = e^{-im_H t} e^{-\Gamma_H t/2} B_H \quad (1.25)$$

$$B_L(t) = e^{-im_L t} e^{-\Gamma_L t/2} B_L \quad (1.26)$$

where $M_{H,L}$ and $\Gamma_{H,L}$ are the masses and decay width of two mass eigenstates. By expanding the mass eigenstates using flavor eigenstates, which are shown in Equation 1.27 and 1.28.

$$B(t) = (1/2p)e^{-im_H t} e^{-\Gamma_H t/2}(pB + q\bar{B}) + (1/2p)e^{-im_L t} e^{-\Gamma_L t/2}(pB - q\bar{B}) \quad (1.27)$$

$$\bar{B}(t) = (1/2q)e^{-im_H t} e^{-\Gamma_H t/2}(pB + q\bar{B}) - (1/2q)e^{-im_L t} e^{-\Gamma_L t/2}(pB - q\bar{B}) \quad (1.28)$$

Replacing $g_\pm(t) = \frac{1}{2}(e^{-im_H t - \Gamma_H/2t} \pm e^{-im_L t - \Gamma_L/2t})$, Equation 1.27 and 1.28 become Equation 1.29 and 1.30.

$$B(t) = g_+(t)B + \frac{q}{p}g_-(t)\bar{B} \quad (1.29)$$

$$\bar{B}(t) = g_+(t)\bar{B} + \frac{p}{q}g_-(t)B \quad (1.30)$$

Considering all the phase-spaces of the decay from flavor eigenstates to final states $f(\bar{f})$ are included in the amplitudes $\mathcal{A}_f(\bar{\mathcal{A}}_{\bar{f}})$, one needs to expand the flavor eigenstates using the final states amplitudes to have the differential decay rate $\Gamma(B \rightarrow f, t)$. From $B(t) \propto \mathcal{A}_f \psi_f + h.c$ and $(\bar{B}(t) \propto \bar{\mathcal{A}}_{\bar{f}} \psi_{\bar{f}} + h.c)$, combined with Equation 1.29 and

1.30, the decay rate can be shown in Equation 1.31 and 1.32.

$$\Gamma(B \rightarrow f, t) = |\mathcal{A}_f|(|g_+(t)|^2 + |\lambda_f|^2 |g_-(t)|^2 + 2\text{Re}(\lambda_f g_+^*(t) g_-(t))) \quad (1.31)$$

$$\Gamma(\bar{B} \rightarrow \bar{f}, t) = |\bar{\mathcal{A}}_f|(|g_+(t)|^2 + |\bar{\lambda}_{\bar{f}}|^2 |g_-(t)|^2 + 2\text{Re}(\bar{\lambda}_{\bar{f}} g_+^*(t) g_-(t))) \quad (1.32)$$

where the parameter λ_f and $\bar{\lambda}_{\bar{f}}$ can be defined as Equation 1.33 and 1.34.

$$\lambda_f \equiv (q/p)(\bar{\mathcal{A}}_f / \mathcal{A}_f) \quad (1.33)$$

$$\bar{\lambda}_{\bar{f}} \equiv (q/p)(\mathcal{A}_{\bar{f}} / \bar{\mathcal{A}}_{\bar{f}}) \quad (1.34)$$

The q/p is introduced by the coefficient of mass eigenstates from weak eigenstates. Using the Hamiltonian matrix, q/p can be presented using Equation 1.35

$$q/p = \frac{\Delta M - i/2\Delta\Gamma}{2(M_{12} - i/2\Gamma_{12})} \quad (1.35)$$

where the M_{12} and Γ_{12} stands for the contribution of non-diagnosed term in the Hamiltonian matirx. $\Delta M = M_H - M_L$ and $\Delta\Gamma = \Gamma_H - \Gamma_L$ are the difference of mass and decay width for two mass eigenstates, respectively. It's obvious that if $|\mathcal{A}_f| \neq |\bar{\mathcal{A}}_{\bar{f}}|$, direct CP violation will occur. The time-dependent decay rate difference is defined as Equation 1.36.

$$\begin{aligned} A_{CP}(t) &\equiv \frac{\Gamma(B \rightarrow f, t) - \Gamma(\bar{B} \rightarrow \bar{f}, t)}{\Gamma(B \rightarrow f, t) + \Gamma(\bar{B} \rightarrow \bar{f}, t)} \\ &= \frac{\mathcal{S}\sin(\Delta Mt) - \mathcal{A}\cos(\Delta Mt)}{\cosh(\Delta\Gamma t/2) + A_{\Delta\Gamma}^f \sinh(\Delta\Gamma t/2)} \end{aligned} \quad (1.36)$$

, where

$$\mathcal{S} = \frac{2\text{Im}(\lambda_f)}{1 + |\lambda_f|^2} \quad (1.37)$$

$$\mathcal{A} = \frac{1 - |\lambda_f|^2}{1 + |\lambda_f|^2} \quad (1.38)$$

$$A_{\Delta\Gamma}^f = -\frac{2\text{Re}(\lambda_f)}{1 + |\lambda_f|^2} \quad (1.39)$$

From Equation 1.37 and ??, the time-dependent CP violation parameters \mathcal{S} and \mathcal{A} are dependent on the parameter λ_f , which are determined by Equation 1.33.

1.4.2 ϕ_1 from $B^0 \rightarrow J/\psi K_S^0$

If final states are CP eigenstates, the amplitude is obtained by $\mathcal{A}_f \equiv \langle f | H | B \rangle$ and $\bar{\mathcal{A}}_f \equiv \langle f | H | \bar{B} \rangle$. In $B_d^0 - \bar{B}_d^0$ mixing system, the q/p can be treated as $e^{i\phi_d}$ as pure phase term. This relative phase accounts the transition from b to up-type quarks to strange quark s in mixing, so it can be presented as $\phi_d = \text{Arg}(V_{td}^* V_{tb}) / (V_{tb}^* V_{td}) \approx 2\phi_1$ based on negligible correction to the SM. In mode $B^0 \rightarrow J/\psi K_S^0$, considering $\Delta\Gamma$ can be treated as zero in the SM in this case[13], Equation 1.36 can be reduced to Equation 1.40.

$$A_{CP}(t) = \mathcal{S}\sin(\Delta M t) - \mathcal{A}\cos(\Delta M t) \quad (1.40)$$

For decay amplitude, which receives contributions from tree-level and loop-level processes shown in Figure 1-4 ,

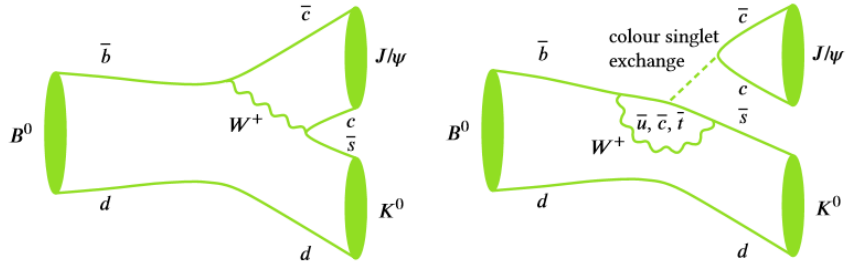


Figure 1-4: The dominated tree-level (left) and the suppressed loop-level (right) of $B \rightarrow J/\psi K^0$, in which K^0 particles are detected K_S^0 . [14]

Using the relation $|V_{ub}| \ll |V_{cb}| \ll |V_{us}| < |V_{cs}|$, it's obvious that $V_{ub}^* V_{us} \ll V_{cb}^* V_{cs}$, so the penguin-mode is suppressed in the Standard Model. Defining η_f as the CP eigenvalue,

Given $\eta_f = 1$ and $|\lambda_f| = 1$ in $B^0 \rightarrow J/\psi K_S^0$, from 1.37, CP violation parameters

can be presented as shown in Equation 1.41.

$$\mathcal{S} = \text{Im}(\lambda_f) = -\sin(\phi_d)\eta_f = -\sin(2\phi_1); \mathcal{A} = 0 \quad (1.41)$$

From Equation 1.41, ϕ_1 can be obtained precisely in the measurement of time-dependent CP violation in $B^0 \rightarrow J/\psi K_S^0$.

1.4.3 ϕ_1 from penguin-dominated mode $b \rightarrow q\bar{q}s$

Compared to $B^0 \rightarrow J/\psi K_S^0$ channel, the measurement of \mathcal{S} and \mathcal{A} from penguin-dominated channels through $b \rightarrow q\bar{q}s$ where q is u, d, s can be different due to the varied tree-to-penguin amplitude ratio. Furthermore, they are quite sensitive to NP effects for the following reasons[15]. First, they can probe $B^0 - \bar{B}^0$ through different short-distance vertices than the tree-level dominated decays. Second, the tree-level decay amplitude is suppressed and penguin-level amplitude is dominated, where the overall non-NP amplitude is relatively small so NP effects may show up easier. Last but not least, they comprise a large number of different final states, which can help disentangling non-perturbation long-distance physics from short-distance information, such as ϕ_1 or NP contributions to the weak Hamiltonian.

Considering possible New Physics contribution as A_f^{NP} , the decay amplitude can be rendered as Equation 1.42

$$\mathcal{A}_f = \lambda_u^s T_f + \lambda_c^s P_f + A_f^{NP} \quad (1.42)$$

where T_f and P_f are tree-level and penguin-level amplitudes. The coefficients λ_u^s and λ_c^s are determined from CKM matrix elements by $\lambda_i^q \equiv V_{ib}^* V_{iq}$. Note that compared to the $B^0 \rightarrow J/\psi K_S^0$, the tree level amplitude T_f is suppressed and penguin amplitude P_f is dominated in $b \rightarrow q\bar{q}s$. It is also worth noting that T_f contains tree-level W^\pm exchange, QCD and electroweak penguin contributions. These carry the combination of CKM matrix elements $\lambda_t^s = V_{ts} V_{tb}^* = -(1 + \epsilon_{uc})\lambda_c^s$ where $\epsilon_{uc} \equiv \lambda_u^s / \lambda_c^s = \mathcal{O}(\lambda^2)$. In the SM with neglected ϵ , $b \rightarrow q\bar{q}s$ modes are pure penguin with the same weak phase

as $B^0 \rightarrow J/\psi K_S^0$ has. Thus, direct CP violation vanishes and time-dependent CP violation reflects \mathcal{S} in the same way as $B^0 \rightarrow J/\psi K_S^0$ does.

Departures from this limit, non-neglected tree amplitude T_f (often called “tree pollution”), as well as possible NP effects, could give different results on ϕ_1 . Introducing the tree-penguin ratio $r_f^T = T_f/P_f$, NP-to-SM ratio $r_f^{NP} = \mathcal{A}_f^{NP}/(\lambda_c^s P_f)$, the following statements are usually used[15]:

- Branching ratios are affected at $\mathcal{O}(|\epsilon_{uc} r_f^T|, |r_f^{NP}|)$
- Direct CPV in the SM are of $\mathcal{O}(\epsilon_{uc} \text{Im}(r_f^T))$
- $-n_f^{CP} \mathcal{S} = \sin(2\phi_1) + \Delta\mathcal{S}$, where $\Delta\mathcal{S} = 2\cos 2\phi_1 \sin \phi_3 |\epsilon_{uc}| \text{Re}(r_f^t) + \Delta\mathcal{S}^{NP}$

1.4.4 ϕ_1 from $B^0 \rightarrow K_S^0 K_S^0 K_S^0$

Since Belle reported the time-dependent CP analysis on various $b \rightarrow q\bar{q}s$ which experimentally showed that the difference on ϕ_1 has a margin for NP effects[16], the improved measurements with a larger data collection is popularly discussed in order to reduce the impact of uncertainties and clear the tension between results. The decay channel $B^0 \rightarrow K_S^0 K_S^0 K_S^0$ is one of the most promising modes for this purpose. The CP eigenvalue of $B^0 \rightarrow K_S^0 K_S^0 K_S^0$ is positive ($CP = +1$). Since there's no up-quark shown in the final states, the potential contribution of $b \rightarrow u\bar{u}s$ rescattered into $b \rightarrow s\bar{s}s$ is almost of absence. This makes $B^0 \rightarrow K_S^0 K_S^0 K_S^0$ a cleaner channel than $B^0 \rightarrow K^+ K^- K_S^0$ which has a different weak phase contribution [17]. Any NP effects expected in the $B^0 \rightarrow \phi K_S^0$ should also affect $B^0 \rightarrow K_S^0 K_S^0 K_S^0$ and the absence of NP effects will lead the same CP violation just as $J/\psi K_S^0$ [17]. Currently there's no specific theoretical calculation on the $\Delta\mathcal{S}$ for three-body $B^0 \rightarrow K_S^0 K_S^0 K_S^0$. However, due to the same weak phase of this decay as $\eta' K_S^0$ and ϕK_S^0 , the theoretical prediction on $\Delta\mathcal{S}$ is usually applied to $B^0 \rightarrow K_S^0 K_S^0 K_S^0$ as well[17]. The expected range on $\Delta\mathcal{S}$ is typically at level of ~ 0.05 [18], which requires the expected precision improvement for both statistical and systematic uncertainty in future data. The result of ϕ_1 from $B^0 \rightarrow J/\psi K_S^0$ using full Belle data is presented as $\mathcal{S}_{J/\psi K_S^0} = +0.670 \pm 0.029(\text{stat}) \pm 0.013(\text{syst})$ [15]. In the meantime, the latest result of ϕ_1 from $B^0 \rightarrow K_S^0 K_S^0 K_S^0$ using full Belle data[19] is presented as: $\mathcal{S}_{3K_S^0} = -0.71 \pm 0.23(\text{stat}) \pm$

0.05(syst), and the result from BaBar [20] is: $\mathcal{S}_{3K_S^0} = -0.94^{+0.21}_{-0.24}(\text{stat}) \pm 0.06(\text{syst})$. Both results have shown a small deviation from the result in $B^0 \rightarrow J/\psi K_S^0$ for NP effects while the statistical uncertainties are dominated which prevents the claim whether NP effects are spotted. In $B^0 \rightarrow K_S^0 K_S^0 K_S^0$, the experimental sensitivity of $\Delta\mathcal{S}$ will be dominated by $\mathcal{S}_{3K_S^0}$ because the total uncertainty from $J/\psi K_S^0$ will be reduced to about 0.005 at 50 ab^{-1} Belle II data[15]. The Figure 1-5 shows the scaled $\Delta\mathcal{S}$ uncertainty regarding the luminosity in Belle II prospective[21], which only includes the statistical uncertainty of Table 1.1 . If the conservative estimation of systematic uncertainty from Belle is considered, the red arrow shows the approximate luminosity where the experimental sensitivity becomes comparable with theoretical prediction at ~ 0.05 . If the future result is different from that in $J/\psi K_S^0$ with 5 times of the uncertainty at 0.05, then it could be an evidence for NP effects. Of course, smaller the total uncertainty is, easier to identify the existence of NP effects.

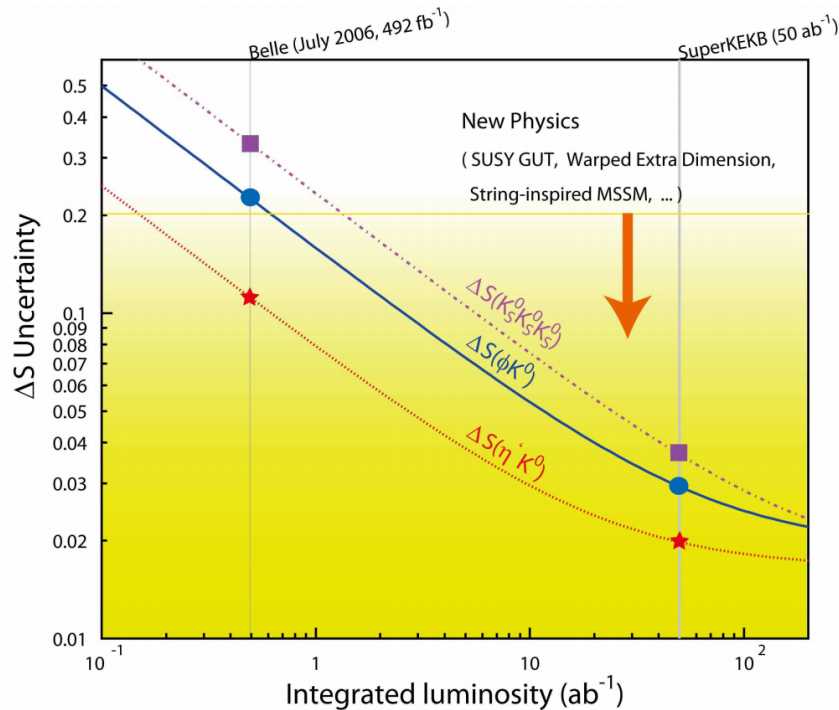


Figure 1-5: Expected sensitivity of $\Delta\mathcal{S}$ regarding the integrated luminosity of Belle II prospective.[21]

Table 1.1: $\Delta\mathcal{S}$ scaled uncertainty (statistical) with integral luminosity [21].

Observable	Belle (0.5 ab^{-1})	Belle II (5 ab^{-1})	Belle II (50 ab^{-1})
$\Delta\mathcal{S}_{\phi K_S^0}$	0.22	0.073	0.029
$\Delta\mathcal{S}_{\eta' K_S^0}$	0.11	0.038	0.020
$\Delta\mathcal{S}_{K_S^0 K_S^0 K_S^0}$	0.33	0.105	0.037

Chapter 2

Belle II experiment

2.1 Belle II and SuperKEKB overview

The fundamental goals of Belle II experiment are to search for evidence of New Physics in the luminosity frontier, and to improve the precision of the measurement of the SM parameters, such as CP parameter.[15] It uses SuperKEKB accelerator as its particle collider at the center-of-mass energy in the region of $\Upsilon(4S)$ resonances. The majority of the production will at the $\psi(4S)$ resonance that is slightly above the mass of two B mesons. The electron and positron beams are designed at 7 GeV and 4 GeV, respectively, with boost factor of 0.28. This creates an environment for measuring time-dependent CP violation by displacing the decay vertices of a B meson pair in a measurable distance along the boosted direction. SuperKEKB has a targeted luminosity of $8 \times 10^{35} \text{ cm}^{-2}\text{s}^{-1}$, 40 times higher than its predecessor, KEKB at peak luminosity. The expected operation period is from 2019 to the end of 2030. These facilities are located in KEK, Tsukuba City, around 70 km in the north of Tokyo, Japan. Some key parameters of SuperKEKB are listed in Table 2.1. The overview of SuperKEKB and Belle II are shown in Figure 2-1.

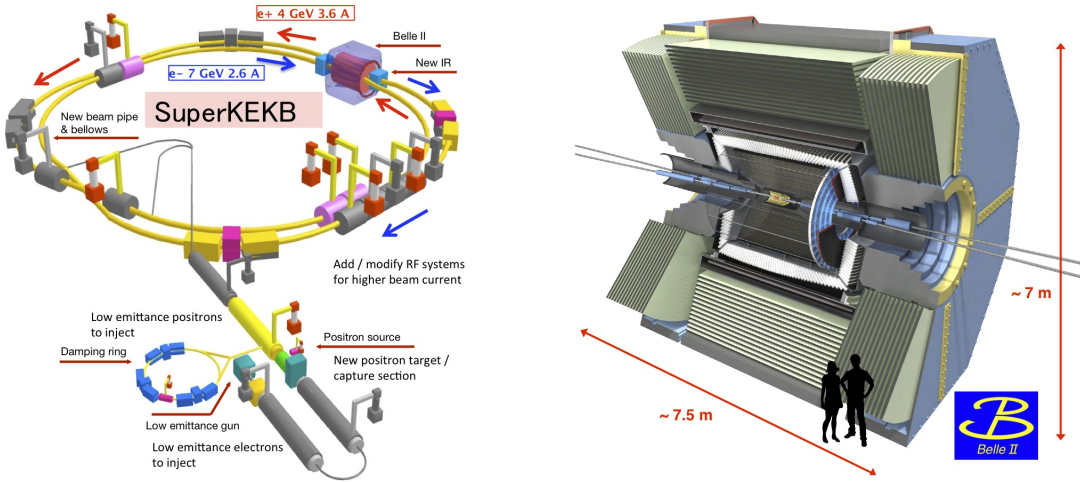


Figure 2-1: Overview of SuperKEKB and Belle II detector [21].

Table 2.1: SuperKEKB parameters for low energy (LER) and high energy (HER) rings.[15]

Parameters	LER(e^+)	HER(e^-)	Unit
Energy	4.0	7.0	GeV
Half crossing angle	41.5		mrad
Horizontal emittance	3.2	4.6	nm
Emittance ratio	0.27	0.25	%
Beta functions at IP (x / y)	32/0.27	25/0.30	mm
Beam currents	3.6	2.6	A
Beam-beam parameter	0.0881	0.0807	
Luminosity	8×10^{35}		$\text{cm}^{-2}\text{s}^{-1}$
Perimeter of ring	3		km

Belle II detector has a similar size as Belle so that it fits in the previous shell, but all sub-detectors and components have been either newly built or considerably upgraded. The advantage of SuperKEKB requires that Belle II has to be able to

stably operate at 40 times higher events rates as well as 10 to 20 times higher beam background compared to Belle at its peak luminosity. This means the mitigation of the effects caused by such high beam background is essential to the success of Belle II. Higher background level leads to high occupancy and radiation damage to the detectors at close range, along with more fake hits in the vertex detectors, pile-up noises in electromagnetic calorimeter and neutron-induced hits in muon detector. Data-acquisition system (DAQ) and trigger are also upgraded not only to adapt to higher luminosity but also for low-multiplicity event sensitivity to support a broader search especially in dark sector. Belle II detector top view is shown in Figure 2-2, and expected performances are summarized as follows:

- vertex resolution of B mesons of $\sim 50 \mu\text{m}$,
- excellent reconstruction efficiency for charged tracks down to several 100 MeV and fairly good efficiency for charged tracks down to $\sim 50 \text{ MeV}$,
- excellent momentum resolution up to $8 \text{ GeV}/c$,
- highly efficient particle identification to separate π^\pm , μ^\pm , e^\pm , K^\pm and p at full energy range of experiment,
- full cover of experimental acceptance solid angle,
- ultra fast and highly efficiency DAQ and trigger system to cope with large data quantities and fast triggering frequency.

The success of Belle II detector depends on the complex of sub-detectors which each of them is design for specific purposes. The critical components and features are explained in the following sections.

2.2 Vertex detector (VXD)

There are two components in VXD, the silicon based pixel detector (PXD) and silicon based vertex detector (SVD), where total 6 layers are placed in the inner-most region from interaction point (IP). As for PXD, two layers are placed at radii of $r = 14 \text{ mm}$ and $r = 22 \text{ mm}$ with DEPFET type pixel sensors, respectively. The PXD layers are the closest to Interaction point (IP) so the vertex resolution can be much improved.

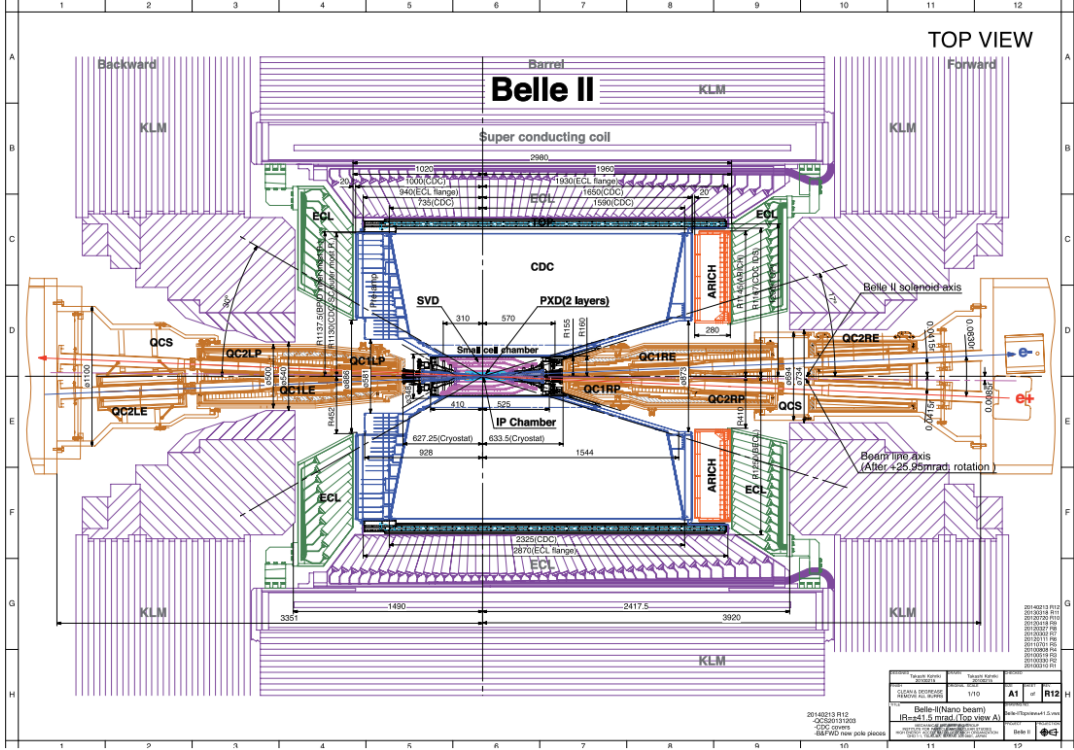


Figure 2-2: Belle II detector top view [15].

However, much higher events rate comes with much higher background level on PXD sensors. The overloaded occupancy leads to severe dead time and incredibly large data size from PXD if no data reduction scheme is implemented. In order to trim down data from PXD, a fast online tracking system is built up. In the data taking workflow, the data from PXD will be first readout to a system called “ONSEN” which can store large size temporary data up to 5 seconds. In this timing window, a fast online tracking system will perform a track fitting extrapolate the fitted tracks backward to PXD plane so the region of interest (ROI) on PXD sensors can be defined. The data outside of the ROI are not read out from ONSEN system to external tapes where offline data is written. This scheme helps reduce large fraction of data especially in the very high luminosity.

For the SVD detector, the sensors are made of “double-sided silicon strip sensors” (DSSD) with 4 layers at 39 mm, 80 mm, 104 mm, and 135 mm. The geometry of VXD from the is shown in Figure ???. The outmost layer of SVD is also larger than Belle SVD1/2. This could be helpful for ensure the reconstruction efficiency for the decay

like $K_S^0 \rightarrow \pi^+ \pi^-$. However, the current hit filter of SVD doesn't allow the "single-hit seeding" in the track reconstruction, which means any track candidate should have at least two SVD hits. This is due to the concern of the large fraction of single-hit background. For the K_S^0 with long flight length, if the daughter π^\pm only hits one layer of SVD, the reconstruction efficiency is dropped.

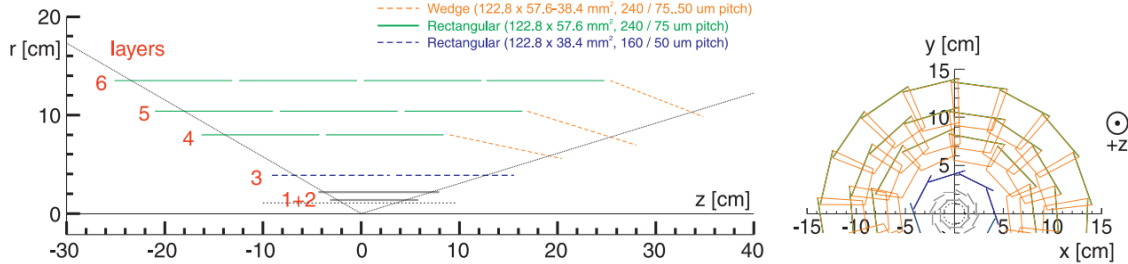


Figure 2-3: A schematic view of PXD (2 layers in gray) and SVD (4 layers in green and orange) [21].

2.3 Central drift chamber (CDC)

The central tracking system is the core component of spectrometer in Belle II, which consists of a fairly big drift chamber made of many small drift cells filled with He-C₂H₆ gas. The out radius of CDC has been extended to 1130 mm from 880 mm of Belle thanks to the much thinner layers in barrel region. The whole CDC contains 14336 sense wires in 56 layers, placed in the axial direction or the stereo direction. Such design can utilize the information from axial and stereo wires to construct a full 3 dimensional hits which forms helix tracks in CDC volume. Thus, CDC is one of the key components for measuring the helix parameters for tracking system. The example of CDC tracking of a cosmic ray event is shown in Figure 2-4

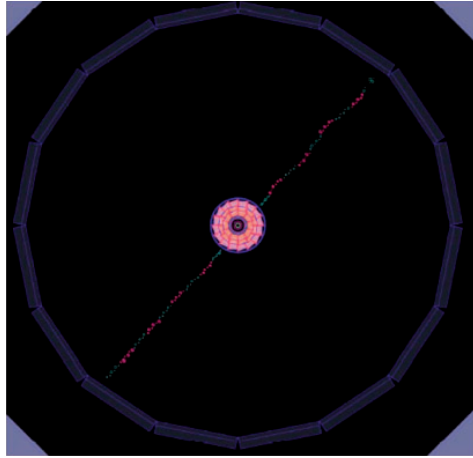


Figure 2-4: CDC tested with a cosmic ray event [15]

2.4 TOP and ARICH detectors

The particle identification system of Belle II mainly consists of two parts, time-of-propagation counter (TOP) and aerogel based Cherenkov radiation imaging ring (ARICH). TOP is the specialized detector that can reconstruct Cherenkov radiation's time of arrival and generated position by a photon detector placed at the end of a 2.6 cm quartz bar. Due to the ultra-fast flying time of photon, the TOP detectors has to achieve timing resolution at around 100 ps. A 16 channels micro-channel plate photon-multiplier (MCP-PMT) with custom-made waveform electronics of readout is used. The resolution of starting time is achieved about 50 ps. [21].

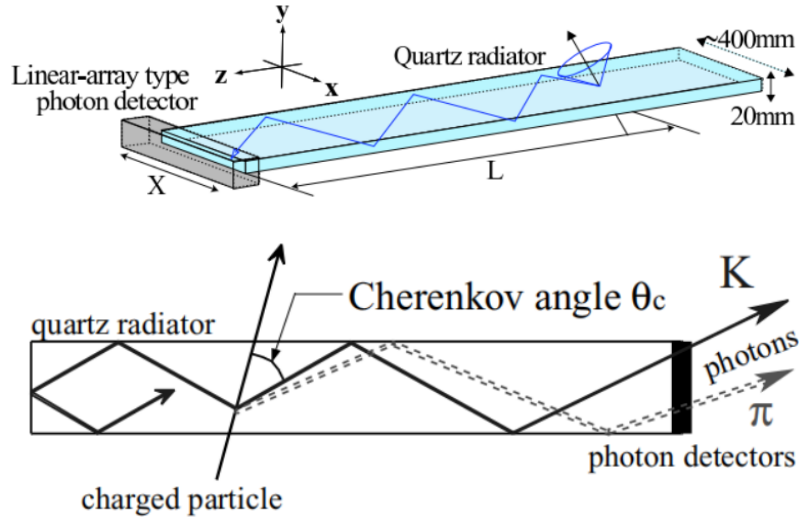


Figure 2-5: Schematic view of TOP counter (up) and its imaging process of K^\pm and π^\pm (down)[21].

As for ARICH, it uses areogal as the sensitive material to approximately image the Cherenkov ring by a special focusing structure to identify charged particles. ARICH should be able to separate charged particles in a momentum range from 0.5 GeV to 4 GeV. ARICH requires single-photon-sensitive high-granularity sensor to reconstruct the Cherenkov angle with small photon yield. Hamamatsu Corporation, Japan, has developed a hybrid avalanche photon detector (HAPD) to meet the requirements. Each sensor is $73 \times 73 \text{ mm}^2$ embedded with 144 channels to accelerate emitted electrons in a 8 kV field. Avalanche photo-diodes (APD) are used for the detection of electrons at the end of electron acceleration, see Figure 2-6. The ARICH detector outlook and the ring image of cosmic μ on the HAPD sensors are shown in Figure 2-7.

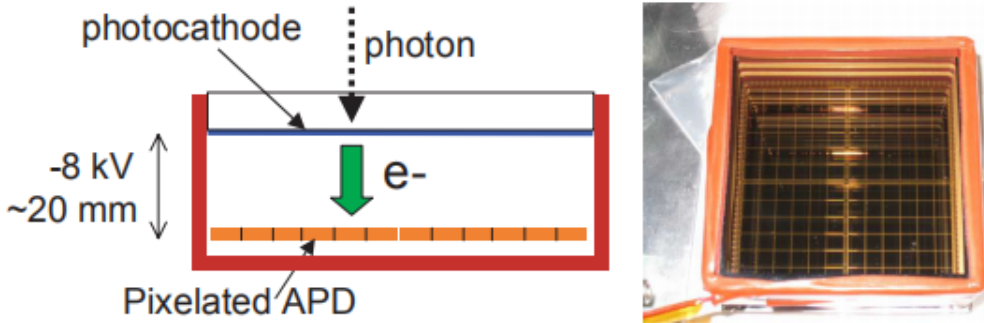


Figure 2-6: Photon-electrons acceleration (left) and pixelated APD (right) at the end[21].

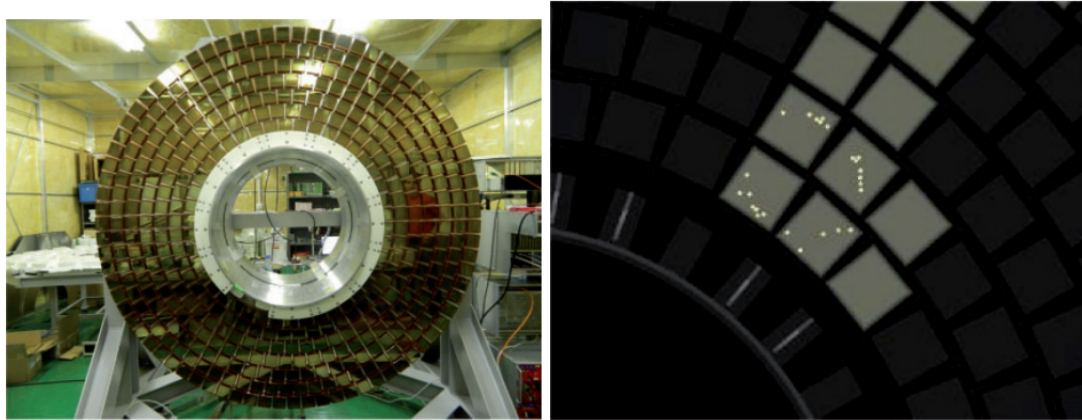


Figure 2-7: ARICH detector (left) and the ring image of cosmic μ on the HAPD sensors[15]

2.5 Electromagnetic calorimeter (ECL)

The electromagnetic calorimeter of Belle II is mainly responsible for the detection of γ radiation and electrons. The thallium doped caesium iodide CsI(Tl) crystals are assembled tightly in all three different regions, backward/forward end-caps and barrel region. Compared to the previous ECL in Belle, the pre-amplifiers and the structures remain unchanged, while the readout electronics have been upgraded. The estimated background level in Belle II ECL will cause the much longer decay time in the scintillation of CsI(Tl). This will lead to the pile-up effect of readout noise. To compensate this effect, wave-form sampling electronics are embedded with the photon

detectors (PMT). Especially in the forward direction of the electron beamline, where the level of beam background is much higher, the effect of pile-up noise becomes even worse and the performance of ECL will be of trouble if no special measure taken. In this situation, the pure CsI crystal is chosen as the material of detector to achieve a fast wave-shaping time and higher radiation tolerance compared to the dosed CsI(Tl).

2.6 K_L^0 muon detector (KLM)

KLM system of Belle II consists of a sandwich stacked iron plates and detectors at outside of the superconducting solenoid. The iron plates serve as the interaction materials with > 3.9 times the interacting length of material compared to the ECL, allowing K_L^0 particles to shower through. The Belle KLM material uses the glass-electrode resistivity plate chambers (RPC) which is not suitable for Belle II due to high background level. Neutrons dose is significantly larger due to the much more electromagnetic radiation reaction on detector materials. The long dead time of RPC under such dose rate will reduce the efficiency of KLM. Besides, the mis-identification possibility would be raised so PID contribution from this part of detector will be meaningless. To mitigate this problem, the RPCs are replaced by the layers of scintillator strips with wavelength-shifting fibers, read out by silicon photomultipliers (called “SiPMs”, Geiger mode operated APDs) as light sensors, which is proven to be able to reliably operate by setting up the discrimination threshold [15].

2.7 Trigger and DAQ system

The interesting topics in Belle II physics analysis highly depend on the trigger system. With the upgraded capabilities to study a wide range of physics analysis at a very high luminosity in Belle II, the trigger system is expected to properly operate at a high event rate. The Belle II trigger system is composed of two levels: a hardware-based, low-level trigger called “L1” trigger, and a software-based high-level trigger (HLT). The L1 trigger has a latency of $\sim 5\mu\text{s}$ and the maximum trigger output rate

is 30 kHz, which is limited by the read-in rate of data acquisition system (DAQ). Considered the high event rate and background level from future Belle II luminosity, a series of upgrades have been implemented for L1 trigger. The key improvements of L1 come from the firmware-based reconstruction algorithm and trigger logic. It's worth noting that a specialized set of hardware trigger lines for dark sector researches are implemented, which improves the trigger efficiency for single energetic photon in the final states.

HLT, as the second level of Belle II trigger systema, plays an important role in DAQ. As discussed in the section of PXD, the data size in PXD is huge at high luminosity and the ROI selection must be applied to reduce the online event rate. The event rate reduction relies on the tracking extrapolation on PXD plane, which is the key function of HLT. HLT can suppress the event rate down to 15 kHz using the information from the CDC tracking and ECL reconstruction. The event rate is further reduced to 10kHz by using full reconstruction information.

Since the primary goal of Belle II is focusing on B physics studies, it is natural that the trigger system should be able to operate over all of the interesting B physics conditions, with normally 3 or more CDC tracks and large energy deposition in ECL. By offline reconstructing the simulated events and studying the efficiency, close to 100% B decays are recorded by Belle II trigger system. However, the extensive capabilities of studying a large range of physics not only in b sector brings a challenge to Belle II trigger and DAQ system. Belle II is expected to show the excellence at performing measurements on other important topics such as τ physics and dark sector researches. These topics usually suffer from the high beam background. Thus, the control of beam background becomes essential. With SuperKEKB, beam background is about 10 to 20 times higher than Belle at the peak instantaneous luminosity. This rises a challenge for Belle II trigger and DAQ system. The main sources of beam background are beam-gas scattering, synchrotron radiation, the radioactive Bhabha scattering, the two-photon process, beam-beam effects, and Touschek effect. Their impacts depend on many factors such as beam current, luminosity and vacuum conditions, etc. One of the featured topology of these beam background events is the

combination of two charged tracks in CDC and one or two clusters in ECL. Beam background events are often assembled with low-multiplicity events from primary collision, and the latter is the main focus of dark sector studies. It's quite important to distinguish these low-multiplicity events from various beam backgrounds. The simulated beam background rate and their sources are listed in Table 2.2.

Table 2.2: Simulated beam background rate (12th BG campaign)[15]

Type	Source	Rate (MHz)
Radiative Bhabha	HER	1320
Radiative Bhabha	LER	1294
Radiative Bhabha(wide angle)	HER	40
Radiative Bhabha (wide angle)	LER	85
Touschek scattering	HER	31
Touschek scattering	LER	83
Beam–gas interactions	HER	1
Beam–gas interactions	LER	156
Two-photon QED	-	206

The improvements on both L1 and HLT triggers, along with DAQ upgrade has shown a good potential in dark sector researches[22][23], thanks to the improved discriminating ability of low-multiplicity events against beam background. In future, several modifications on the current trigger system is under consideration, such as the partially pre-scaled trigger lines, which is expected to be optimized for dark sector studies[15].

2.8 Analysis Software

The data acquired by the Belle II experiment or simulation can be processed by Belle II Analysis Software Framework, called BASF2. It has a good capability to handle the tasks of sophisticated algorithms for simulation, reconstruction, visualization, and analysis. The official BASF2 is developed in different release versions, light-versions and featured-versions. In this thesis, release-05-01-01 version is used.

2.8.1 BASF2 Core Structure

The core structure of BASF2 contains three major parts: the analysis codes specifically required by the needs of Belle II data (called Belle II codes), the external libraries that are the third-party software which Belle II utilize, and the tools for configuring and installing the BASF2 software.

The Belle II codes consists of many packages. They are categorized based on the different levels of Belle II detector components, like the packages of base-level system control called “framework”, the package for track reconstruction called “tracking”, and the one for post-reconstruction data analysis called “analysis”. Users can work either with compiled binary version of BASF2 installed centrally on working servers, or build from the source based on their own need.

As for the externals, it contains the many packages or libraries that provide functionalities BASF2 needs during the execution or installation. For example, some basic packages, like gcc compiler, cmake, tar, wget, Python and git are included. In particular, due to the dependence of the analysis tools that may be frequently used by Python, around 100 additional Python packages are installed as the externals, such as “Numpy” and “matplotlib” packages that provide functions for statistical calculations and plotting. The complexity of building all of these external software could be tough for users so that the compiled versions that cover the common platforms are available from BASF2 official repository.

Tools are collections of shell or Python scripts for setting up BASF2 and externals environment. It can easily handle the need of setting up an environment of specific BASF2 version and the externals tied to that version. It also provides a function to setting up the environment of developing BASF2, where developers can get one developing copy of BASF2 and write the additional codes as the modification, so the compatibility of BASF2 could be easily maintained by building a release version from the developing branches. In this thesis, two new packages are developed and built with release-05-01-01 version BASF2. This developing version of BASF2 contains all functions that release-05-01-01 has. The details will be discussed later.

2.8.2 Event Processing Workflow

The data from Belle II detector or from the simulation, are organized into a set of runs that are defined by either experimental conditions or simulation conditions. For instance, the simulation data from a certain detectors' condition are packed together, marked with the conditions' database index that is used during the simulation. Such data sample then is divided into different runs based on estimated luminosity from experiment, which can contain the different number of events in each run. This scheme is used for categorizing experimental data as well, so that users can easily know which experiment conditions are used. In a run, every event is recorded as an independent measurement of an electron-positron collision, a cosmic ray injection or background event. Such experiment-run-event structure is the basic data structure that BASF2 handles. Thus, when BASF2 processes a data set, the functions are called for every event based on different configurations that are corresponding to the different experiment conditions. For example, in a data set where events are recorded with the different magnetic fields, BASF2 can automatically change the configurations of the magnetic fields event-by-event to provide a better track measurement. Based on this idea, all BASF2 functions (called “modules”) are developed based on a python module class which contains following embedded functions to be called at event-based level:

- initialize: called at the start of processing a event to properly set up constants needed for this run.
- beginRun: called at the start of calling this module, including setting up database conditions used in this run (run-dependent configurations) or event (event-based configurations).
- event: called for each event. This is the actual processing step, such as perform tracking or combining all daughters to find a mother particle.
- endRun: called at the end of a run, usually to register all processed information to the storage, such as physics variables from all reconstructed particles.
- terminate: called at the end of the processing of all events, release the buffered

space and memory.

BASF2 executes a series of modules loaded dynamically to process the data set according to above sequence. The selection, configuration and executed order of the modules are defined by a file called “steering file” written in Python. The modules parameters are attributes which can be set during the runtime using the steering file. For example, the “Path” object declared in a steering file stores the sequence of modules that will be executed, to which allow other modules such as “mdstInput” or “reconstructDecay” to be added. Users can use “boolean” type variable set in “event” function to create a conditional branch of a “Path” in case that one event needs to be processed with different modules at the same time. For instance, in the decay reconstruction package, if a decay chain is not fulfilled by missing one particle in the “event” functions, other back-up decay chains can be checked to see if a successful reconstruction is possible.

The object that interacts with BASF2 I/O is called “Datastore”. This implementation doesn’t depend on the event data model. The only mandatory component is called “EventMetaData” which presents the experiment, run and event number of a event. “Unpacker” module converts the raw digits into digits-based object in BASF2. In simulation, digitization is done by module called “digitizer”. The digits-based objects are further processed to form hits or clusters depending on detector types. Higher level functions such as tracking and decay reconstructions are implemented based on these basic information by their packages. Eventually, BASF2 writes out the information based on users’ needs, like kinematics variables, to ROOT[24] format files, or simply prints out processing statistics to the standard output.

In practice, BASF2 starts running when it checks there is at least one module specifying the number of events to be processed in a “path” from the “steering file”, then it reads in the information from Datastore in the input ROOT file, execute all the requested modules in the “steering file” and return the time and number of events as information printed in standard output. In Figure 2-8, an example of “steering file” is shown, with a “path” called “main” created and a module called “EventInfoSetter” added. This steering file will process 100 event, set their experimental numbers, run

numbers and event numbers.

```
#!/usr/bin/env python3
# -*- coding: utf-8 -*-

# Generate 100 events with event numbers 0 to 99
# that contain only the event meta data.

import basf2
main = basf2.create_path()
main.add_module('EventInfoSetter', evtNumList=[100])
basf2.process(main)
```

Figure 2-8: An minimal example of BASF2 steering file, setting up a basic processing of 100 events in “path” called “main”[21].

2.8.3 mDST structure

The output from BASF2 processing can contain several detector-specific objects, which are restored as mini data summary table (mDST) type ROOT file. For instance, in a mDST file, the object called “RecoTracks” will be created if track pattern recognition is called and “Track” object will be created if the track fit is performed. For a mDST level analysis, the goal is usually aimed to find particles from physics processes and reconstruct decay information. A output mDST ROOT file could typically contain the following objects:

- Track: object presenting any charged particle trajectory. It’s linked to multiple track fit results using different nominal mass hypotheses as well as their track fit quality to help select good tracks.
- TrackFitResult: the fitting result of tracks with different mass hypotheses. It consists of five helix parameters, their covariance matrix and p-value from the fit. It also stores the information of hit pattern on vertex detector and CDC.
- V0: object for the relative long-lived neutral particles that fly out of interaction region but mostly decay or interact inside detector region. In Belle II, these are mostly K_S^0 , Λ and photon converted to electron pairs. V0 also stores their relation to

the charged daughter tracks and track fit results for further selections.

- PIDLikelihood: it presents for the possibility of a charged track to be an electron, muon, charged kaon and pion, proton and deuteron provided by particle identification system.
- ECLCluster: reconstructed cluster in ECL detector. It consists of energy deposition and hit positions as well as other hit shape related variables. If a cluster is matched with an extrapolated track, a relation between them will also be created.
- Reconstructed cluster KLM detector. It consists of momentum and position measurement. If a cluster is matched with an extrapolated track, a relation between them will also be created.
- KLId: K_L^0 candidates with the particle identification as related to KLM and ECL clusters.
- TRGSummary: L1 trigger information.
- SoftwareTriggerResult: HLT information mapped by trigger names to trigger results.
- MCParticle: simulated particles containing momentum, production and decay vertex, relations to mother and daughter particles, and traversed detector components. Particle-detectors relations are created if simulated particles are correctly reconstructed as tracks or clusters.

The size of mDST level data is very important to BASF2 offline processing performance. Thus, mDST level data is restricted from contain non-physical analysis related information such as raw digits or calibration constants. For detailed detector or reconstruction algorithm performance studies, and also for calibration tasks, a dedicated format higher than mDST, called cDST (calibration data summary table), is used.

2.8.4 Conditional Database

In addition to the physics data, analysis relies on various conditional data that are different calibration of detector, weight files for multi-variate analysis usage like PID and so on. This data is stored in a central database server called central Conditional

Database (CDB).

Conditions are made of payloads and each payload has its own “Intervals of Validity” (IoV). It defines in which runs the payload is valid. A set of payloads and IoVs are called a global tag (GT). Considered the GT that is required by the different analysis purposes may change even though the experiment condition is still same, GT is subjected to be updated once new calibrations of detectors or weight files for MVA tools are available. On the users’ side, except for just using central database, a local database back-end that takes GT information such as calibration data while uses a local database, such as a customized PID weight file, is also possible. It automatically download the needed database files that are required for a BASF2 execution and stores them in a local folder. This means even if the local machine is offline or the CDB is not accessible, one can still run BASF2 as long as the local folder is there.

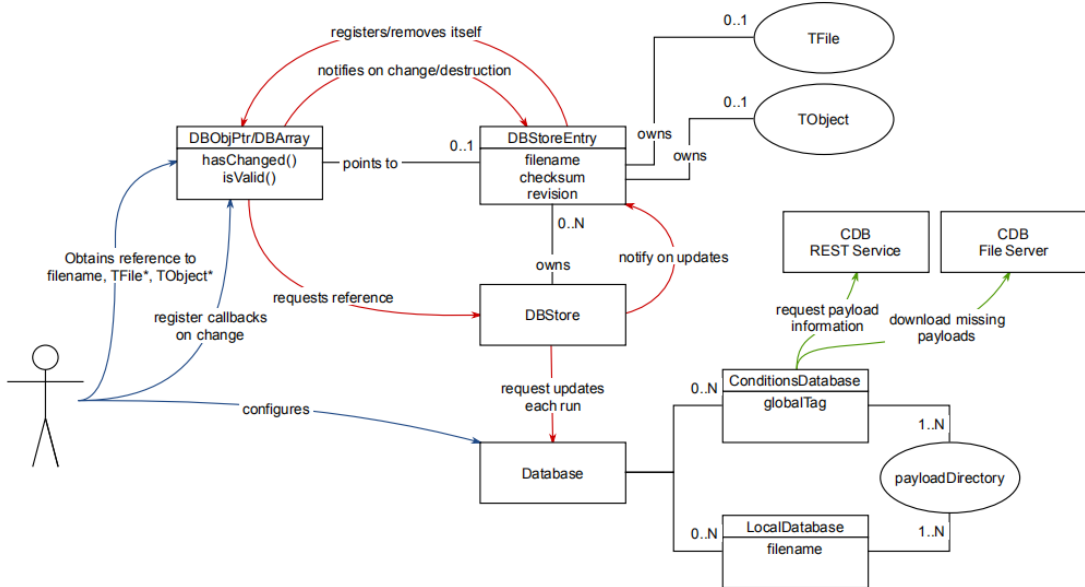


Figure 2-9: Relations of all entities in CDB[25], showing the management logic from users’ end to each CDB files and services.

The management of CBD with the extension of local database gives a good convenience for users to perform their own analysis and share the results with collaborators. Users’ access to conditions objects in the CDB is provided by two interface classes, one

for single objects called “DBObjPtr” and one for arrays of objects called “DBArray”. To facilitate easy creation of new conditions data – for example, during calibration – we provide two payload creation classes, “DBImportObj” and “DBImportArray”. They have an interface very similar to DBObjPtr and DBArray[25]. Users instantiate one of the creation classes, add objects to them and commit them to the configured database with a user-supplied IoV. This includes the support for run dependency as well. The capability to use a local file-based database allows for easy preparation and validation of new payloads before they are uploaded to the CDB. The scheme of this entities and how users interact with CDB object is demonstrated in Figure 2-9. For example, user can perform their analysis and first locally generate weight files or calibration data based on different run conditions and reconstruction criteria, which are stated by their names of the IoVs. Once the results are good to share, they can create a GT in CDB of which they have the full ownership, add all database files into the GT and open it to Belle II collaboration. Anyone who would like to re-calibrate data or use their weight files for PID and so on, can simply use the built-in function “`basf2.useCentralDB()`” in the BASF2 steering file to directly access the corresponding data. However, only the creator of the CDB objects has the right to add, recall, replace and remove the GT, which guarantees the stability of the CDB and responsibilities for each user.

2.9 Belle II simulation

This section briefly describes simulation (MC) used in the studies presented in this thesis. As for the focus of this analysis is in b sector which is mainly from $\Upsilon(4S)$ decay, the discussed simulation is based on the collisions with center-of-mass (CMS) energy at $\sqrt{s} = 10.58$ GeV.

In the previous section, it’s shown that many packages and functionalities have been integrated with BASF2, including the core components of Belle II simulation in B decay: “`evtgen`” as event generator[26] and “`GEANT4`” as the simulator of detectors[27]. Along with the active development of BASF2 in the early stage of Belle

II, the versions of software that is used for simulation and reconstruction are often different. For the simulation used in this analysis, BASF2 version release-04-02-08 was used. For the event reconstruction, the used BASF2 version is release-05-01-01. This is not a problem thanks to the CDB management, allowing modified software to use the same constants such as magnetic field distribution for the consistence between simulation and reconstruction.

All simulations start with at least one event generator that configures the physics processes. In Belle II, the configuration of “evtgen” requires a decay file called “xxx.dec” that describes the decay chain from a certain mother particle, branching fraction for all processes and decay-related information such as flavor mixing or CP violation information. For different type of decays, the different decay files are prepared. MC sample is centrally produced using Belle II GRID computing service based on these files periodically, so that the latest improvements of software can be applied. Each round of MC sample is called a campaign named with their index, such as “MC13”, which is the 13th (latest in 2020 Winter) Belle II official MC production (in the following content of this thesis, all MC samples are produced in the 13th MC campaign if not specifically stated).

For the analysis in this thesis, there are two MC samples, one is called “signal MC” and the other is called “generic MC”. Both MC samples use “evtgen” as event generator. Signal MC, as its name suggests, is the MC sample that describes the whole decay chain of $B^0 \rightarrow K_S^0 K_S^0 K_S^0$. The mother particle of the decay chain is $\Upsilon(4S)$, then it decays into a pair of $B^0 - \bar{B}^0$ at branching fraction of 100%, with the model “EvtVSSMix”[26] describing the decay model. Then, one of the B meson is set to decay into three K_S^0 based on phase-space model (“PHSP”) at 100% branching fraction. To be noted, the phase-space model doesn’t provide any time-dependent CP violation. The default configuration of “evtgen” can not handle multi-bodies charmless B decay with TDCPV. A modified decay model profile is under-development and not fully validated yet. Thus, MC sample of $B^0 \rightarrow K_S^0 K_S^0 K_S^0$ yields zero CP parameters by default. As for the other B meson, it decays into all possible final states that are described by Belle II generic decay file.

Table 2.3: Production cross section for different hadronic flavors from collision at $\sqrt{s} = 10.58$ GeV used in Belle II generic MC.[15]

Processes	$\Upsilon(4S)$	$u\bar{u}(\gamma)$	$d\bar{d}(\gamma)$	$s\bar{s}(\gamma)$	$c\bar{c}(\gamma)$
Cross section [nb]	1.110 ± 0.008	1.61	0.40	0.38	1.30

As for generic MC, all hadronic processes in a $\sqrt{s} = 10.58$ GeV collision are simulated. The total production cross section receives contributions from not only $\Upsilon(4S)$ (b -flavor decay dominated), but also u, d, s, c . Their relative branching fractions are taken from cross sections at $\sqrt{s} = 10.58$ GeV as shown in Table 2.3. Generic MC sample contains 6 types of MC samples due to this production arrangement, where $\Upsilon(4S)$ produces “mixed” (neutral) and “charged” B meson pairs and the rest are “uubar”, “ddbar”, “ccbar” and “ssbar”, respectively. In this thesis, the latter 4 types of MC samples are combined and called “qqbar” for simplicity. In the mixed MC sample, the branching fraction of $B^0 \rightarrow K_S^0 K_S^0 K_S^0$ is set at 6×10^{-6} and the branching fraction of $K_S^0 \rightarrow \pi^+ \pi^-$ is set at 0.692. Both values are taken from PDG[28]. Same as signal MC, CP violation is set to zero for signal events in generic MC since they use the same model at generator level.

In addition to the simulation of physics processes, MC campaigns are produced with at least two beam background conditions, called “BG0” and “BG1”. The former stands for no beam background and the latter is produced with one overlay of beam background. The components of them have been discussed briefly in section 2.7. The mixing of simulated beam background to simulated physics events is done by adding simulated hits on each sub-detector output. Possible pile-up of hits is therefore inherently included. The average number of background events of a given type to be added to a single simulated event is determined from the rate R of a particular background sample and the time window Δt in which the background is mixed in Equation 2.1:

$$\bar{N} = sR\Delta t \quad (2.1)$$

where s is an optional scaling factor. The injected background events are based

on a Poisson distribution with mean \bar{N} . Within the timing window, the background events are shifted randomly to simulate contributions from different bunches. To use real experiment background events (data-based beam background), the random triggered events are measured and added to simulated BG0 MC sample for a more precised background configuration. This method can give a more realistic description of actual beam background but with a possibility to introduce bias due to the pile-up effect of multiple background events in a short timing window. In the early stage of Belle II, the level of background is not high and the background pile-up effect is small. Therefore, for MC13, BG1 sample is produced with data-based beam background.

In total, there are 2 million events generated in signal MC. Half of the signal MC (1 million) is produced without beam background for cross-checking the reconstruction performance. For generic MC, 1 ab^{-1} sample including mixed, charged and $q\bar{q}$ events are produced with beam background at $\sqrt{s} = 10.58 \text{ GeV}$.

2.10 Belle II data taking

Belle II Phase I operation started in 2016 which was focused on the commissioning and test of SuperKEKB. Later in 2018, the commissioning of Belle II detector and SuperKEKB was finished. From 2019 April, Phase III operation that marked the beginning of official physics runs has started. By the end of 2020, Belle II has been operating in Phase III for 4 total run seasons. The integrated luminosity collected during this period of time is about 84.73 fb^{-1} , see Figure 2-10. The official processing of recorded data is performed along with the data taking. For the analysis reported in this thesis, the experimental data collection from experiment number 7, 8, 10 and 12 is used. Only the data collected at $\Upsilon(4S)$ energy is included. Correspondingly, the integrated luminosity that is used for this thesis is about 62.8 fb^{-1} [29].

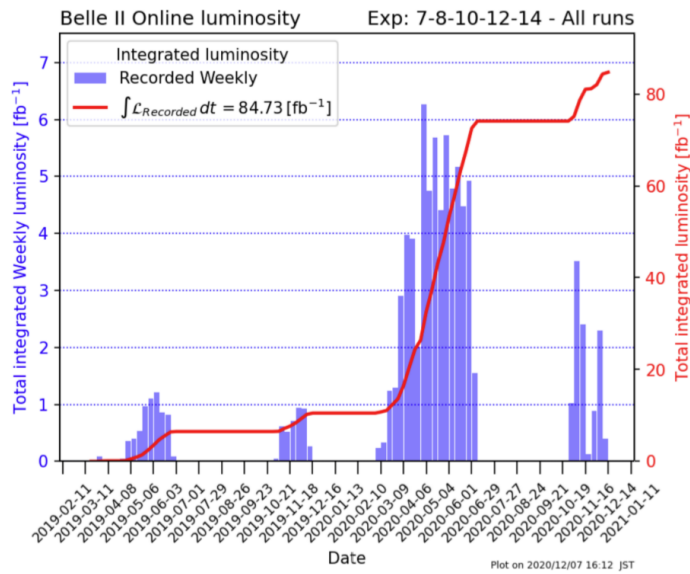


Figure 2-10: Belle II online luminosity from 2019 April to the end of 2020[29].

Chapter 3

K_S^0 reconstruction study

The final states of $B^0 \rightarrow K_S^0 K_S^0 K_S^0$ only depends on the decay of K_S^0 . The main decay channels of K_S^0 is to either $\pi^+ \pi^-$ at branching fraction of about 0.692, or to $\pi^0 \pi^0$ at branching fraction of 0.307, which are referenced from PDG[28]. The characteristics of these two decays are much different in terms of the response from Belle II detector. The charged decay that yields $\pi^+ \pi^-$ leaves two tracks originating from VXD or CDC volumes with opposite charges. On the other hand, the π^0 main decay channel is $\pi^0 \rightarrow \gamma\gamma$. This creates a bunch of clusters on ECL. The reconstruction of the decay channel is performed through $\pi^+ \pi^-$. There are mainly two reasons for not selecting π^0 as final states. First, $\pi^0 \rightarrow \gamma\gamma$ can yield a large fraction of fake K_S^0 . The reconstruction of two ECL clusters provides no constrain on K_S^0 vertex so it's almost impossible to suppress the combinatorial background using vertexing quality in this case. The only reliable selection will be the mass of K_S^0 which is typically distributed around its nominal mass with a few hundred of keV. The γ however, could be originating from many other resources, such as beam background and charged track radiation. Using mass window of K_S^0 could not effectively reject the noticeable fraction of fake K_S^0 . Second, with K_S^0 reconstructed from neutral pions , the events of B^0 that consist of one or more such K_S^0 have poorly reconstructed vertices. To be noted that even with $B^0 \rightarrow K_S^0 K_S^0 K_S^0$ which only uses K_S^0 from charged pions as the final states, there is no direct charged tracks from the interaction region, which leads to the worse resolution of vertex position compared to the channel like $B^0 \rightarrow J/\psi K_S^0$, which has two direct

charged tracks of e^+e^- or $\mu^+\mu^-$ thanks to the very short flight distance of J/ψ . If one (or more) of K_S^0 has the poor vertexing quality from its decay products, it can further reduce the precision of vertex positions of B^0 . This leads to a large uncertainties in defining the decay time of signal B^0 and the decay time difference. The latter is the key observable in TDCPV measurement. Based on above, only K_S^0 reconstructed using charged pions are considered in this analysis.

3.1 Cut-based K_S^0 Reconstruction

The K_S^0 has average life time at $(8.954 \pm 0.004) \times 10^{-11}$ s. Therefore, the flight length of K_S^0 is comparable with the scale of detector size. In the typical Belle II energy scale, the flight length of K_S^0 is in a range from a few micrometer away from B vertex, to more than 14 cm that is outside of the last layer of SVD ladder, see Figure 3-1.

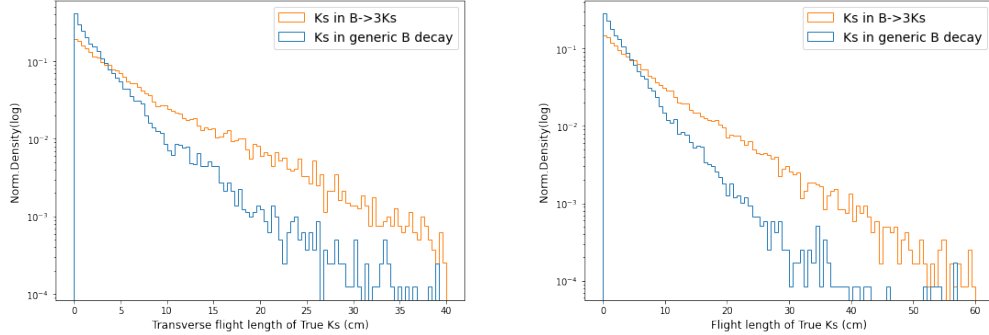


Figure 3-1: The left is transverse flight length distribution and the right is the total flight length distribution from true K_S^0 . The blue is from generic MC and the orange is from signal MC. It's clear that the average K_S^0 flight length in signal MC is longer. Both plots are normalized.

Due to the different topology of B^0 decay, the average momentum of K_S^0 in generic MC is different from the ones from signal MC. While it's clear that the fraction of K_S^0 decaying outside the IP is the majority in both MC samples and therefore there's no reason to constrain K_S^0 decay vertices in IP. In general, the cut-based reconstruction for K_S^0 is first performed by the selection of invariant mass from its decay products. After the selection on invariant mass is applied, a vertex fit for each K_S^0 using charged pions' tracks is done without IP constraint. This reconstruction is mainly

achieved by using standard BASF2 particle list called “stdKshort:merged”. In this “stdKshort:merged” list, two K_S^0 particle collections are first reconstructed and then merged. We first take all the “V0” objects from BASF2 Datastore which use 2 online

Table 3.1: Pre-selection criteria of $\pi^+\pi^-$ for K_S^0 offline reconstruction.

Selection Criteria	θ CDC acceptance	CDC Hits Number > 20	PID pionID > 0.1
-----------------------	----------------------------	---------------------------	-----------------------

reconstructed charged tracks with opposite charges and a converged fitted vertex. The invariant mass “M” from two pions’ 4-vector is calculated. The K_S^0 candidates with “M” between $0.45 < M < 0.55$ GeV are selected, named “Ks:V0”. In addition to these K_S^0 from “V0” objects, another K_S^0 collection from offline reconstruction is also formed. In this step, charged tracks with mass hypothesis of π^\pm is used, which the tracks and PID of charged pions are pre-selected by the criteria in Table 3.1. Then K_S^0 are found by combining all of these tracks and the candidates with “M” in between $0.3 \sim 0.7$ GeV before the vertex fit are kept. Then, vertex fit is perform for these candidates and the ones that have converged vertices and $0.45 < M < 0.55$ GeV are considered as the K_S^0 candidates, named “Ks:reco”, which uses the same criteria as “V0”-based reconstruction. In both cases, the vertex fit is performed using “TreeFit”[30] that is the recommended algorithm in Belle II. It’s clear that there are duplication of K_S^0 if two collections are merged directly. Therefore, the objects’ index of two daughters’ tracks in the Datastore are compared between K_S^0 from these two collections, from which the identical combinations are removed to avoid duplication. The B^0 reconstruction efficiency is highly sensitive to the efficiency of charged pions because the final states particles are three identical K_S^0 decaying to 6 charged pions. That’s why only a very loose selection on π^\pm is applied. The selected K_S^0 collection using cut-based method therefore contains many fake candidates, see the distribution of “M” from cut-based selected K_S^0 from signal MC in Figure 3-2.

The reconstruction quality of K_S^0 also depends on the flight distance. K_S^0 that decay in the inner region of VXD yields more hits on the SVD layers from its charged daughters, which is critical in performing a proper tracking. Belle II tracking efficiency

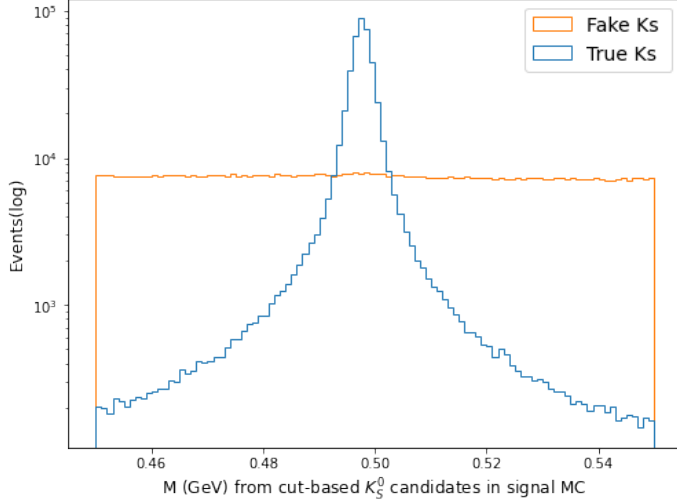


Figure 3-2: “M” of K_S^0 from cut-based selection in signal MC. The blue line is the true K_S^0 and the orange is the fake K_S^0 . 200000 candidates are used in total.

gets poor due to higher beam background when performing track finding for tracks without inner detector hits such as SVD. For certain fraction of K_S^0 decaying outside of layer 5 of SVD, it’s much likely that there is no SVD hits assigned to their daughters’ tracks. This is due to the feature of SVD track finding, where a track candidate needs either at least 3 SVD hits to form a good track, or 2 hits to form a hit double-lets, to be used for combining tracks with other track candidates. Single hit on layer 5 or layer 6 is filtered out to suppress the large fraction of beam background induced by random single hits. This effect is shown in Figure 3-3. K_S^0 are categorized based on how many SVD hits their daughters have, in which *SVD10* and *SVD01* stands for K_S^0 that only π^+ and π^- has non-zero SVD hits number, *SVD11* and *SVD00* stands for K_S^0 that both or neither charged pions have SVD hit non-zero SVD hits number. This is related to the track quality of K_S^0 where *SVD11* K_S^0 has the best quality and *SVD00* has the worst. Thus, the efficiency and purity of K_S^0 with long flight length is reduced. It’s clear that *SVD00* K_S^0 show up at about 11 cm where SVD layer 5 is placed. Most of *SVD10*(*SVD01*) K_S^0 start to show up at the similar range. The geometric structure of PXD and SVD is shown in Figure 2-3 and the fraction for each types of K_S^0 in $B^0 \rightarrow K_S^0 K_S^0 K_S^0$ is listed in Table 3.2.

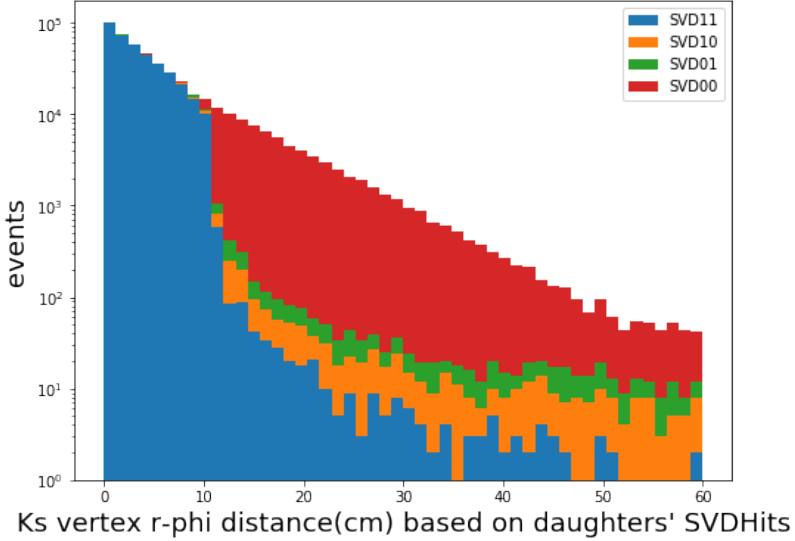


Figure 3-3: K_S^0 transverse flight length based on SVD hits of pions. $SVD11$: both pions have SVD hits, $SVD10(SVD01)$, positive(negative) pions have SVD hits, and $SVD00$: no SVD hits from pions. The result is from signal MC of $B^0 \rightarrow K_S^0 K_S^0 K_S^0$.

K_S^0 type	SVD11	SVD00	SVD10	SVD01
% in Belle II	52%	39%	5%	5%

Table 3.2: The fraction of each category of K_S^0 based on pions SVD hits in $B^0 \rightarrow K_S^0 K_S^0 K_S^0$ signal MC.

Fake K_S^0 candidates costs a large extra processing time and the number of combinatorial backgrounds in $B^0 \rightarrow K_S^0 K_S^0 K_S^0$ becomes high. It largely reduces the signal significance and introduce bias to the result of CP parameters. Thus, a multi-variate analysis (MVA) based K_S^0 identification package, called “KsFinder”, is developed to further reject the fake K_S^0 from cut-based selected candidates.

3.2 MVA-based K_S^0 Identification: KsFinder

3.2.1 Belle II K_S^0 classification

As mentioned in the last section, in order to improve the reconstruction performance of K_S^0 from cut-based selection, a MVA-based package called “KsFinder” has been developed. The reconstruction of K_S^0 can be treated as a typical classification problem.

The input is a set of variables that describes the characteristics of $K_S^0 \rightarrow \pi^+ \pi^-$ decay. The training target is the true or fake flag from the MC truth-matching variable called “isSignal” where $\text{isSignal} = 1$ (0) stands for being a true (fake) K_S^0 . It aims to improve the limitations in the Belle K_S^0 MVA classification tool.

In Belle, the K_S^0 reconstruction was first done by using cut-based method to select primary candidates, then a MVA-based classifier was implemented by assigning two likelihood indicators to each K_S^0 candidates. The package used by Belle is called “nisKsFinder”[15] conventionally. It outputs the two likelihood variables based on “NeuroBayes” algorithm[31], which defines the goodness of K_S^0 , called “nb_nolam” and “nb_vlike”, respectively. As their names suggest, “nb_nolam” is the likelihood of not being a Λ particle and “nb_vlike” is the likelihood of being a V0-like particle. A good K_S^0 candidate from “nisKsFinder” is the one with a low likelihood of being Λ particle and a high likelihood of being a V0-like particle, assuming the major backgrounds for K_S^0 is the mis-identified Λ among V0-like particles. By putting cuts on these two variables, a purification of K_S^0 can be made, see Figure 3-4. It can effectively reduce fake K_S^0 from cut-based selected candidates, however, there are a few disadvantages about this method. First, “NeuroBayes” is a commercial product that was developed over 10 years ago. The official support and update is stopped nowadays, so it’s not an ideal method for an experiment like Belle II that has a quite long prospective in operation. Second, the classification is based on a joint cut on two variables, which might make the cut values hard to choose, for example, two different cuts might have very close purity. Last but not least, the classification of K_S^0 is not the directly targeted output of the neuro-network. Instead, it classifies the V0-like particle and “ Λ ”. Besides, the computation speed of this method is not very optimized compared to other popular methods in today’s view.

In Belle II, such a dedicated K_S^0 classification tool is not implemented yet in BASF2 framework until 2019. Considered the limitation of Belle method, the development of K_S^0 classifier demands another algorithm and structure. The “Boosted Decision Trees” (BDT) are widely employed for multivariate classification and regression tasks in modern high energy physics field. Particularly, a speed-optimized

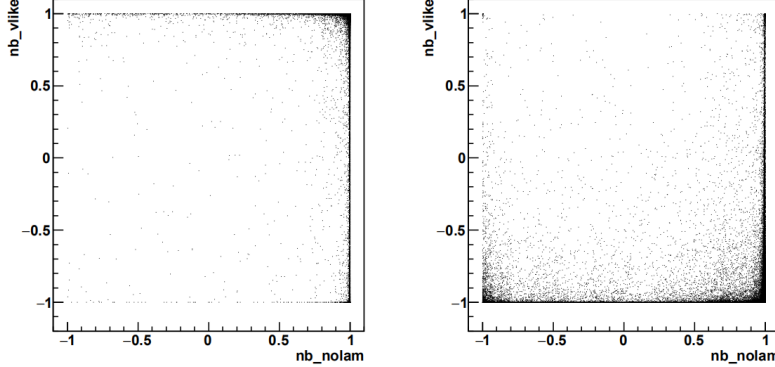


Figure 3-4: The distribution of two variables output from “nisKsFinder”: “nb_nolam” and “nb_vlike” for K_S^0 candidates from Belle signal MC. The left is from true K_S^0 and the right is from the fake K_S^0 . In Belle, the standard cuts for K_S^0 is $\text{nb_vlike} > 0.5$ and $\text{nb_nolam} > -0.4$ [19].

and cache-friendly implementation of such method called FastBDT (FBDT) is popularly used[32]. Compared to other popular classification algorithms such as TMVA, scikit-learn and XGBoost, FastBDT method is proven to be one order of magnitude faster during the training and applying phases[32]. The brief introduction of FastBDT algorithm is given in th section 3.2.2.

By using FastBDT algorithm, KsFinder in Belle II is expected to give a single output which directly presents the goodness of a candidate of being a true K_S^0 . Since the FastBDT algorithm depends on the variables that are different in signal and backgrounds, a set of training variables are selected based on K_S^0 decay topology. The details are discussed in section 3.2.3 and section 3.2.4. To be noted, K_S^0 variables used in the training of KsFinder might be differently distributed in different decay channels, therefore a KsFinder that is trained using MC sample from one channel may not be able to perform a good classification on the other. Thus, KsFinder is designed as a general package that provides a mode-dependent K_S^0 classification. It mainly consists of four parts which are “KsFinderSampler”, “KsFinderTeacher”, “KsFinderApplier” and “KsFinderTest”. KsFinderSampler is a function that automatically generates training and/or testing sample from mDST files where the default “std-Kshort:merged” is used as section 3.1 discussed. KsFinderTeacher is responsible for using variables to perform training of the FastBDT model and generate a weight file

containing all the nodes information in ROOT format, which also contains a function to communicate with BASF2 central database (see section 2.8.4) in case that users need to share or download others’ weight file in their own analysis. KsFinderApplier can apply the weight file generated by KsFinderTeacher (or downloaded from BASF2 central database) to the independent data sample and assign each K_S^0 candidate a goodness index so that users can use it as a single cut value in the further analysis. KsFinderTest is the evaluation function that can use a test sample to check for over-training, efficiency, purity and so on, based on the output of KsFinderApplier. By providing MC sample(s) from a certain decay mode(s), users can easily generate their own weight file(s) of K_S^0 classification that suits different decay modes despite K_S^0 variables distribution may be varied. The typical workflow is demonstrated in section 3.2.5. Such design largely improves the flexibility of KsFinder compared to Belle MVA tool which indirectly classify K_S^0 with two outputs.

3.2.2 FastBDT algorithm

As the basic component of BDT, a general DT (decision tree) performs classification using a number of consecutive cuts at each tree nodes, where tree nodes are distributed on the layers of a tree. The maximum number of the layers is called “depth of tree” and it’s a hyper-parameter of a DT. Each data point contains labels (variables) called “features” in DT. There are generally two phases in using DT for classification. One is “training” (or “fitting”) phase that determines the best cut at each nodes. The other is called “applying” phase that uses a trained DT to classifier a new data set. In training phase, training data points are fed to a DT and separated based on their features. At each node with a cut value, a cumulative probability histogram (CPH) can be defined by counting the signal and background data points. The histograms are used to determine the separation gain for a cut value at each position in these histograms. The feature and cut value (or equivalently bin) with the highest separation power are used as the cut for the node. Hence, each cut value locally maximizes the separation gain between signal and background on the given training sample. Eventually, on the last layer (called terminal layer), the signal fraction of all

training data points in the same terminal node is used for the signal probability for a testing data point which ends up in the same terminal nodes, shown as Figure 3-5. In applying phase, a new data set, such as a test sample, is fed to the trained DT with fixed cut values at each nodes, to evaluate the performance of a DT or use it to separate the signal and background.

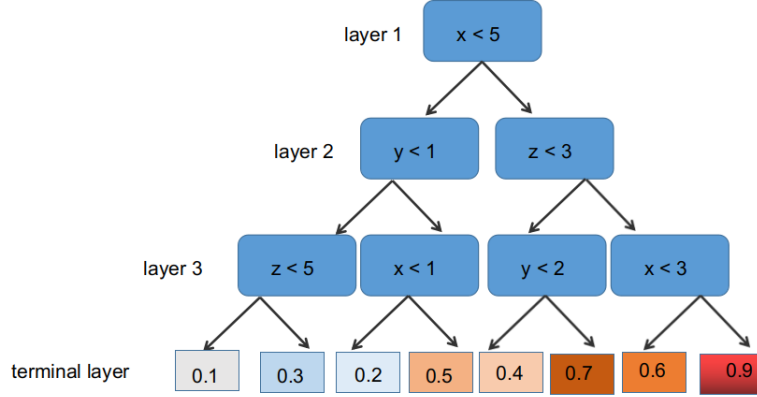


Figure 3-5: Basic structure of a DT with depth = 3 and labels (features) of x,y,z. The terminal layer contains training data points and are separated by cuts on layer 1 to 3. The number (color demonstrated) is the signal fraction of training data points in each terminal node, which is used for testing data points signal probability.

The mathematical idea behind this method is to treat the data points as a data set defined on a multi-dimension hyper-space. As long as the signal/background data points show certain concentration in a sub-region of the hyper-space, it's possible to locally increase the signal fraction by consecutively cutting on the edge where signal and background are separated. The cut on labels at each node is the edge of the sub-region. A very deep DT (too many layers) means the edges of the sub-region of the hyper-space is cut too finely so that even small statistical fluctuation could be separated. Therefore, training data points in the sub-region can give a over-trained signal fraction that is unrealistically high. As a result, the classifier performs poorly on new data points since the fluctuation is randomly occurred in new data set. There are pruning algorithms which automatically remove cuts prone to over-training from a DT, details can be found here [33].

Avoiding the over-training of a DT limits the depth of a tree strongly. For a

problem of K_S^0 classification, the number of observables (features) is much more than the usual tree depth (a few layers). A single DT can only roughly separate the signal and background and thus, it's called a weak-learner. To improve the separation power, a sequence of many shallow DTs is formed during the training phase. For all the DTs, a negative binomial log-likelihood loss-function is minimized in the training phase. By using the results from many DTs (many weak learners), a well-regularized classifier with large separation power is constructed. The number of trees N is called “boosting steps”, which is also the hyper-parameters for the training model. Such improved model is called “Boosted Decision Trees” (BDT). There are a few different strategies to further optimize the performance of BDT such as “Gradient Boost Decision Trees” (GBDT) and “Stochastic Gradient Boost Decision Trees” (SGBDT) which use different methods to define the model output or increase the training speed, details are discussed here[34].

The FastBDT (FBDT) implements a optimized algorithm from a derived SGBDT method [35] and gain an order of magnitude faster execution time. FBDT reduces CPU time on CPH for tree nodes by using binned values for comparison to avoid floating-point data calculation. It uses “struct of arrays” that leads to a faster pre-cached CPU memory access pattern. The comprehensive comparison in terms of speed in fitting and applying phases between FastBDT and other popular methods such as XGBT, TMVA and scikit-learn is described in here[32].

3.2.3 Decay Topology of $K_S^0 \rightarrow \pi^+ \pi^-$

As introduced in section 3.2.1, the first step for developing K_S^0 MVA classification is to determine the input variables for FastBDT algorithm that can represent the decay features of K_S^0 against possible backgrounds. The remaining background of $K_S^0 \rightarrow \pi^+ \pi^-$ after the cut-based reconstruction comes from different sources, including the false combination of tracks (including π^\pm misidentification), V0-like particle misidentification and self-looped tracks. For instance, a D^0/D^* from a B decaying to $K\pi$ with K misidentified as π , could give a false combination of tracks.

On the other hand, it's also possible that both of two tracks are correctly identified

as π^\pm but they are not from the same mother particle, or the mother is not a K_S^0 particle due to the missing of other daughters, such as $D^+ \rightarrow K_S^0(\rightarrow \pi^+\pi^-)\pi^+$. The decay shape resembled the above cases are illustrated in Figure 3-6.

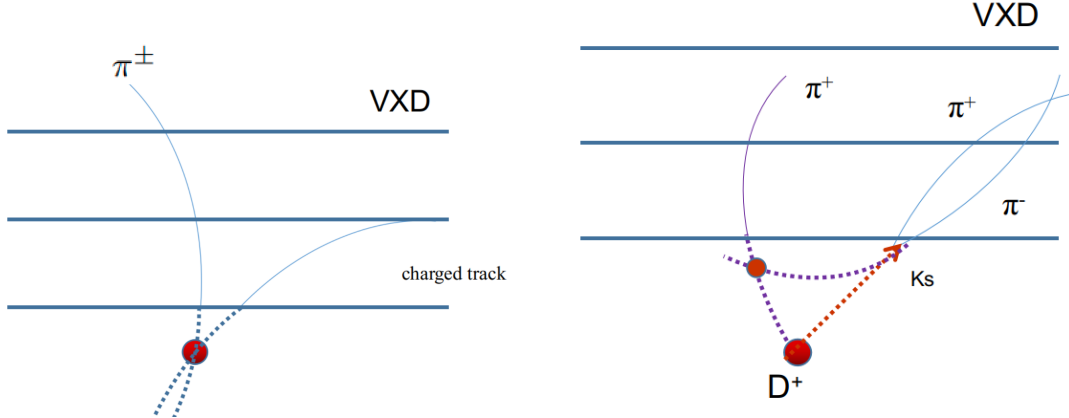


Figure 3-6: The left shows the case when a charged track (not π^\pm) combined with a true pion to form a fake K_S^0 , the right shows the case when two daughters are correctly reconstructed as pions but not from the correct mother particle (the smaller red dot), which is falsely taken as a K_S^0 .

The V0-like particles mainly refer to K_S^0 , Λ and γ . $\gamma \rightarrow e^+e^-$ yield is significantly lower than the other two types and the mass difference between pion and electron is very large, so the PID values can be used to well-distinguish them. As for the contribution of $\Lambda \rightarrow p^+\pi^-$, it happens when the positive charged tracks (proton track) is wrongly identified as π^+ , see Figure 3-7 left. The key observable to distinguish this background is the invariant mass of mother particle, which is 1.115 Λ GeV, much larger than the K_S^0 . The number of left-over Λ after the cut-based reconstruction in section 3.1 is small, and can be further reduced by rejecting the candidates whose positive charged daughter has $\text{PID}(\pi^\pm)$ smaller than $\text{PID}(p)$.

When a charged pion only carries a minimal of its mother's transverse momentum p_T , the curvature of its track may form a self-loop of which radius is comparable with the size of Belle II detector (mainly VXD and CDC). In this case, one charge pion could leave two charged tracks candidates with the opposite charge and similar p_T , with a possibility to form a converged vertex to form a fake K_S^0 , see Figure 3-7 right.

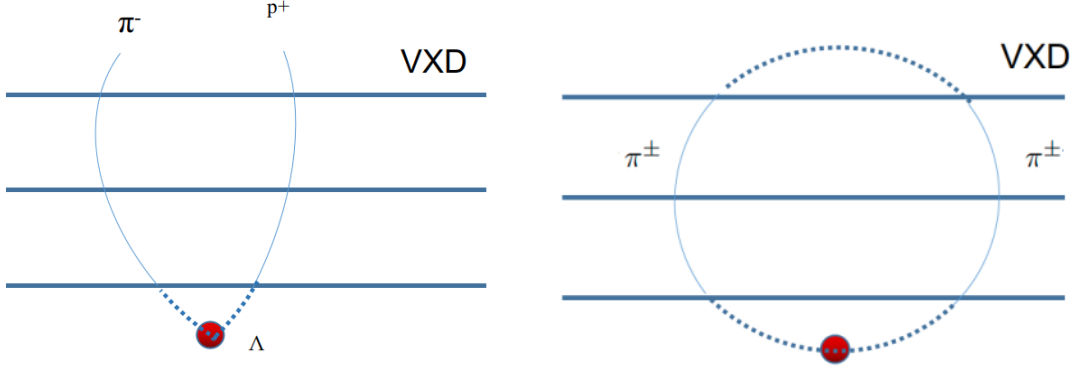


Figure 3-7: The left shows the $\Lambda \rightarrow p^+\pi^-$ decay shape that can be treated as K_S^0 , the right shows a self-loop formed by a low p_T charged pion reconstructed as two separated tracks with a vertex.

3.2.4 Determination of training observables from K_S^0 decay

Given the characteristics of $K_S^0 \rightarrow \pi^+\pi^-$ discussed in the previous section, a set of variables as training features of KsFinder can be selected. The set includes variables related to K_S^0 kinematics, decay shape parameters, particle identifications and detector hits information. The summarized information of training variables is listed in Table 3.3.

K_S^0 variables	Meaning
cosVertexMomentum	cosine between K_S^0 vertex and momentum direction (lab)
flight distance	K_S^0 flight distance projected on its momentum direction
significanceOfDistance	relative error of flight length from IP
cosHelicityAngleMomentum	cosine between π^\pm and K_S^0 (lab)
ImpactXY	Impact parameters in transverse plane for K_S^0
x, y, z, px, py, pz	K_S^0 vertex position and momentum
p_D1(D2)	momentum magnitude for $\pi^+(\pi^-)$
pionID, muonID	PID values of π^+
decayAngle_D1(D2)	angle between $\pi^+(\pi^-)$ and K_S^0 (K_S^0 CMS)
daughterAngle2body	angle between π^\pm (lab)
daughtersDeltaZ	Z-direction distance of two tracks helix
nSVDHits_D1(D2)	SVD detector hits of $\pi^+(\pi^-)$
nPXDHits_D1(D2)	PXD detector hits of $\pi^+(\pi^-)$
M, InvM	K_S^0 invariant mass before(after) vertex fit

Table 3.3: Summary of KsFinder input variables, where ‘‘lab’’ means angles in lab frame and ‘‘ K_S^0 CMS’’ means angles in K_S^0 rest frame. Other variables are based on lab frame by default.

The cosine between K_S^0 vertex and momentum direction (named “cosVertexMomentum”) is of the most importance because it demonstrates the best separation between a true and a fake K_S^0 . For instance, if a falsely reconstructed K_S^0 is made of two tracks, it’s likely that the momentum direction of the fake K_S^0 is not aligned with its vertex direction from IP. So the projection of vertex position of K_S^0 on the reconstructed momentum direction could be negative value for fake K_S^0 . While in case of a true K_S^0 , such projection is almost always a positive value, shown in Figure 3-8. This often happens when the two tracks taken as π^\pm are accidentally crossed, or due to the misidentified track(s). The abbreviations and importance rank of input variables from KsFinderTest function is shown in Table 3.4.

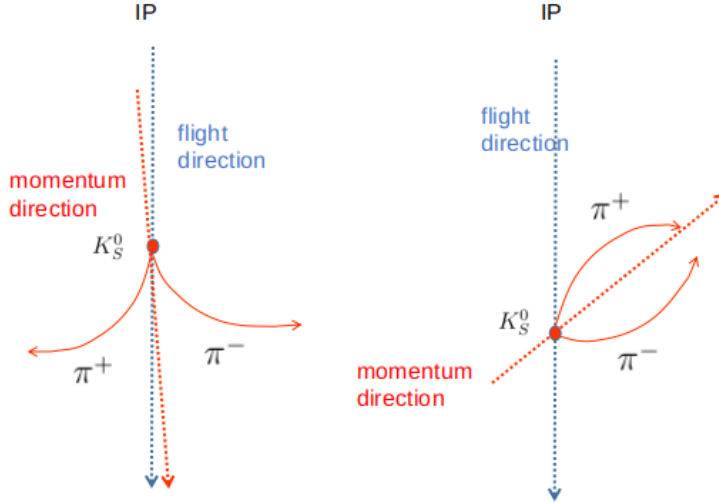


Figure 3-8: The left shows a true K_S^0 decay shape where the cosine angle of K_S^0 vertex position (blue dashed arrow) against reconstructed momentum direction (red dashed arrow) is positive. While the right shows a fake K_S^0 decay shape where cosine angle of K_S^0 vertex position against reconstructed momentum direction can be negative.

As a FastBDT method relies on the distribution of variables to calculate CPH, there are a few points to be checked before feeding the training data to the algorithm or applying the classification. First, the distribution of the observables should be different in true K_S^0 and the fake ones, so the FastBDT classifier can effectively separate the true and the fake K_S^0 at each node to maximize the separation gain, just as Section 3.2.2 discussed. Second, there will be a correlation among the training observables and they should also be different in signal and background. The boosting step will

create a sequence of shallow DTs whose structures are not same. Different correlations helps improve the performance of DTs in tuning of structure. For instance, a true K_S^0 flights longer due to larger momentum in general, so its daughters' detector hits number becomes fewer. Then these two observables have negative correlations in true K_S^0 . In case a fake K_S^0 , the flight length could be a deep outside of VXD but daughters may have full hits on SVD, without strong correlation, see Figure 3-9 . At last, one should also avoid using many observables with too strong correlations, since in this case, many DTs might have a potentially equivalent structure in the boosting step. Therefore, the separation power of many DTs doesn't gain any improvement. Conservatively speaking, if one variable shows a positive or negative correlation in percentage larger than 80% for over half of the all training variable, users may consider to remove it with very trivial loss on separation power. The correlation between variables are shown in Figure 3-9.

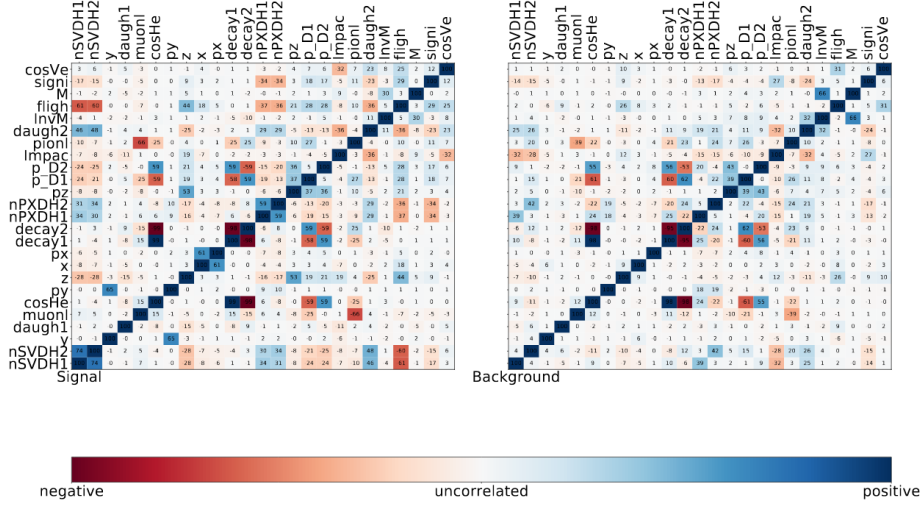


Figure 3-9: The correlation between input variables for KsFinder. As the given example, flight length has negative correlation with SVD hits in signal while uncorrelated in background. The correlations are in a reasonable level.

3.2.5 Training, Applying and Testing of KsFinder

The variables are internally registered inside the KsFinder so it can automatically retrieve their values from a mDST file in BASF2. The first step of using KsFinder is

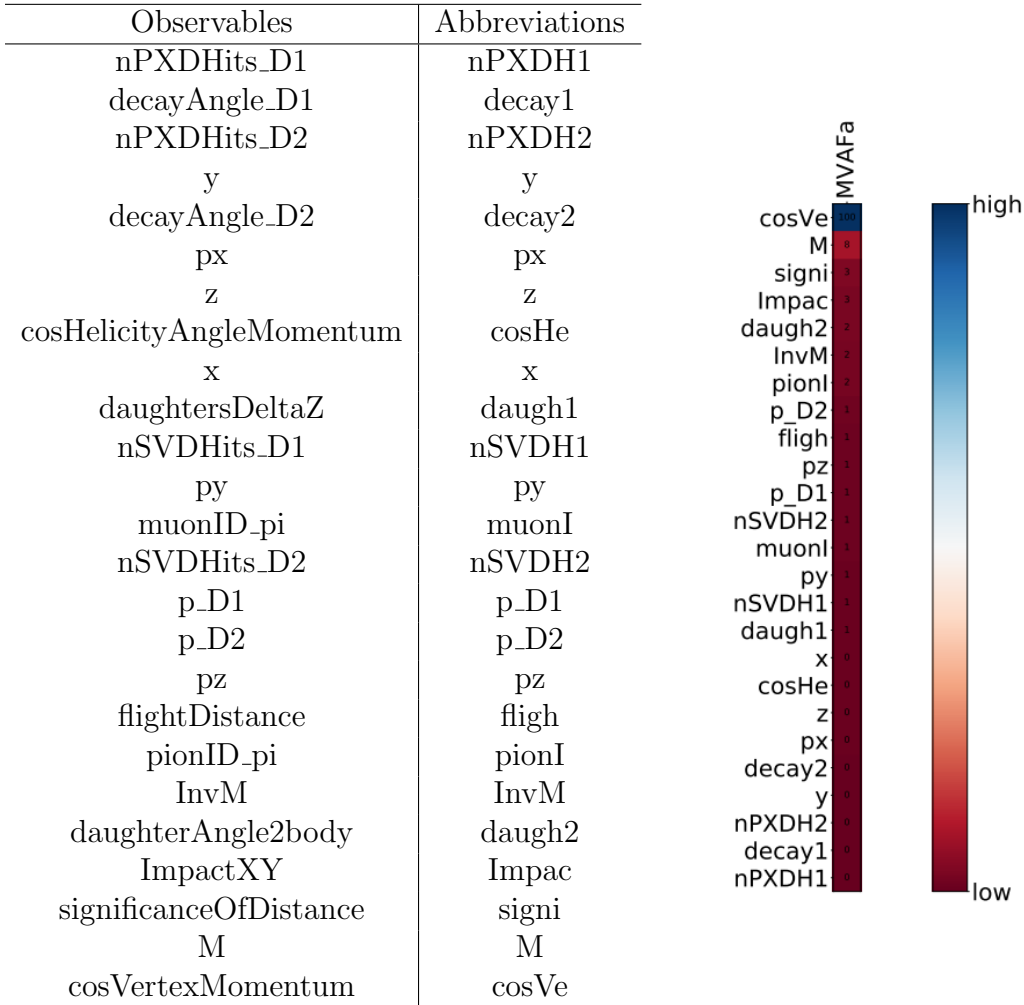


Table 3.4: The abbreviations (left) and importance rank (right) of input variables from “KsFinderTest”, where the most important variable is “cosVertexMomentum”.

to call KsFinderSampler on a MC sample to generate training and testing data sample. To show the flexibility and stability of KsFinder on different modes, KsFinderSampler extracts MC data points from both signal MC and generic MC (see MC definition in section 2.9), respectively. KsFinder configures that the depth of each DT is 3 and boosting steps is 200. In both MC samples, the ratio of true and fake K_S^0 is set to 1:1 and each component contains 200000 data points. The distribution of input variables in signal MC is shown in Appendix A.

To train the KsFinder, KsFinderTeacher function is called for the training samples from signal/generic MC and weight files are saved. To apply the classification of K_S^0 , KsFinderApplier reads in the testing samples of signal/generic MC and calculate output using saved weight files, so that each K_S^0 candidate is assigned with a goodness index named “FBDT_Ks”. It ranges from 0 to 1 where 1 stands for the best goodness. After the applying of KsFinder on the testing samples, KsFinderTest is called to check the performance and over-training of KsFinder on the testing samples, which will be discussed in the next section.

3.2.6 The Performance and Over-fitting check

To evaluate the performance of KsFinder on both signal/generic samples, signal efficiency and background rejection are first calculated by cutting on the different values on “FBDT_Ks”, as defined in Equation 3.1 and 3.2.

$$\text{signal efficiency} = \frac{\text{Number of true } K_S^0 \text{ with FBDT_Ks} > \text{cut value}}{\text{Number of all true } K_S^0} \quad (3.1)$$

$$\text{background rejection} = \frac{\text{Number of fake } K_S^0 \text{ with FBDT_Ks} < \text{cut value}}{\text{Number of fake true } K_S^0} \quad (3.2)$$

In order to check the performance of KsFinder as a classification tool, the ROC (receiver operating characteristics) curve is plotted, which shows the dependence of rejection power with respect to the signal purity. The larger area under a ROC curve means that the better performance is achieved since background rejection drops slower

when increasing the cut. The ROC curves and efficiency/background rejections are shown in Figure 3-10 and 3-11, where the former is for signal MC and the latter is for generic MC.

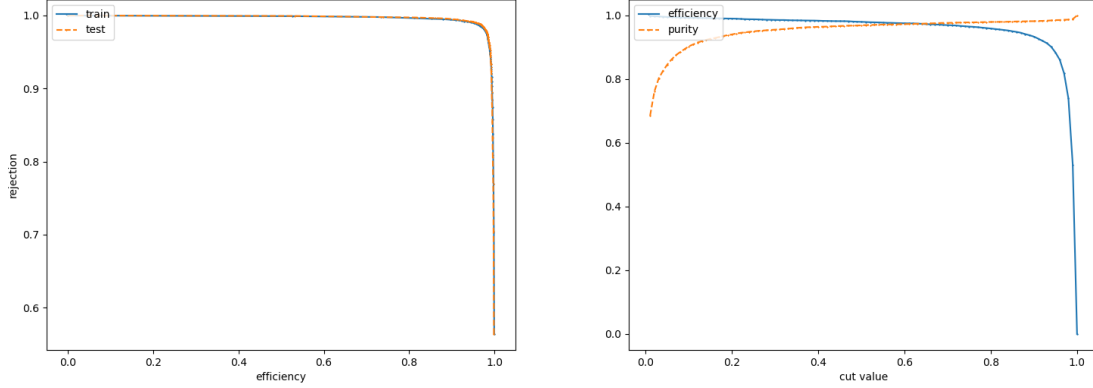


Figure 3-10: The left is ROC curve(blue for training and orange for testing) and the right is efficiency and purity (blue for efficiency and orange for purity) depending on cut of KsFinder output. Results are from $B^0 \rightarrow K_S^0 K_S^0 K_S^0$ sample.

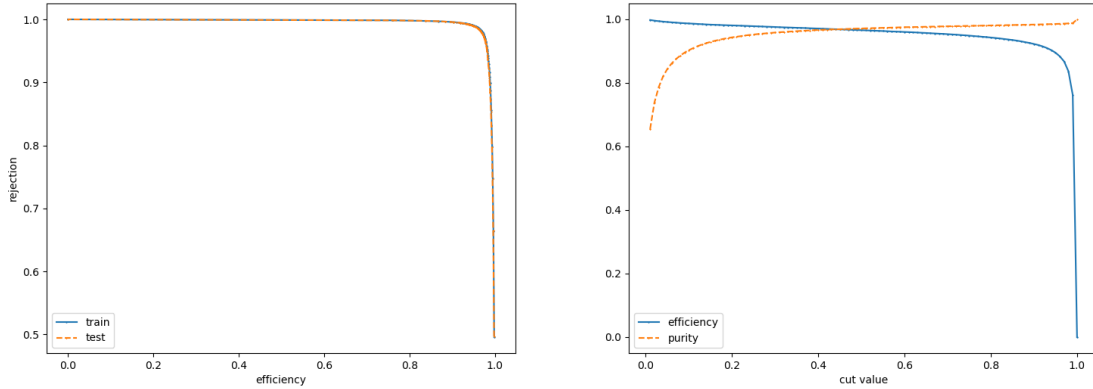
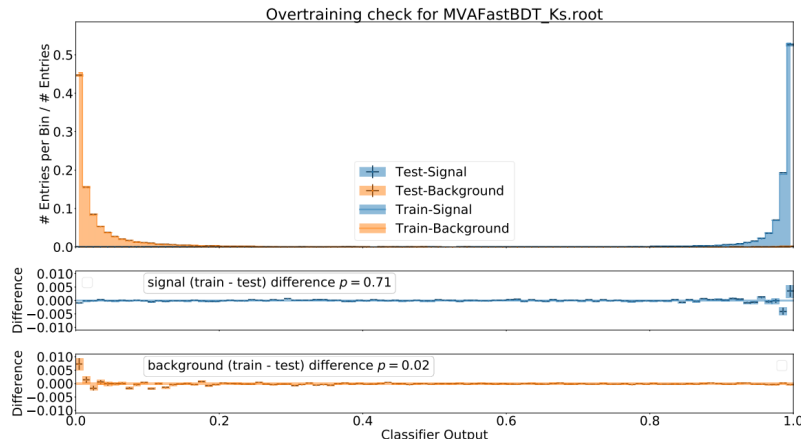


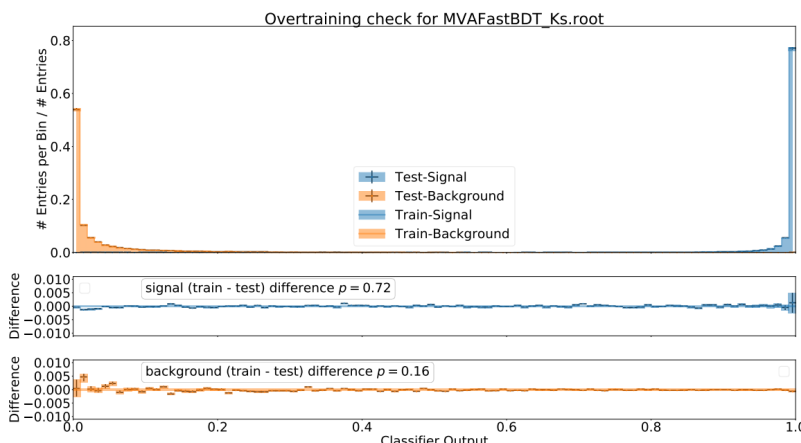
Figure 3-11: The left is ROC curve (blue for training and orange for testing) and the right is efficiency and purity (blue for efficiency and orange for purity) depending on cut of KsFinder output. Results are from B^0 generic decay sample.

The ROC curves show a good rejection power. With increasing the efficiency, the cut on the output of KsFinder is getting loose. The background rejection only starts to drop when the efficiency exceeds 90% in both training and testing sample.

To be noted, the curves are consistent in training and testing samples. In both signal MC and generic samples, KsFinder yields the similar ROC curves, hence the performance is in a good level in both modes. While the ROC curve has shown the absence of noticeable over-fitting in classification, the detailed check can be made by comparing the distributions of classifier output on true and fake K_S^0 in training and testing samples. Therefore, the distribution of signal/background data points in training/testing sample with respect to the KsFinder output is plotted, where a distinctive separation for both signal MC and generic MC is shown and no over-training (difference p is smaller than 1 in unit of %) is found, see Figure 3-12.



a) Over-fitting check for signal MC sample.



b) Over-fitting check for generic MC sample.

Figure 3-12: The over-training check based on the comparison between training/testing data points in both signal and generic MC.

In order to use the output of KsFinder, a cut value must be chosen. The cut value for “FBDT_Ks” is determined by maximizing the “Figure of Merit” (FOM), see Equation 3.3, where S and B is the number of true and fake K_S^0 after the cut, respectively. The FOM distribution depending on the cut value of FBDT_Ks is shown in Figure 3-13. The maximum FOM is achieved at $\text{FBDT_Ks} = 0.74$ in signal MC, which is going to be used as the cut value to further reject fake K_S^0 .

$$\text{FOM} = \frac{S}{\sqrt{S + B}} \quad (3.3)$$

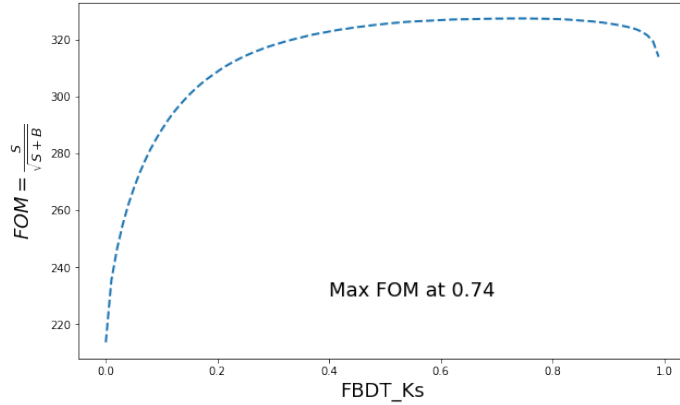


Figure 3-13: FOM of classifier output (FBDT_Ks) in signal MC, the maximum value is achieved at 0.74 and the curve is almost flat between $0.5 \sim 0.9$.

By comparing the fitted invariant mass (“M”) of K_S^0 before and after the application of this cut, it’s clear that the fraction of fake K_S^0 has been largely reduced and the majority of the true K_S^0 remains. In the signal MC sample, the true K_S^0 fraction before applying KsFinder cut is 39%, and 95.3% of them are kept after KsFinder applied. In the meantime, the fake K_S^0 fraction before applying KsFinder cut is 61%, and 97.6% of them are rejected after KsFinder applied. The purity of the K_S^0 candidates is improved significantly as shown in Figure 3-14.

3.2.7 Data Validation for Classifier

The results from MC studies show an excellent performance of KsFinder. However, such classification is based on the variables reconstructed using MC samples. As a

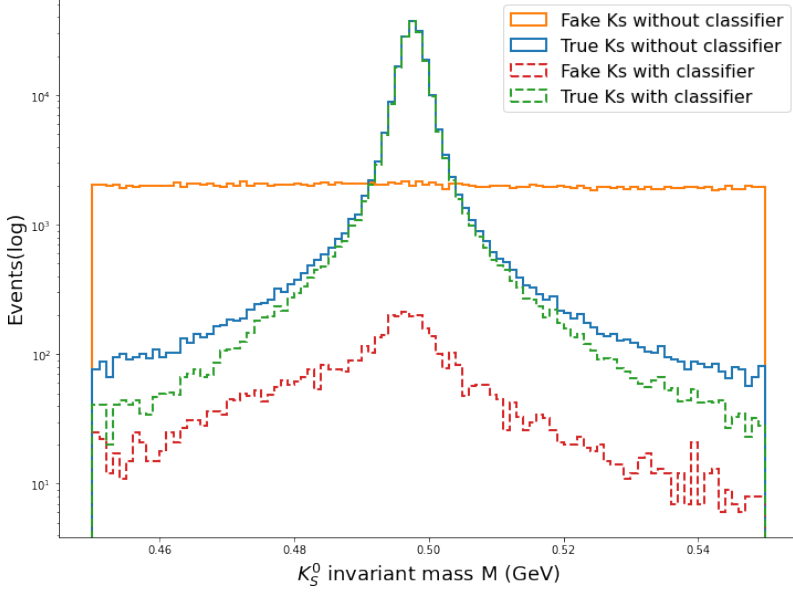


Figure 3-14: K_S^0 purity improvement with cut value of FBDT_Ks at 0.74 applied. The blue solid line is true K_S^0 without KsFinder and green dashed line is the true K_S^0 with KsFinder. The orange solid line is fake K_S^0 without KsFinder and red dashed line is fake K_S^0 with KsFinder. 95.3% of true K_S^0 are kept while 97.6% of the fake are rejected by the classification.

result, the validation of such a tool on the real experiment data is necessary. This would justify the usage of classifier on data and is also essentially helpful to check the potential discrepancy between MC and data.

The validation comes from the following aspects. First of all, since there's no “isSignal” truth in real data, there's no way to direct check performance on data. Since the FastBDT method is based on the distribution of training variables (CPH on each nodes), if these variables shows close distribution among MC and data, then the classification performance is expected to be close.

In addition, since K_S^0 candidates are used for further reconstruction of B^0 , its kinematics distributions, such as invariant mass and momentum, may change after applying KsFinder, so the validation that approves no clear bias on B^0 's variables that are used for signal extraction is required.

For validating KsFinder on data, a small data sample from Belle II early phase 3 operation experiment 7 and 8 in 2019 is used. The integral luminosity at $\Upsilon(4S)$ resonance for this data sample is about 5.17 fb^{-1} . MC13 sample is extracted from

generic B^0 decay with equivalent events number. There are two campaigns of MC included (MC12b and MC13, later one is the latest). Fig 3-16 shows the invariant mass and momentum distributions from data and MC samples, and full comparison of all training variables is included in Appendix B. Most of the distribution shows a good consistence before and after using KsFinder. It shows that kinematics of K_S^0 in data and MC yield fairly close distributions and no clear bias is seen by applying the KsFinder cut.

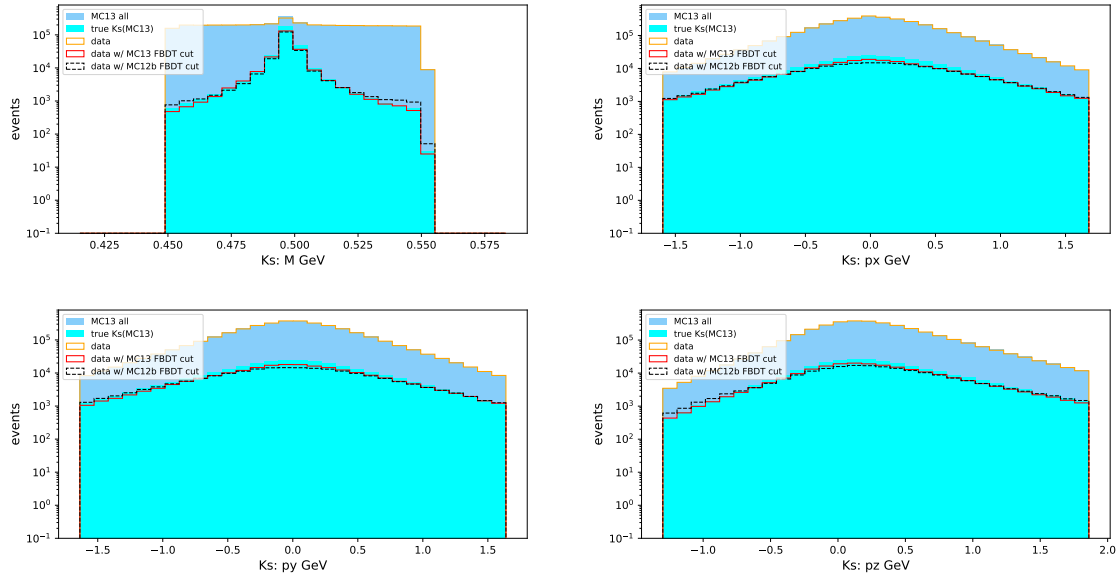


Figure 3-15: The distribution of invariant mass from daughters and the momentum of x,y,z direction. Blue bar is from all MC13, cyan bar is the true K_S^0 in it. Yellow step histogram is data with no cut, solid red data with MC13 trained cut, and the dashed is with MC12b cut. Experimental data has a good agreement with MC before and after applying the KsFinder.

3.2.8 KsFinder Effects on Kinematics Evaluation

Implementing KsFinder for K_S^0 may induce extra bias on the event numbers for K_S^0 . It's not easy to directly evaluate the impact of each variables in training towards the final signal yield because the output is non-linear dependence on those variables. However, we can directly use the output of KsFinder and introduce the scale factor when check the data and MC signal yields.

A fit on invariant mass M of K_S^0 candidates after varied cut on KsFinder output is done by modeling signal shape as double-Gaussian and background as Chebyshev polynomial. Significance is define as $S_{data/MC} = N_{signal}/N_{total}$ in data and MC from fitting using RooFit. A list of intervals of cut value on KsFinder output is made and the significance is calculated within each interval. Fitting results are shown in Fig 3.17 using loose and tight cut respectively. The fit plots in all cut intervals are included in Appendix C. Data/MC correction is defined as:

$$R = \frac{S_{MC}}{S_{data}} \quad (3.4)$$

The correction is defined by taking the R value within the chosen interval. Uncertainty of R is defined by the difference of maximum and minimum of R in all intervals. R is distributed as:

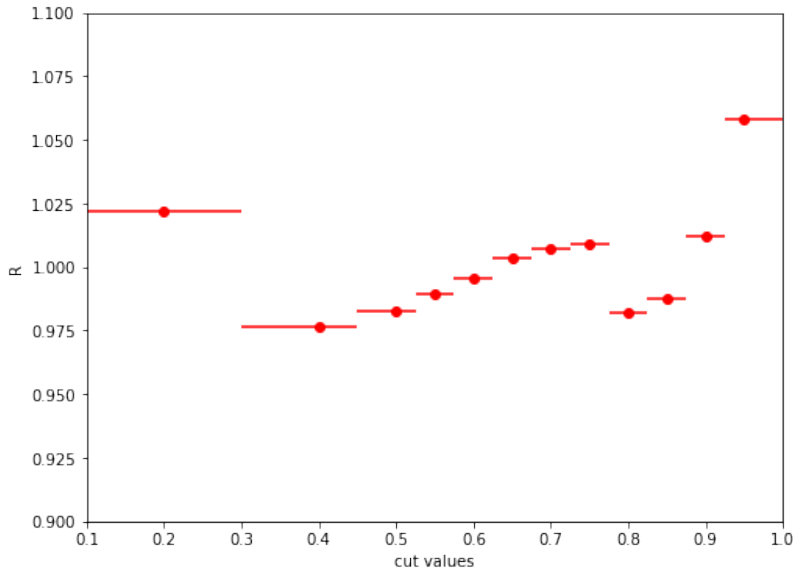


Figure 3-17: Data MC correction induced by K_S^0 classifier.

The R, for example in cut value 0.74 of maximum FOM, is $R = 1.009 \pm 0.081$. In $B^0 \rightarrow K_S^0 K_S^0 K_S^0$, the correction of B^0 events should be proportional to R to the three. Correction that is implemented for B^0 is $1.027^{+0.33}_{-0.18}$. In most of the cut intervals, the R is within 2.5% so the bias on K_S^0 numbers is very small.

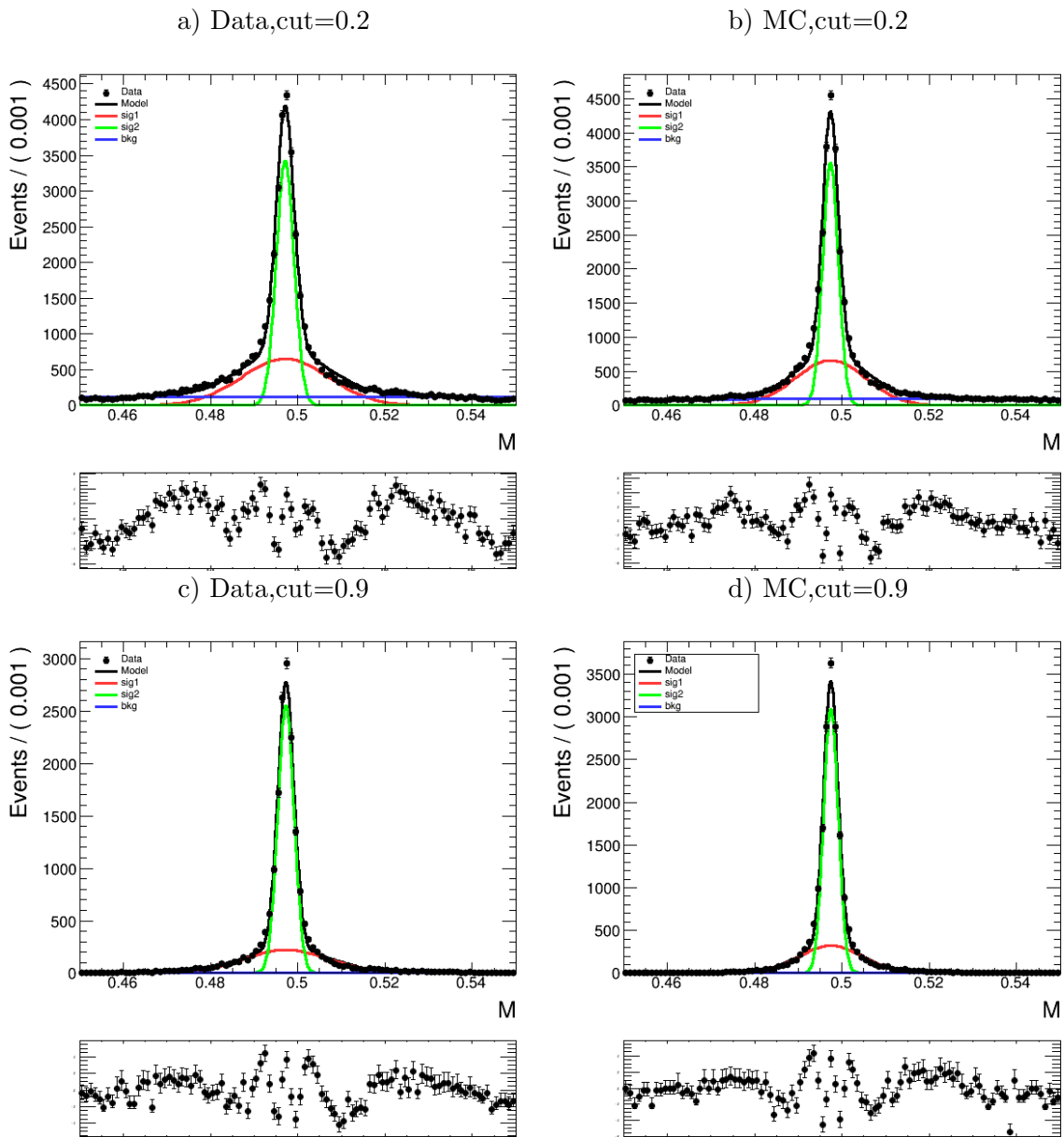


Figure 3-16: Invariant mass fit of K_S^0 using cut at 0.2(loose) and 0.9(tight) to calculate $S_{data/MC}$.

Chapter 4

Analysis strategies

4.1 Data Sample and Event Selection

As introduced in section 2.9, the branching fraction of $\mathcal{B}(B^0 \rightarrow K_S^0 K_S^0 K_S^0) = 6.0 \times 10^{-6}$. The simulation takes the $\Upsilon(4S)$ as the mother particle and generate its decay process to two scalar B^0 mesons with mixing. $B^0 \rightarrow K_S^0 K_S^0 K_S^0$ is simulated based on only the possible phase-space of kinematics that final states could have, which no CP violation is assigned for $\mathcal{S}(\sin 2\phi_1)$ and \mathcal{A} in both signal and generic MC.

4.1.1 K_S^0 Selection

K_S^0 reconstruction is first reconstructed by the cut-based reconstruction which contains a large fraction of fake candidates, as discussed in chapter 3. In addition, a momentum cut on K_S^0 is used considering distribution in $B^0 \rightarrow K_S^0 K_S^0 K_S^0$. Only the K_S^0 candidates with momentum larger than 0.05 GeV are selected, as shown in Figure 4-1. Next, the vertex fit of K_S^0 is performed using *TreeFit* package[36]. Using fitted K_S^0 momentum and energy, fitted invariant mass is different from the one obtained directly using daughters' 4-vector. This quantity often receives impact of the measurement uncertainties. If we check out the distribution of fitted invariant mass based on daughters' SVD hits as section 3.1 discussed, *SVD00* K_S^0 shows a large dispersion from the central region of the distribution of invariant mass after vertex

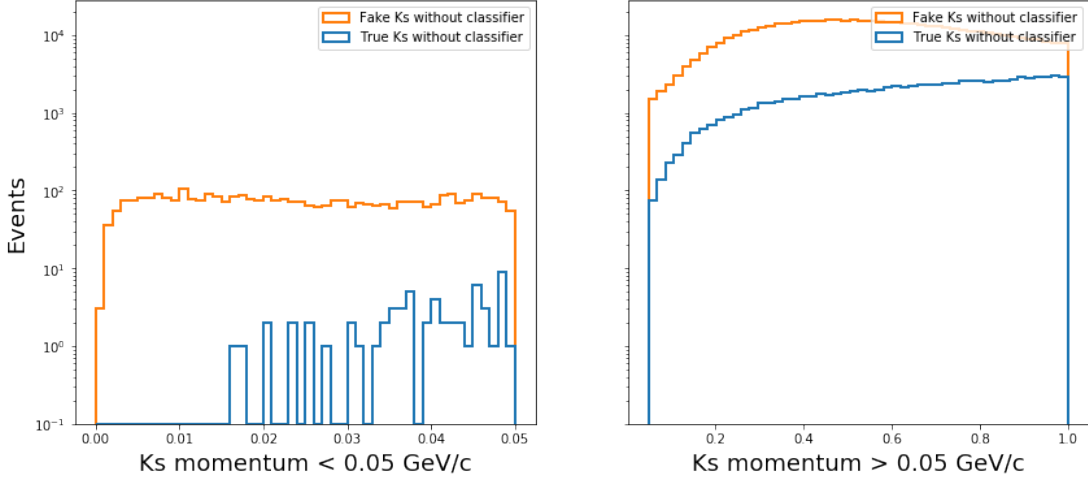


Figure 4-1: The distribution of K_S^0 momentum. Candidates smaller than 0.05 GeV/c are rejected. (Both plots shares the same y-axis scale on the left side.)

fit, while *SVD11* K_S^0 shows a small dispersion as shown in Figure 4-2. Therefore, considering the K_S^0 candidates with different SVD hits, see Figure 3-3 and Table 3.2, reflecting the different tracking quality of daughter π^\pm , the different cut on invariant mass $M_{\pi^+\pi^-}$ after vertex fit is applied depending on the SVD hits number of pion tracks. As shown in Figure 4-3, the sideband regions where fake K_S^0 is much higher than true K_S^0 are excluded. The cut windows are listed in Table 4.1. This improves the reconstruction purity.

In summary, K_S^0 are first reconstructed using BASF2 standard library with all converged vertex fit candidates are kept using *TreeFit*. Then we reject K_S^0 candidates with momentum smaller than 0.05 GeV/c. After this, tuned cuts on invariant mass after vertex fit for each K_S^0 based on their SVD hits of pions are applied according to Table 4.1. Eventually, only K_S^0 with “FBDT_Ks” larger than 0.74 are kept based on Figure 3-13.

K_S^0 type	SVD11	SVD10	SVD01	SVD00
$M_{\pi^+\pi^-}$ window (GeV)	(0.45,0.55)	(0.38,0.7)	(0.38,0.7)	(0.3,0.7)

Table 4.1: Invariant mass cut window after vertex fit for K_S^0 based on Figure 4-3.

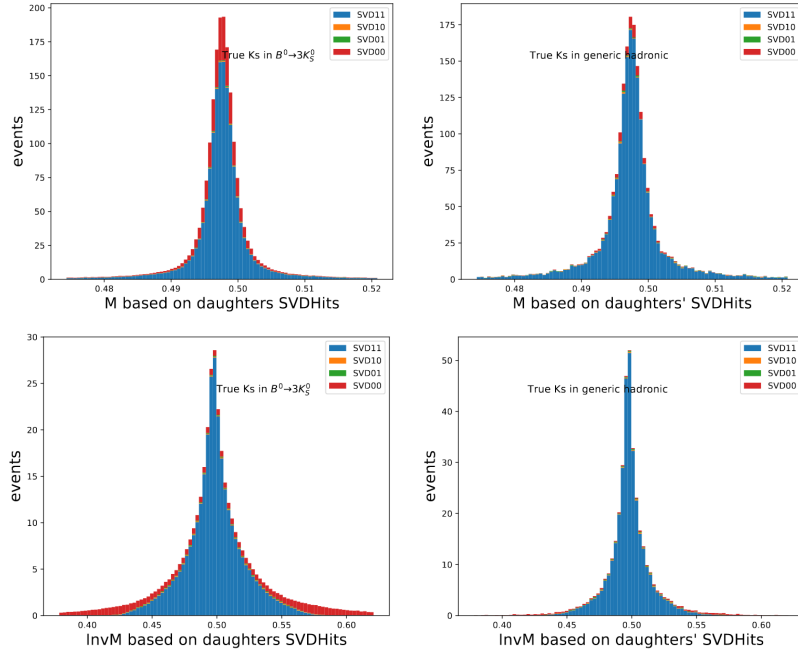


Figure 4-2: (Top two plots)The invariant mass from daughters' 4-vector, the left is $B^0 \rightarrow K_S^0 K_S^0 K_S^0$ signal MC and the right is generic MC; (bottom two plots)The invariant mass after vertex fit, the left is $B^0 \rightarrow K_S^0 K_S^0 K_S^0$ signal MC and the right is generic MC; In both cases, the red shows the clear dispersion on $SVD00$ type K_S^0 .

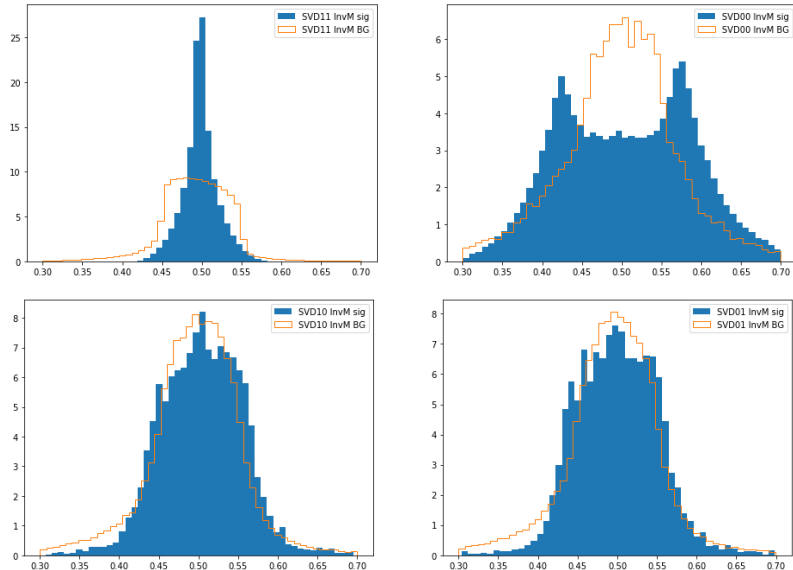


Figure 4-3: Invariant mass after vertex fit of K_S^0 , the sideband is excluded in each distribution to further reject fake K_S^0

4.1.2 B^0 Reconstruction

By combining three K_S^0 particles from selected dataset, we can reconstruct B^0 . The beam-constraint mass M_{bc} and energy difference ΔE are used to extract signal, as defined in Equation 4.1 and 4.2, respectively. For M_{bc} , s is defined as the invariant mass and p_B^* is the reconstructed B momentum, both in the center-of-mass frame of e^+e^- . For ΔE , E_B^* is the reconstructed energy in the center-of-mass frame of e^+e^- . These two variables are quite useful for discriminating signal and background events for hadronic B decay with fully reconstructed final states. In Belle II, the B^0 candidates with $M_{bc} > 5.2$ GeV and $|\Delta E| < 0.2$ GeV are requested to be reconstructed. The B^0 vertex fit using *TreeFit* is performed on each B^0 candidate and only B^0 with converged vertex fit result is kept (by a very loose cut of "chiProb > 0.001"), which is essential to obtain the decay vertex positions of B mesons for further CP violation analysis. When multiple B^0 candidates are obtained in a single event, the best candidates selection (BCS) is performed by ranking their vertex fit quality. Since the BCS is based on the vertexing quality that might introduce bias in the vertex positions for CP fit, we check the distribution of the vertex χ_2 , as shown in Figure 4-4 top right where the data and generic MC present a good consistence within 1σ on average. The distribution of candidates number per event without BCS is shown in top left of Figure 4-4 as well, showing an agreement between data and generic MC within 1σ . The distribution of candidates per event is also in an agreement with that from signal MC (bottom left of Figure 4-4). The 2D distribution of M_{bc} and ΔE from $B^0 \rightarrow K_S^0 K_S^0 K_S^0$ signal MC is shown in Figure 4-4 bottom right, where the correlation factor is about 15% between two observables.

$$M_{bc} = \sqrt{\frac{s}{4} - p_B^{*2}} \quad (4.1)$$

$$\Delta E = E_B^* - \frac{\sqrt{s}}{2} \quad (4.2)$$

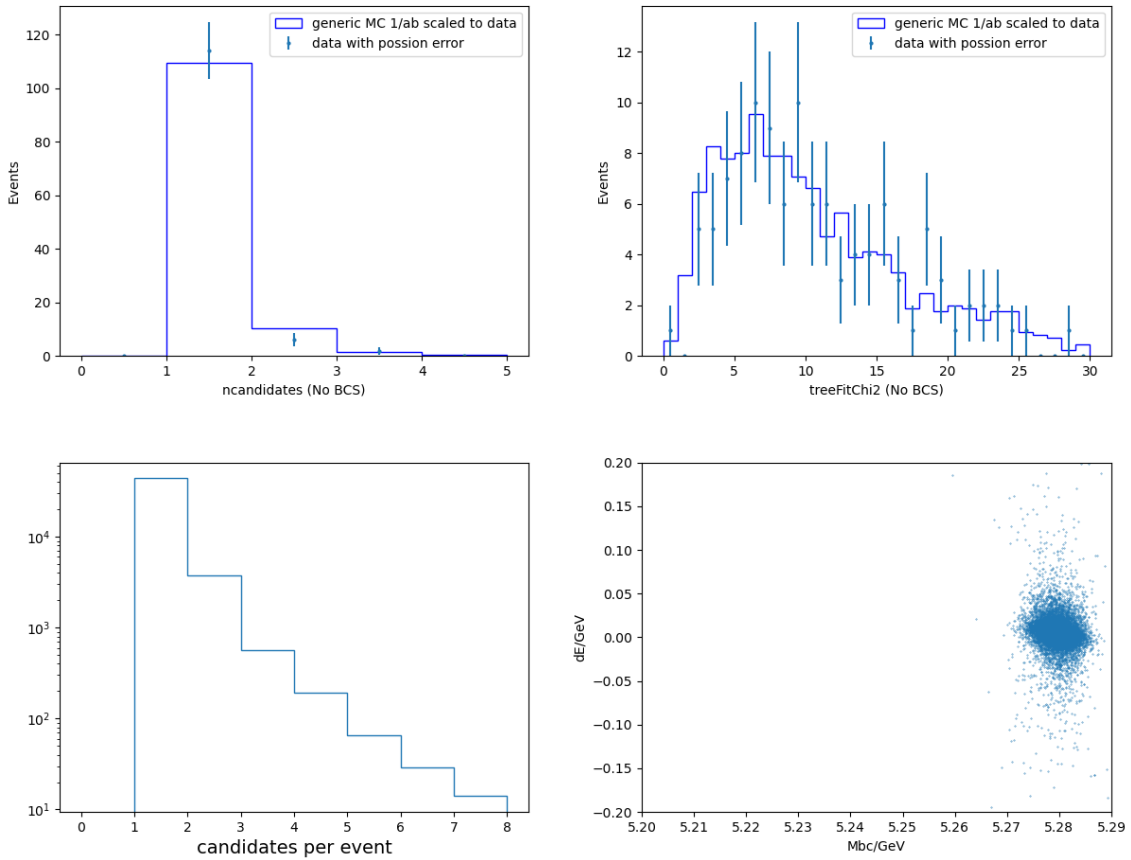


Figure 4-4: Top left is the candidates per event in data and generic MC before the BCS. Top Right is the χ_2 for data and generic MC before BCS. Bottom left is the number of candidates B^0 per event from signal MC. Bottom right is the 2D M_{bc} and ΔE distribution from signal MC.

4.1.3 Continuum Suppression

The production cross-section of $B\bar{B}$ from $\Upsilon(4S)$ receives a sizable contribution from other flavor of quarks other than b quark. This calls a demand to distinguish a specific $B\bar{B}$ decay events from combinatorial background from $e^+e^- \rightarrow q\bar{q}$, so called continuum suppression (CS). The rejection is essential because it's the dominated background. In the case of $b \rightarrow s$ charmless decay like $B^0 \rightarrow K_S^0 K_S^0 K_S^0$, the number of continuum background can exceed the signals by a few orders of magnitudes without suppression. In a $B\bar{B}$ event, two mesons are produced almost at rest in the CMS frame since the resonance state $\Upsilon(4S)$ is just slightly lighter than beam energy. As a result

, decay products are emitted more isotopically, compared to continuum background. The ARGUS and CLEO collaboration[37] developed a set of variables to suppress the continuum, which has also been implemented into BASF2 framework.

CLEO cones momentum can be presented as Equation 4.3, where p_i is momentum of i-th particle in Rest-Of-Event (ROE) particles in a event except for the ones used to reconstructed CP -side B^0 , θ_i is angle against momentum thrust of reconstructed CP -side of B meson.

$$L_n = \sum_{i \in ROE} p_i \times |\cos\theta_i| \quad (4.3)$$

Besides, the modified Super Fox-wolfram momentum named KSFW momentum, are calculated in each event. The KSFW momentum are defined as shown in Equation 4.4.

$$KSFW = \sum_{l=0}^4 (R_l^{so} + R_l^{oo}) + \gamma \sum_{n=1}^{N_t} |P(t)_n| \quad (4.4)$$

where the first term is shown in Equation 4.5.

$$R_l^{so} = \frac{\alpha_{cl} H_{cl}^{so} + \alpha_{nl} H_{nl}^{so} + \alpha_{ml} H_{ml}^{so}}{E_{beam}^* - \Delta E} \quad (4.5)$$

when l is odd in Equation 4.5:

$$H_{nl}^{so} = H_{ml}^{so} = 0 \quad (4.6)$$

and H_{cl}^{SO} is defined as shown in Equation 4.7:

$$H_{cl}^{so} = \sum_i \sum_{jx} Q_i Q_{jx} |p_{jx}| P_l(\cos\theta_{i,jx}) \quad (4.7)$$

i runs over B daughter particles and jx for other particles in ROE. Q is charge and p_{jx} is momentum for each particle. $P_l(\cos\theta_{i,jx})$ is the i -th order Legendre polynomial of cosine of i and jx -th particles. On the other hand, for l is even, H_{xl}^{SO} can be written

in Equation 4.8.

$$H_{xl}^{so} = \sum_i \sum_{jx} |p_{jx}| P_l(\cos\theta_{i,jx}) \quad (4.8)$$

The second term in Equation 4.4, when l is odd, can be defined as Equation 4.9.

$$R_l^{oo} = \sum_j \sum_k \beta_l Q_j Q_k |p_j| |p_k| P_l(\cos\theta_j, k) \quad (4.9)$$

j and k runs over ROE particles and others are same as Equation 4.7. For an even l :

$$R_l^{oo} = \sum_j \sum_k \beta_l |p_j| |p_k| P_l(\cos\theta_j, k) \quad (4.10)$$

β is Fisher coefficients to be determined. Using above definitions, we can form the possibility density functions for KSFW, cosine angle against B meson thrust $\cos\theta_B$ and ΔZ of two side vertices. Then based on each event's variables' value, we can calculate a ratio \mathcal{R} as Equation 4.11, where the likelihood L of signal(L_S) and background(L_B) are obtained from the possibility density functions defined in Equation 4.12. The \mathcal{R} is:

$$\mathcal{R} = \frac{L_S}{L_S + L_B} \quad (4.11)$$

$$L_{S/B} = P(KSFW)_{S/B} \times P(\cos\theta_B)_{S/B} \times P(\Delta Z)_{S/B} \quad (4.12)$$

where P is probability density function for signal and continuum, depending on the discriminating variables in the parentheses. For example, the distribution of a variable called R_2 shown in Figure 4-5 where the possibility density function is different for signal and continuum events in generic MC.

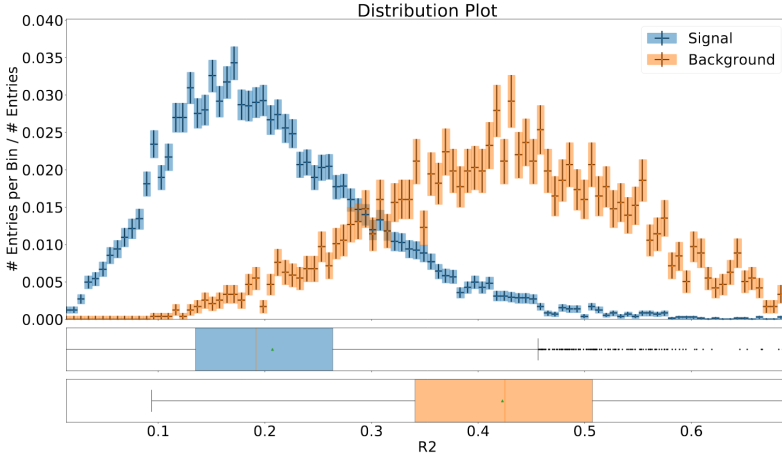


Figure 4-5: R_2 is the ratio of the second to the zeroth KSFW momentum in Equation 4.4. Its distribution in generic MC sample which serves as the highest weight as a variable in discriminating the continuum events, having a quite different distribution between signal and background.

In order to maximize suppression power in this analysis, these variables (KSFW, CLEO cone momentum and angular distributions) are combined as an input for FastBDT classifier. The targeted variable is the continuum event truth. The MC samples using signal $B\bar{B}$ events from signal MC and continuum events from generic MC ($q\bar{q}$ component) are prepared in a ratio of their cross-section at $\Upsilon(4S)$ energy. The same events reconstruction procedures for B^0 is applied for both MC samples. Events passing the reconstruction for B^0 using M_{bc} and ΔE are used for training the continuum suppression classifier. The fraction of signal and background is set to 1:1 during the training. The output of continuum suppression classifier is renamed as “FBDT_CS”. Then we determine the cut value at 0.66 based on the maximum of *FOM* curve, as shown in Figure 4-9. The variables used in training are listed in Table 4.2 with their abbreviations and the rank of important variables is in Table 4.3.

The correlation between these training variables are shown in Figure 4-6. The correlation among the variables are varied in signal and background. The ROC curve and the efficiency/purity with respect to the classifier output are shown in Figure 4-7.

Overtraining check is made by comparing the distribution of signal and background depending on the classifier output in both training and testing samples. The

Table 4.2: Variables and the abbreviations for CS.

Observables	Abbreviations
CleoConeCS(9,)	CleoC1
KSFWVariables(hoo1,)	KSFWV1
CleoConeCS(7,)	CleoC2
CleoConeCS(5,)	CleoC3
KSFWVariables(hso22,)	KSFWV2
KSFWVariables(hoo3,)	KSFWV3
CleoConeCS(4,)	CleoC4
KSFWVariables(hoo4,)	KSFWV4
CleoConeCS(3,)	CleoC5
CleoConeCS(6,)	CleoC6
CleoConeCS(8,)	CleoC7
KSFWVariables(hso14,)	KSFWV5
KSFWVariables(hso00,)	KSFWV6
KSFWVariables(et,)	KSFWV7
KSFWVariables(hso24,)	KSFWV8
KSFWVariables(hso04,)	KSFWV9
KSFWVariables(hso20,)	KSFWV10
KSFWVariables(mm2,)	KSFWV11
KSFWVariables(hoo2,)	KSFWV12
thrustOm	thrus1
cosTBz	cosTB1
CleoConeCS(1,)	CleoC8
CleoConeCS(2,)	CleoC9
KSFWVariables(hso02,)	KSFWV13
KSFWVariables(hoo0,)	KSFWV14
KSFWVariables(hso12,)	KSFWV15
KSFWVariables(hso10,)	KSFWV16
cosTBTO	cosTB2
thrustBm	thrus2
R2	R2

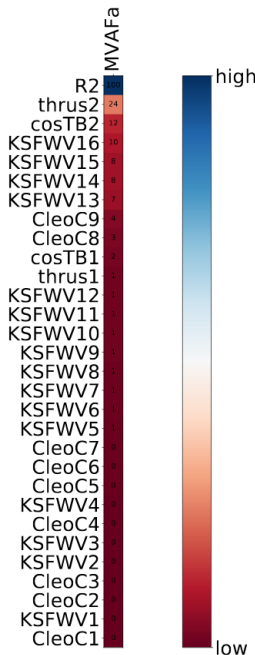


Table 4.3: The rank of important variables for CS.

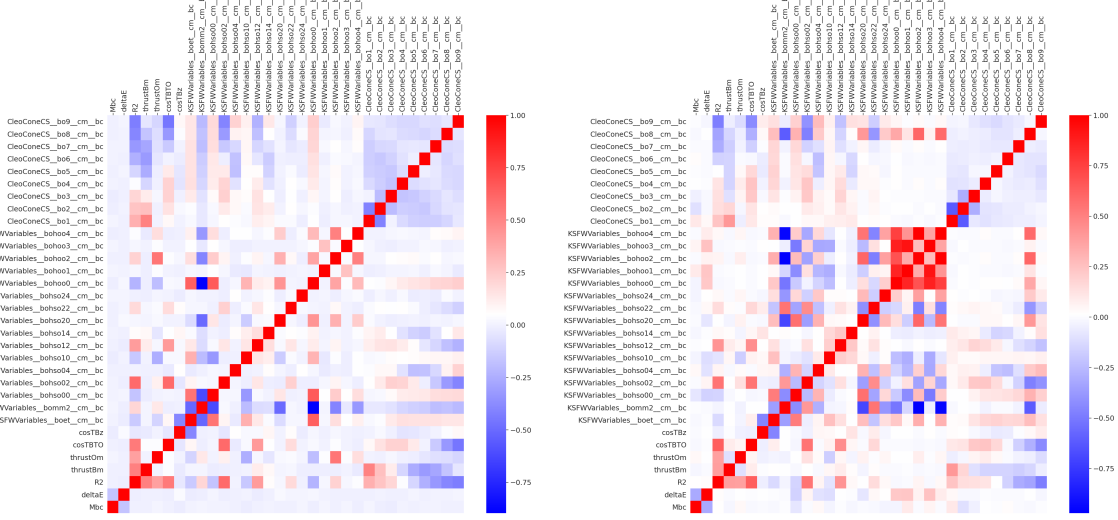


Figure 4-6: The correlation in variables for continuum suppression. The left is for signal and the right is for background.

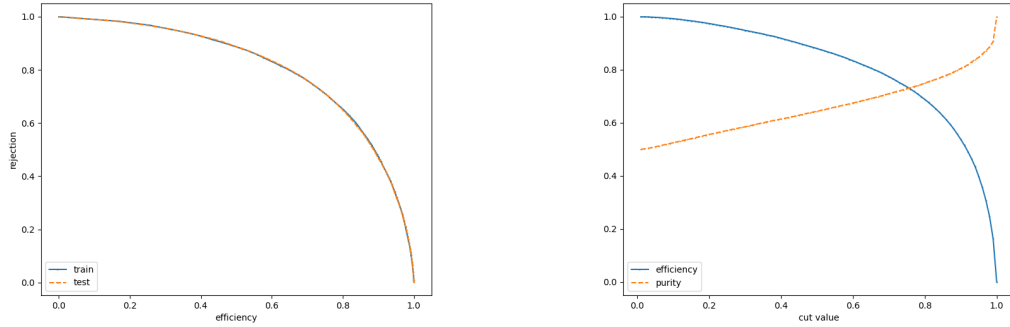


Figure 4-7: The left is the ROC curve (blue for training and orange for testing) and the right is the efficiency(blue) and purity(orange) regarding the classifier output “FBDT_CS”

testing samples show about 1% lower in each bin for both signal and background events, which is within the acceptable range.

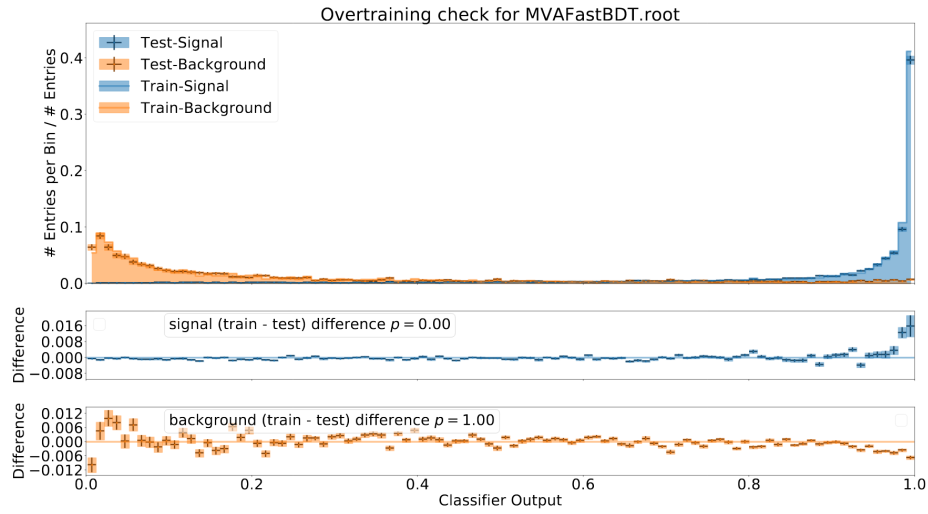


Figure 4-8: Over-training check of continuum classifier, where a very small difference in training and testing (1%) is shown.

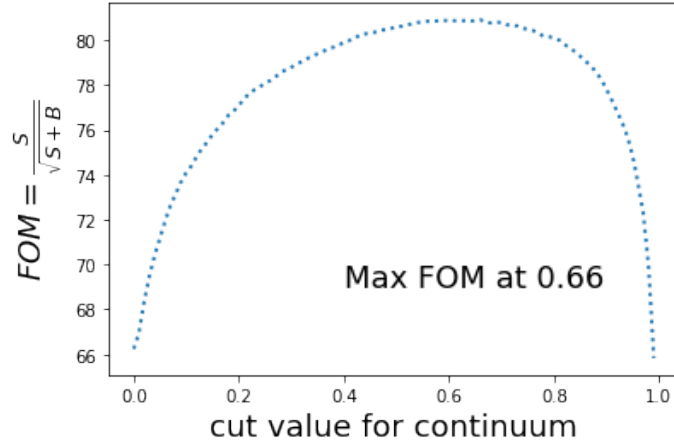


Figure 4-9: FOM depending on the cut value of continuum classifier output, cut value at 0.66 is used for continuum suppression.

The summary of B^0 selections is listed in Table 4.4, including the application of KsFinder (by “FBDT_Ks”) and continuum suppression (by “FBDT_CS”).

B^0	M_{bc}/GeV	$\Delta E/\text{GeV}$	chiProb	Rank	FBDT_CS	FBDT_Ks
Selection	$> 5.20 \& < 5.29$	$ \Delta E < 0.2$	> 0.001	= 1	> 0.66	> 0.74

Table 4.4: B^0 selection criteria, “chiProb” is from B^0 vertex fit and “Rank” is from best candidate selection.

Explicitly, the reconstruction performance of B^0 is summarized in Table 4.5, the efficiency, purity, fraction of multiplicity events and best candidates fraction of B^0 is slight improved in Belle II compared to Belle.

event selection	efficiency	purity	f_{MB}	BCS
Belle Standard	35%(33%)	96%(99%)	6%(6%)	83%(96%)
Belle II (BG1)	36%(34%)	96%(98%)	(4%)(4%)	95%(96%)
Belle II (BG0)	40%(36%)	96%(99%)	(3%)(3%)	97%(97%)

Table 4.5: The efficiency is defined by the fraction of best candidates among the MC input number. Purity is the fraction of true B^0 in best candidates. f_{MB} stands for multiple B^0 events fraction in true signal events. BCS is the fraction of best candidates being a true signal. All values in the parenthesis are calculated in $|M_{bc}| - 5.28 < 0.1$ and $|\Delta E| < 0.1$, called as “signal region” where efficiency is lower but purity is higher, compared to the full range of M_{bc} and ΔE in Table 4.4.

4.1.4 Resonance Background

Besides the major contribution from continuum background, charmonium resonance that mediates through $b \rightarrow c$ transition brings odd CP eigenvalue in the final states as same as $B^0 \rightarrow K_S^0 K_S^0 K_S^0$. Monitoring their contribution is also important. Basically, one needs to check the resonance states formed by two K_S^0 with corresponding invariant mass. In $B^0 \rightarrow X(K_S^0 K_S^0)K_S^0$, there are two types of resonant events that give out same final states, one is resonant signal and the other is resonant background. For $b \rightarrow s$ transitions as resonance signal because of the CP -even final states, X could be $f_2(1270)$, $f_0(1500)$, $f'_2(1525)$, $f_0(980)$, $f_0(1710)$ and $f_2(2010)$. For $b \rightarrow c$ transition as resonance background because of CP -odd final states, X could be D^0 , J/ψ , $\psi(2S)$, χ_{c0} , χ_{c1} , and χ_{c2} .

The number of these background in signal reconstruction could be further reduced by implementing veto on invariant mass of $2K_S^0$. However, such veto should be carefully validated with data. The distribution of invariant mass of X should agree well in MC and data, which is hard to check in the low luminosity. The distribution of $2K_S^0$ invariant mass in generic MC and data are shown in the Appendix

Some of these resonance have not been implemented inside generic MC production in the current Belle II simulation. Given the very limited statistics of data accumulation we used in this analysis, we only present the expected number of these resonances in 400fb^{-1} luminosity (about 2.14×10^8 events) from generic $\Upsilon(4S)$ events. These numbers should be re-checked in the future when data accumulation increases, and veto must be based on the structure of $2K_S^0$ invariant mass from data as well. Details about the expected yields can be found in Table 4.6. Currently there is no veto applied for rejecting these resonant background considering the estimated background number is about 1 event in the current luminosity.

4.1.5 $B\bar{B}$ background and self-cross feed

Another possible contribution of backgrounds are from $B\bar{B}$ events including the charged and the neutral particles. The estimated contributions of these types can be checked with charged $B\bar{B}$ samples and the mixed samples. For this channel, the number of the events is very limited. Self-cross feed backgrounds stands for the events from the signal-like events but the tag-side particle(s) is associated as a fake signal. The combined contributions from $B\bar{B}$ background and self-cross feed is about 3% in the channel and therefore we don't perform special treatment on them.

4.1.6 Signal Extraction

The event selections defined in Table 4.4 is applied to signal MC, generic MC and experiment data for signal extraction. As introduced in chapter 2, the integral luminosity in generic MC is 1 ab^{-1} and experiment data used in this analysis is about 62.8 fb^{-1} from the latest official processing.

The unbinned maximum likelihood fit using RooFit is performed to extract the signal. The 2D fit using both M_{bc} and ΔE are done by taking the probability density function as shown in Equation 4.13.

$$\mathcal{P}(M_{bc}, \Delta E) = f_{sig} \times \mathcal{P}_{sig}^{M_{bc}} \times \mathcal{P}_{sig}^{\Delta E} + (1 - f_{sig}) \mathcal{P}_{bkg}^{M_{bc}} \times \mathcal{P}_{bkg}^{\Delta E} \quad (4.13)$$

Table 4.6: Expected yield for signal and background resonances $2.14 \times 10^8 B\bar{B}$ in generic MC. The branching fraction of $B \rightarrow X K_S$ and $X \rightarrow 2K_S$ are listed for both PDG value and value in Belle II generic decay profile (see section 2.9). The events from CP -odd contamination is expected to be very low at current luminosity (62.8 fb^{-1}).

Resonances	$\text{Br}(B \rightarrow X K_S)\text{PDG}$	$\text{Br}(X \rightarrow 2K_S)$	$\text{Br}(B \rightarrow X K_S)\text{Dec.}$	$\text{Br}(X \rightarrow 2K_S)\text{Dec.}$	$B\bar{B}$ pairs	Expected yields
$D^0 K_S$	2.6×10^{-5}	1.7×10^{-4}	2.6×10^{-5}	1.8×10^{-4}	2.14×10^8	0.134
ηK_S	3.45×10^{-4}	$< 3.1 \times 10^{-4}$	4×10^{-4}	No Value	2.14×10^8	No Value
$J/\psi K_S$	4.35×10^{-4}	$< 1.4 \times 10^{-8}$	4.35×10^{-4}	0	2.14×10^8	0
$\psi(2S) K_S$	2.9×10^{-4}	$< 4.6 \times 10^{-6}$	2.9×10^{-4}	0	2.14×10^8	0
$\chi_{c0} K_S$	7.3×10^{-5}	3.16×10^{-3}	7.35×10^{-5}	3.1×10^{-3}	2.14×10^8	6.21
$\chi_{c1} K_S$	1.96×10^{-4}	6×10^{-5}	1.96×10^{-4}	1×10^{-5}	2.14×10^8	0.05
$\chi_{c2} K_S$	7.5×10^{-6}	2.6×10^{-4}	7.5×10^{-6}	5.5×10^{-4}	2.14×10^8	0.11
$f_2(1270) K_S$	1.35×10^{-6}	1.15×10^{-2}	1.35×10^{-6}	1.15×10^{-2}	2.14×10^8	0.42
$f'_2(1525) K_S$	1.5×10^{-7}	2.22×10^{-2}	No value	0.22	2.14×10^8	No Value
$f_2(2010) K_S$	5×10^{-7}	No Value	No Value	No Value	2.14×10^8	No Value
$f_0(980) K_S$	2.7×10^{-6}	No Value	2.75×10^{-6}	No Value	2.14×10^8	43.3
$f_0(1710) K_S$	5×10^{-7}	No Value	No Value	No Value	2.14×10^8	No Value
$f_0(1500) K_S$	6.5×10^{-5}	0.022	No Value	0.022	2.14×10^8	No Value
Total	-	-	-	-	-	$\simeq 50$

where $\mathcal{P}_{sig}^{M_{bc}}$ and $\mathcal{P}_{sig}^{\Delta E}$ are the single Gaussian and triple Gaussian functions. The f_{sig} is fraction of signal events based on M_{bc} and ΔE . The $\mathcal{P}_{bkg}^{M_{bc}}$ is primarily continuum events, and presented as Argus distribution as Equation 4.14 shows, with a preset mass threshold at $c = 5.29$ GeV.

$$f(x; \chi, c) = \frac{\chi^3}{\sqrt{2\pi}\Psi(\chi)} \cdot \frac{x}{c^2} \sqrt{1 - \frac{x^2}{c^2}} \cdot \exp\left\{-\frac{1}{2}\chi^2(1 - \frac{x^2}{c^2})\right\} \quad (4.14)$$

x is defined in $0 < x < c$. χ and c are parameters of the distribution, $\Psi(\chi) = \Phi(\chi) - \chi\phi(\chi) - \frac{1}{2}$ where $\Phi(\chi)$ and $\phi(\chi)$ cumulative distribution and probability density functions of the standard normal distribution, respectively.

The $\mathcal{P}_{bkg}^{\Delta E}$ is modeled by the first order Chebyshev polynomials. The shape parameters of signal events are determined by fitting to signal MC, and then fixed as constants in fitting of Equation 4.13 on M_{bc} and ΔE for generic MC and experiment data. Fitting results on signal MC are shown in Figure 4-10. The continuum back-

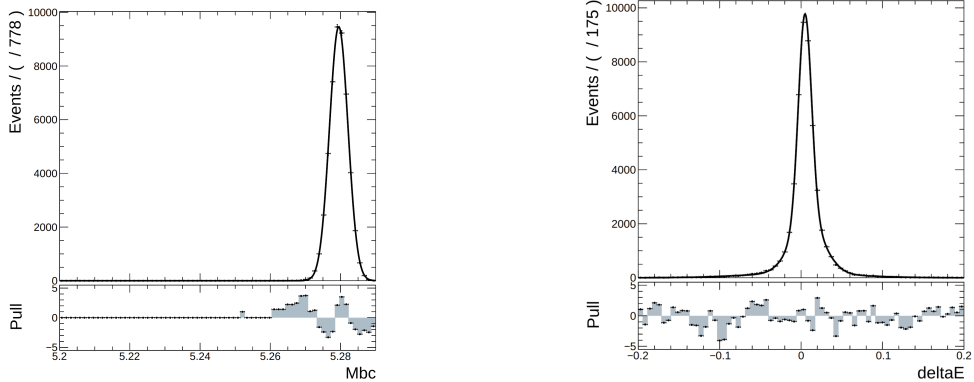


Figure 4-10: The distribution of M_{bc} and ΔE of signal MC of $B^0 \rightarrow K_S^0 K_S^0 K_S^0$ fitted with single and triple Gaussian functions respectively.

ground is fitted by using off-resonance generic MC to determine the shapes then fix them as constants for 2D fit as shown in Figure 4-11.

Then we set the events number for signal and background as floating parameters and use Equation 4.13 as 2D fit model on 1 ab^{-1} generic MC and experiment data, which is also done by using unbinned maximum likelihood fit. For B^0 in generic MC, the stacked histogram of each contribution and the 2D fit result projected on M_{bc} and ΔE is shown in Figure 4-12.

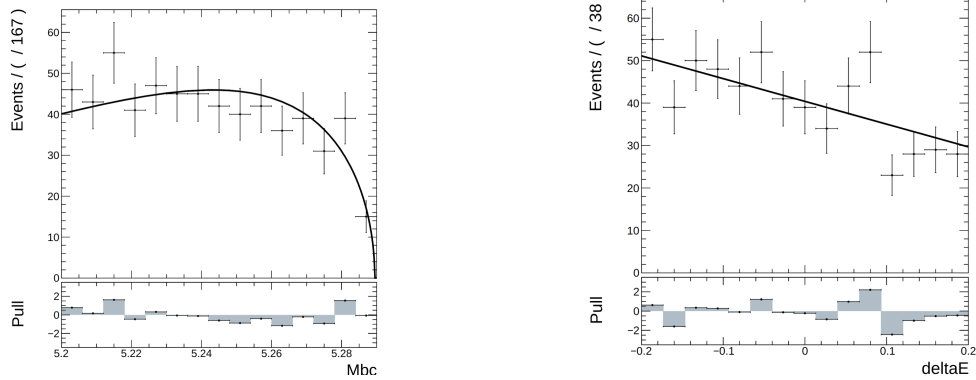


Figure 4-11: The distribution of M_{bc} and ΔE of continuum events in generic MC fitted with Argus and Chebyshev polynomial, respectively.

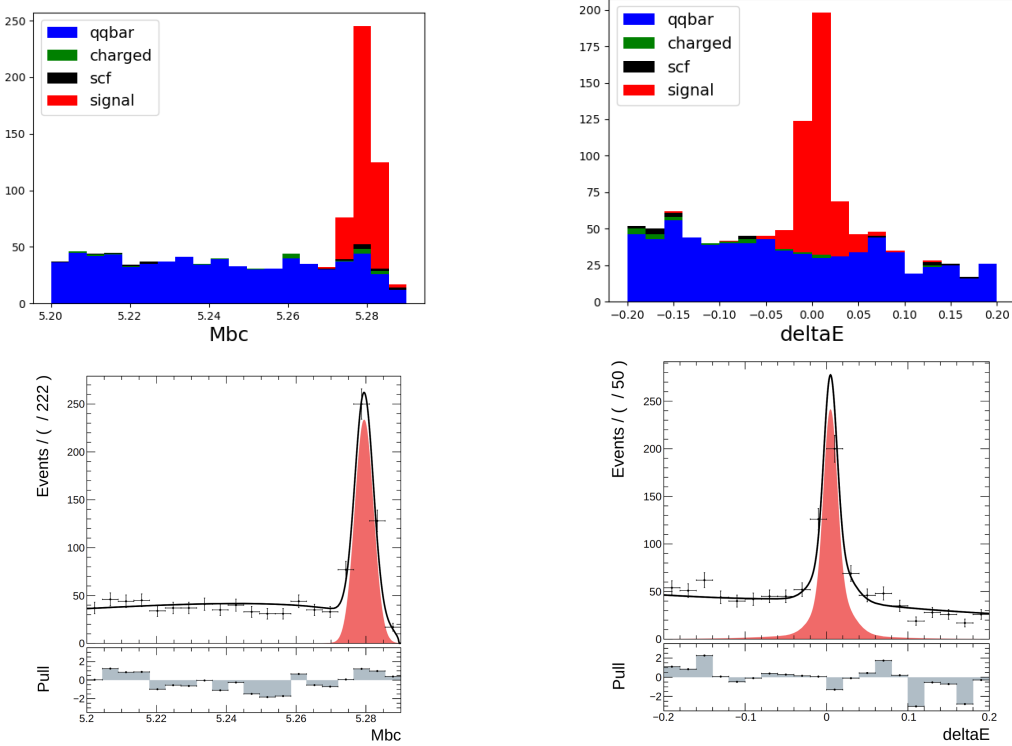


Figure 4-12: Top is the stacked plots for generic MC of M_{bc} and ΔE , where each background components are stacked with signal. The bottom is the 2D fit on 1 ab^{-1} generic MC projected on M_{bc} and ΔE , the red is signal component from the fit result in both plots.

Before perform fitting on experiment data, the distribution of K_S^0 invariant mass from the reconstructed B^0 candidates is compared between generic MC and experiment data. The distributions are shown in Figure 4-13, where the generic MC is scaled

to the luminosity of experiment data and an agreement within $\sim 1\sigma$ is observed on average.

The 2D fit of experiment data projected on M_{bc} and ΔE is in Figure 4-14.

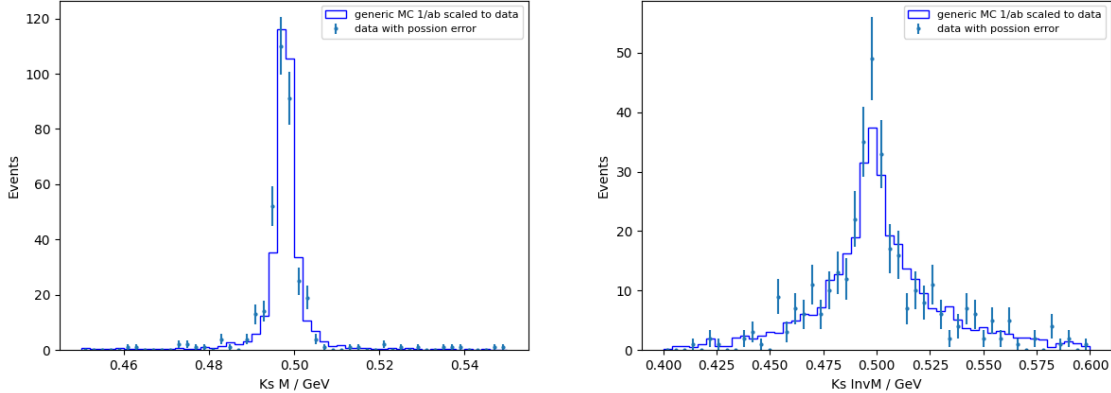


Figure 4-13: Invariant mass before(left) and after vertex fit(right) from generic MC and experiment data.

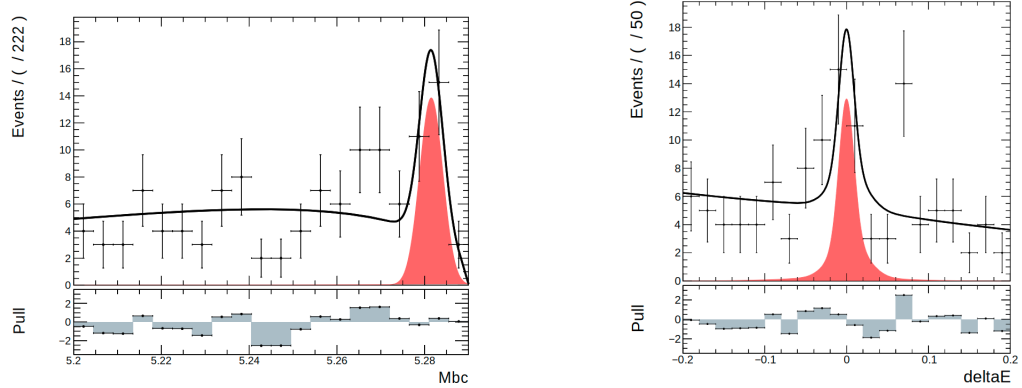


Figure 4-14: M_{bc} and ΔE 2D fit on 62.8 fb^{-1} data, the red is the signal component.

The number of signal events is extracted by the integral of fit model over the signal region which is defined as $5.27 < M_{bc} < 5.29 \text{ GeV}$ and $-0.1 < \Delta E < 0.1 \text{ GeV}$. The expected signal events with $\sim 35\%$ efficiency is calculated as Equation 4.15.

$$\mathcal{B}(B^0 \rightarrow K_S^0 K_S^0 K_S^0) = \frac{N_{sig}}{\mathcal{B}(K_S^0 \rightarrow \pi^+ \pi^-)^3 \times \epsilon_{rec} \times N_{B\bar{B}}} \quad (4.15)$$

In 1 ab^{-1} generic MC, the expected signal number is $7.7 \times 10^8 \times 6 \times 10^{-6} \times 21\% \times 35\% \simeq 339$. The 2D fit result from M_{bc} and ΔE yields 341 ± 20 events which agrees with

expected number within 1σ . The event number in sideband defined as $M_{bc} < 5.26$ GeV in generic MC is 507. Compared to Belle result with 772×10^6 ($\sim 1 \text{ ab}^{-1}$) $B\bar{B}$ pairs used, signal from data yields 327 ± 19 . In 62.8 fb^{-1} data fit in Belle II, we extract $N_{sig} = 17.4 \pm 4.2$ in signal region. The sideband region $M_{bc} < 5.26$ GeV contains 60 events in data.

To check linearity of the event number fitted from the M_{bc} and ΔE in this low statistics case, we extract the fraction of continuum backgrounds from generic MC sample rescaled to the experimental data luminosity, which includes about 46 continuum events. Then the number of signal events from 5 to 30 with 5 events per step are injected into the continuum events, to perform the M_{bc} and ΔE fit to check the output signal events number. The M_{bc} and ΔE distributions and fit in each injection test are shown in Figure 4-15. The fitted signal and background events depending on the injected numbers (linearity test) are presented in Figure 4-16, where the dependence on both signal and background events number are fitted with linear functions. The fit results show a good linearity on the input and output of signal numbers while the background numbers remain constant close to the input number.

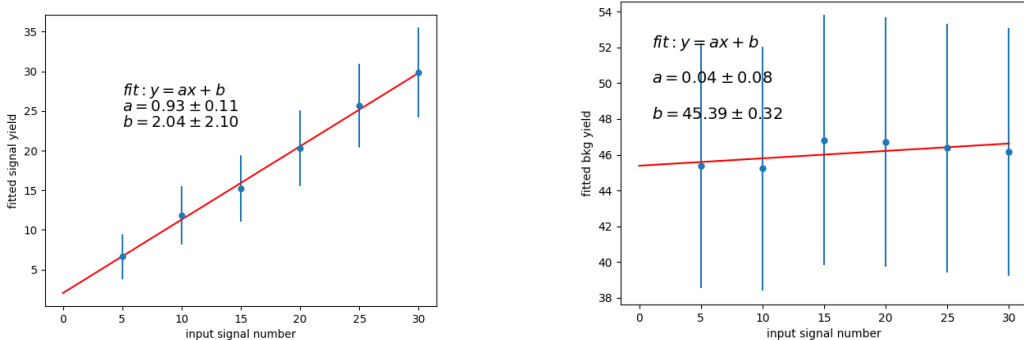
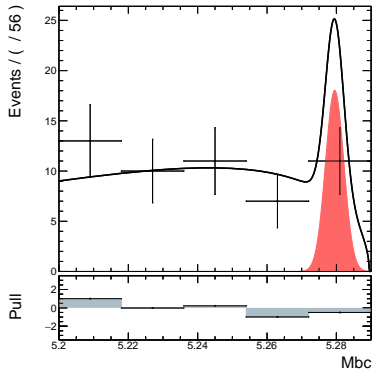


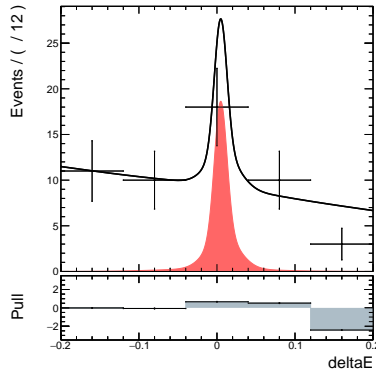
Figure 4-16: Injection test for signal extraction. The linearity is clear between input and output signal events number.

4.1.7 Kinematics and Vertexing Dependence on KsFinder

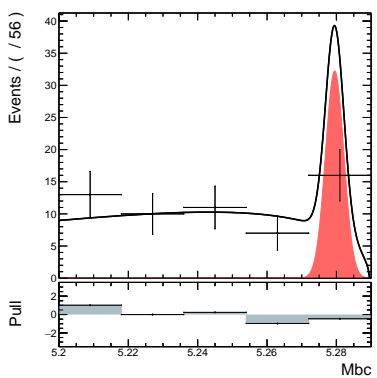
KsFinder largely reduce the combinatorial background of B^0 by improving K_S^0 purity. The previous section shows a good reconstruction performance at low statistics in



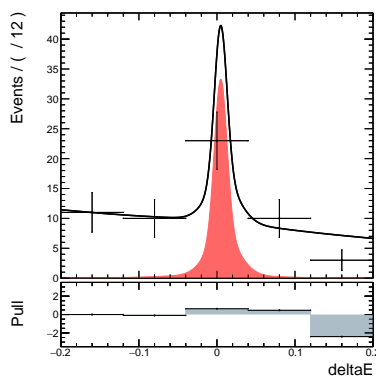
a) signal injected: 5



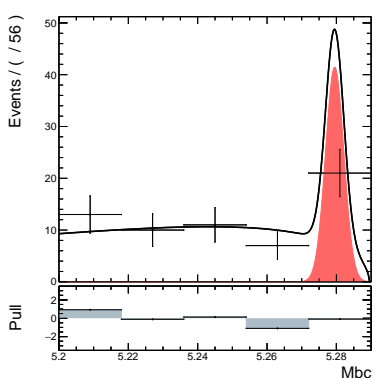
b) signal injected: 5



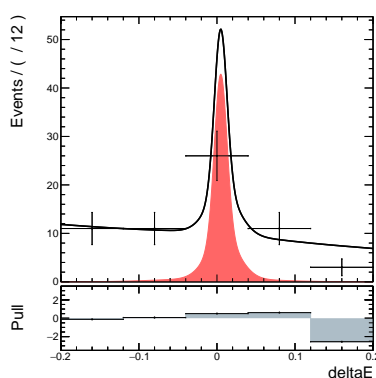
c) signal injected: 10



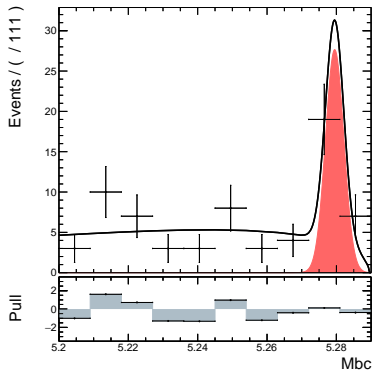
d) signal injected: 10



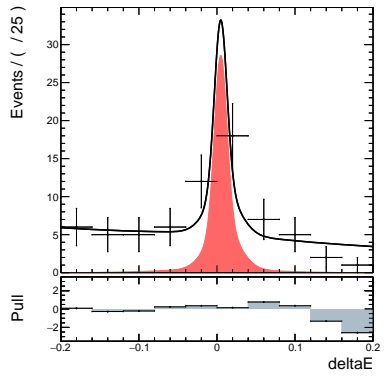
e) signal injected: 15



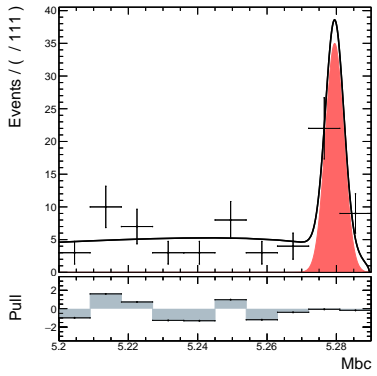
f) signal injected: 15



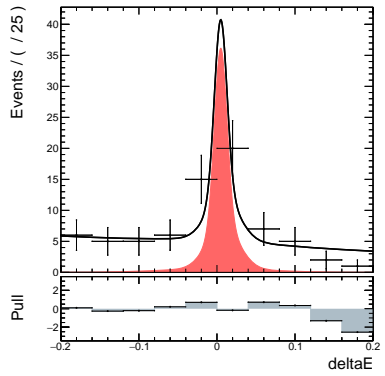
g) signal injected: 20



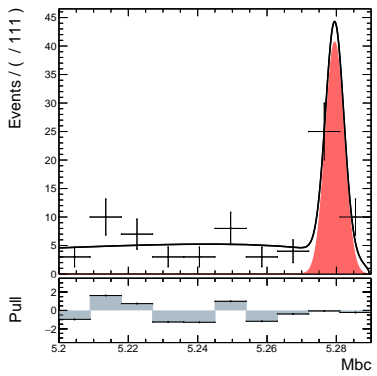
h) signal injected: 20



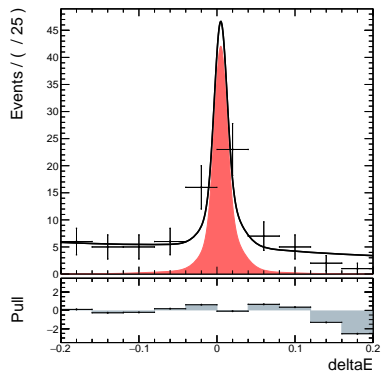
i) signal injected: 25



j) signal injected: 25



k) signal injected: 30



l) signal injected: 30

Figure 4-15: The fit results of M_{bc} and ΔE in signal injection test, where signal events from 5 to 30 with 5 per step are injected with 46 continuum events.

early phase 3 data. Without the power of rejection provided by K_S^0 finder, rediscovery of $B^0 \rightarrow K_S^0 K_S^0 K_S^0$ in early phase 3 of Belle II won't be feasible.

However, it's essential to check the potential impact on kinematics and vertex positions of B^0 regarding the implementation of KsFinder. The K_S^0 classification uses information such as invariant mass and decay vertex positions which may propagate bias into B^0 kinematics and vertex information, eventually may affect the measurement of CP parameters. Considering that 4 different types of K_S^0 based on their SVD hit numbers are used in B^0 reconstruction, the estimation with B^0 based on different K_S^0 types are required as well.

Given each type of B^0 based on how many CDC-only tracks (meaning B^0 daughter K_S^0 are *SVD00* type) it has in final states, the comparison on M_{bc} and ΔE with or without KsFinder is done by fitting the distribution in signal MC. M_{bc} and ΔE are both modeled by double Gaussian. The main Gaussian (with larger fraction) among the double Gaussian is used for checking the fit shape change by using KsFinder. Comparing corresponding fit results, no clear bias on M_{bc} and ΔE is found by using KsFinder where the main Gaussian fit results are agreed well. The fit results are shown in Figure 4-17 and 4-18.

Similar to the comparison of M_{bc} and ΔE , the Z direction vertex position and its uncertainties are also checked. No clear bias on vertex position and uncertainties are spotted either. The results are shown in Figure 4-19 and 4-20. It obvious that the resolution of vertex on z-axis is much worse when the final states of B^0 only have CDC tracks.

Above all, no strong appearance of bias on kinematics and vertex positions from using KsFinder has been found, KsFinder may implement a small shift on the vertex position which is neglect-able compared to the large statistical uncertainty due to low luminosity. For the moment, there's no correction on these observables are applied.

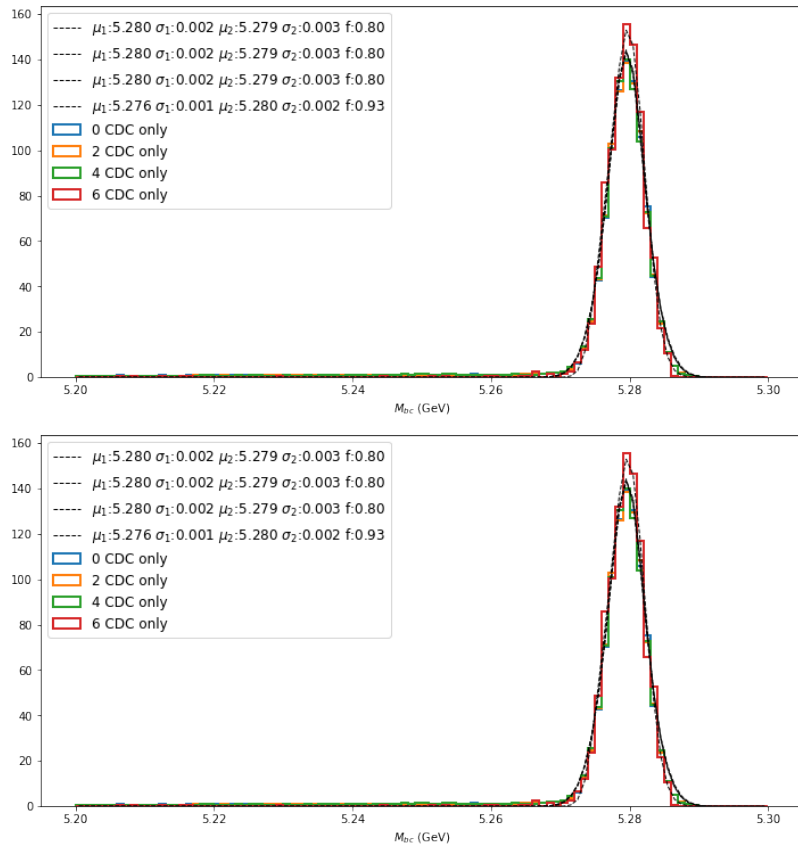


Figure 4-17: M_{bc} distribution based number of CDC-only tracks in final states. Top: no KsFinder; Bottom: K_S^0 finder used.

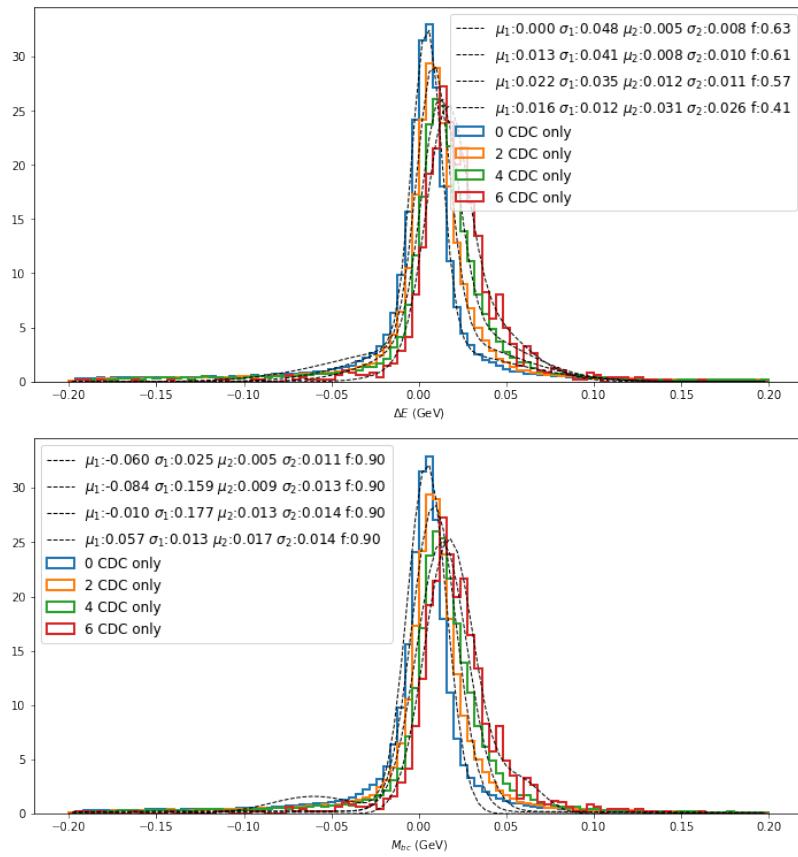


Figure 4-18: ΔE distribution based number of CDC-only tracks in final states. Top: no KsFinder; Bottom: KsFinder used.

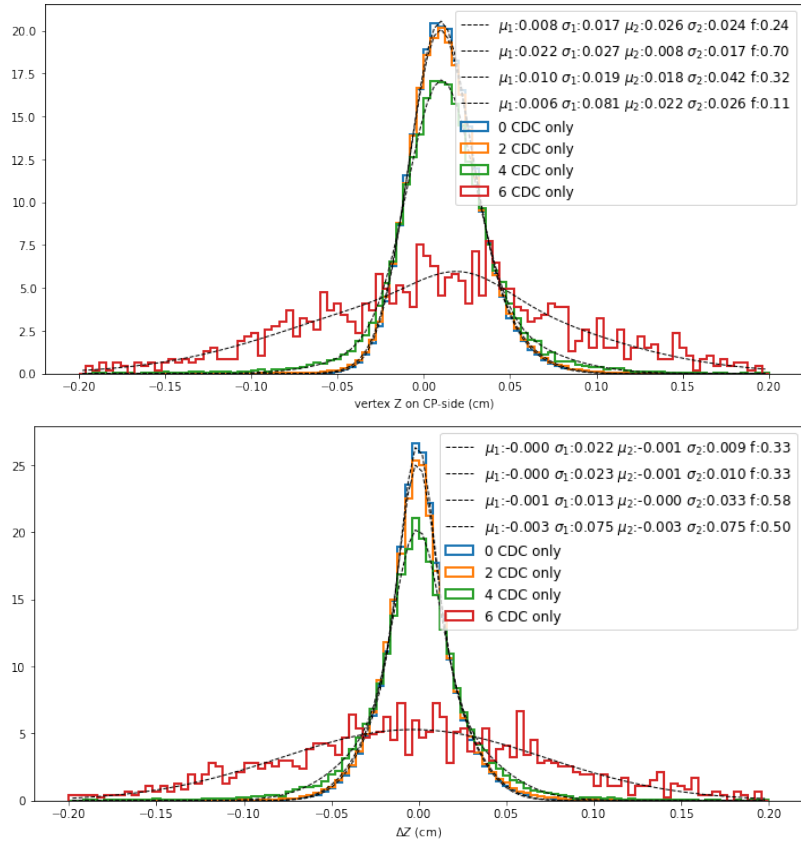


Figure 4-19: Δz distribution based number of CDC-only tracks in final states. Top: no KsFinder; Bottom: KsFinder used.

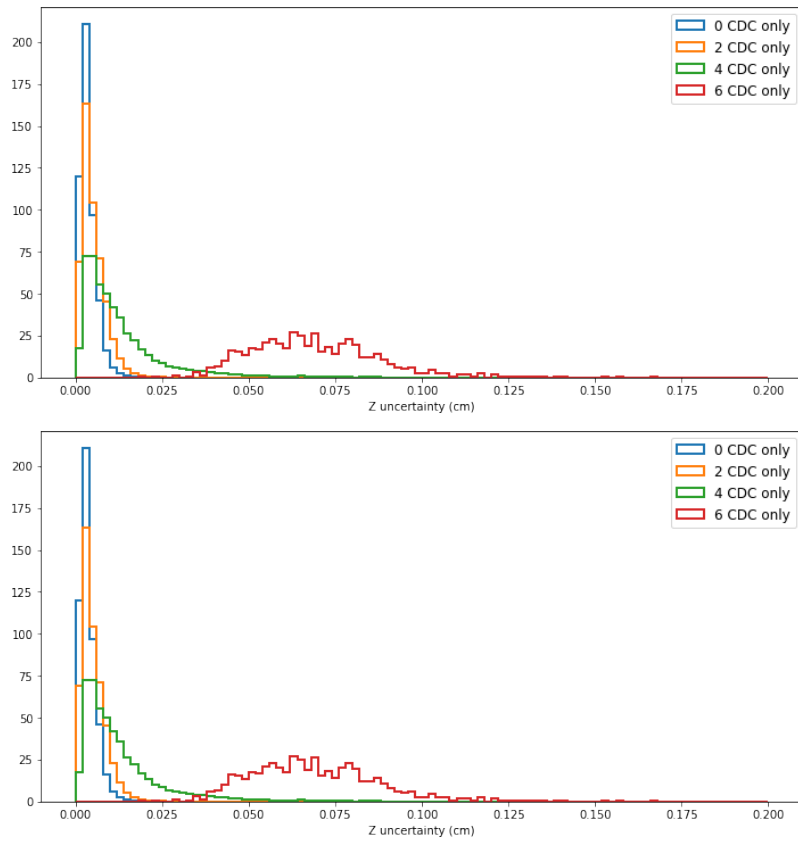


Figure 4-20: $\delta\Delta z$ distribution based number of CDC-only tracks in final states. Top: no KsFinder; Bottom: KsFinder used.

Chapter 5

CP parameters measurement

The measurement of CP parameters \mathcal{S} and \mathcal{A} are performed by fitting Equation 5.1 to the distribution of events with respect to the decay time difference Δt and flavor q , where $\Delta t = t_{CP} - t_{tag}$ and $q = +1(-1)$ when the tag-side B meson is $B^0(\bar{B}^0)$.

$$\mathcal{P}_{sig}(\Delta t, q) = \frac{e^{-|\Delta t|/\tau_{B^0}}}{4\tau_{B^0}} \left\{ 1 + q \cdot [\mathcal{S} \sin(\Delta M_d \Delta t) + \mathcal{A} \cos(\Delta M_d \Delta t)] \right\} \quad (5.1)$$

The Equation 5.1 describes the physics distribution of signal events only. To perform the unbinned maximum likelihood fit on data, a complete model for i -th event that includes the overlay of background components and outlier bands can be defined as Equation 5.2.

$$\begin{aligned} \mathcal{P}(\Delta t_i, q_i, f_i^{sig}, \mathcal{S}, \mathcal{A}) &= (1 - f_{ol}) \left[f_{sig} \mathcal{P}_{sig}(\Delta t_i, q_i, \mathcal{S}, \mathcal{A}) + (1 - f_{sig}) \mathcal{P}_{bkg}(\Delta t_i) \right] \\ &\quad + f_{ol} \mathcal{P}_{ol}(\Delta t_i) \end{aligned} \quad (5.2)$$

where f_{sig} and f_{ol} are the fraction of signal and outlier components, respectively. The \mathcal{P}_{bkg} and \mathcal{P}_{ol} are defined by Equation 5.3 and 5.4.

$$\mathcal{P}_{bkg}(\Delta t_i) = f_{bkg}^\delta \delta(\Delta t_i - \mu_{bkg}^\delta) + (1 - f_{bkg}^\delta) \frac{1}{2\tau_{bkg}} e^{-|\Delta t_i - \mu_{bkg}^{bkg}|/\tau_{bkg}} \quad (5.3)$$

$$\mathcal{P}_{ol}(\Delta t_i) = G(\Delta t_i, \sigma_{ol}) \quad (5.4)$$

where $\delta(\Delta t_i - \mu_{bkg}^\delta)$ is Dirac δ function and G is single Gaussian. The outlier component is to improve the fit quality with large Δt events.

5.1 Vertex Resolution Model

The Equation 5.2 presents an ideal distribution of Δt_i for each event without considering the difference between measured and the true position of the vertex. The difference can be described by introducing resolution functions. This turns Equation 5.2 into Equation 5.5.

$$\begin{aligned} \mathcal{P}(\Delta t_i, q_i, f_i^{sig}, \mathcal{S}, \mathcal{A}) = & (1 - f_{ol})[f_{sig} \mathcal{P}_{sig}(\Delta t_i) \otimes R_{sig}(\Delta t_i) \\ & + (1 - f_{sig}) \mathcal{P}_{bkg}(\Delta t_i) \otimes R_{bkg}(\Delta t_i)] \\ & + f_{ol} \mathcal{P}_{ol}(\Delta t_i) \otimes R_{ol}(\Delta t_i) \end{aligned} \quad (5.5)$$

The R_{sig} stands for the resolution function for signal events, which receives smearing effect from CP and tag side separately, namely R_{cp} and R_{tag} . The treatment of CP side and tag side is different because of vertexing strategies. For CP side, vertex of B^0 is reconstructed by fully fitting all the daughter particles. Instead, in tag side, there's no full reconstruction of B^0 so vertex fit is applied for the selected charged tracks in ROE. The background events have its own resolution model which is independent from CP violation parameters. The outlier is used to compensate and smooth the long tails when Δt becomes very large. In the early stage of Belle II, we don't include the outlier to have a more realistic model under very low statistics.

For signal events, the resolution functions are studied for CP -side and tag-side based on each possible degradation such as detector resolutions, effect of tracks from non-primary B vertex and so on. Such a method is used in Belle analysis and named as artificial model. Details are summarized in [38]. Considered the vertex position difference Δz for signal events as shown in Equation 5.6.

$$\Delta z = \Delta z' + (z_{cp} - z'_{cp}) - (z_{tag} - z'_{tag}) \quad (5.6)$$

where the primed ones stands for physics truth of the position and the non-primed is the measured value, the resolution function receives contribution from both *CP* and tag-side effects. In the meantime, the resolution functions on both sides also depend on the applied constraint. Considering that the fine structure of IP profile is not yet fully understood and small discrepancies have been observed between data and simulation[39], there's no IP constraint applied for both sides in vertex fit, which avoids potential bias from IP profile under this low statistical situation. The combined contributions can be presented as Equation 5.7.

$$R_{sig} = R_{cp} \otimes R_{tag} \quad (5.7)$$

5.1.1 *CP*-side resolution function

CP-side vertex is fitted with all tracks from a reconstructed B^0 , thus the resolution models only depend on detectors' effect. For each event, the resolution effect can be different based on event-by-event reconstruction quality, primarily presented by the reduced χ^2 called χ_2/N from *TreeFit*, which N is the degree of freedom of the fit. The distribution of χ_2/N in data are shown in Figure 5-1.

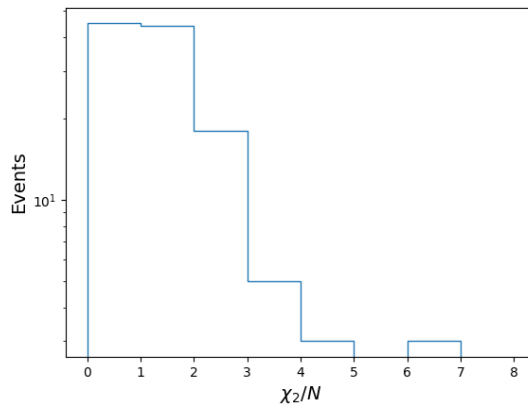


Figure 5-1: χ_2/N of selected events from data.

Therefore, we model the resolution functions on *CP*-side by using a double Gaussian function, where the mean is fixed to zero and the standard deviation is scaled by χ_2/N and the error of reconstructed vertex $\sigma_{z_{cp}}$, as shown in Equation 5.8.

$$R_{cp}(\delta z_{cp}) = (1 - f_{cp}^{tail})G(0, s_{cp}^{main}) + f_{cp}^{tail}G(0, s_{cp}^{tail}) \quad (5.8)$$

where s_{cp}^{main} and s_{cp}^{tail} are defined in Equation 5.9.

$$\begin{aligned} s_{cp}^{main} &= (s_0^{main} + s_1^{main} \cdot \chi_{cp}^2/N) \cdot \sigma_{z_{cp}} \\ s_{cp}^{tail} &= (s_0^{tail} + s_1^{tail} \cdot \chi_{cp}^2/N) \cdot \sigma_{z_{cp}} \end{aligned} \quad (5.9)$$

The dependence of resolution models on χ_2/N is shown in Figure 5-2. Restrictively speaking, the *CP*-side resolution for $B^0 \rightarrow K_S^0 K_S^0 K_S^0$ is slight different from $B^0 \rightarrow J/\psi K_S^0$, due to the absence of the direct charged tracks from the B^0 vertex. The modification of the resolution function on *CP*-side will be further studied when more data becomes available in future. Given the current low statistics, the Equation 5.8 works well as an approximation. By fitting the resolution function using signal MC on *CP*-side, we can determine the parameters which are listed in Table 5.1.

Table 5.1: Parameters in R_{cp} .

f_{cp}^{tail}	0.07424 ± 0.0008
s_0^{main}	0.9151 ± 0.0077
s_1^{main}	0.2142 ± 0.0064
s_0^{tail}	2.0477 ± 0.0779
s_1^{tail}	1.3470 ± 0.0720

5.1.2 Tag-side resolution function

For the tag-side, the vertexing is done by using *KFit* and no IP constraint used. Due to the charged tracks from non-primary B vertex, the resolution functions on tag-side not only receives contribution from detectors' effect R_{det}^{tag} but also the resolution degradation from secondary vertex, called R_{np}^{tag} . To the contrary, if all tracks that

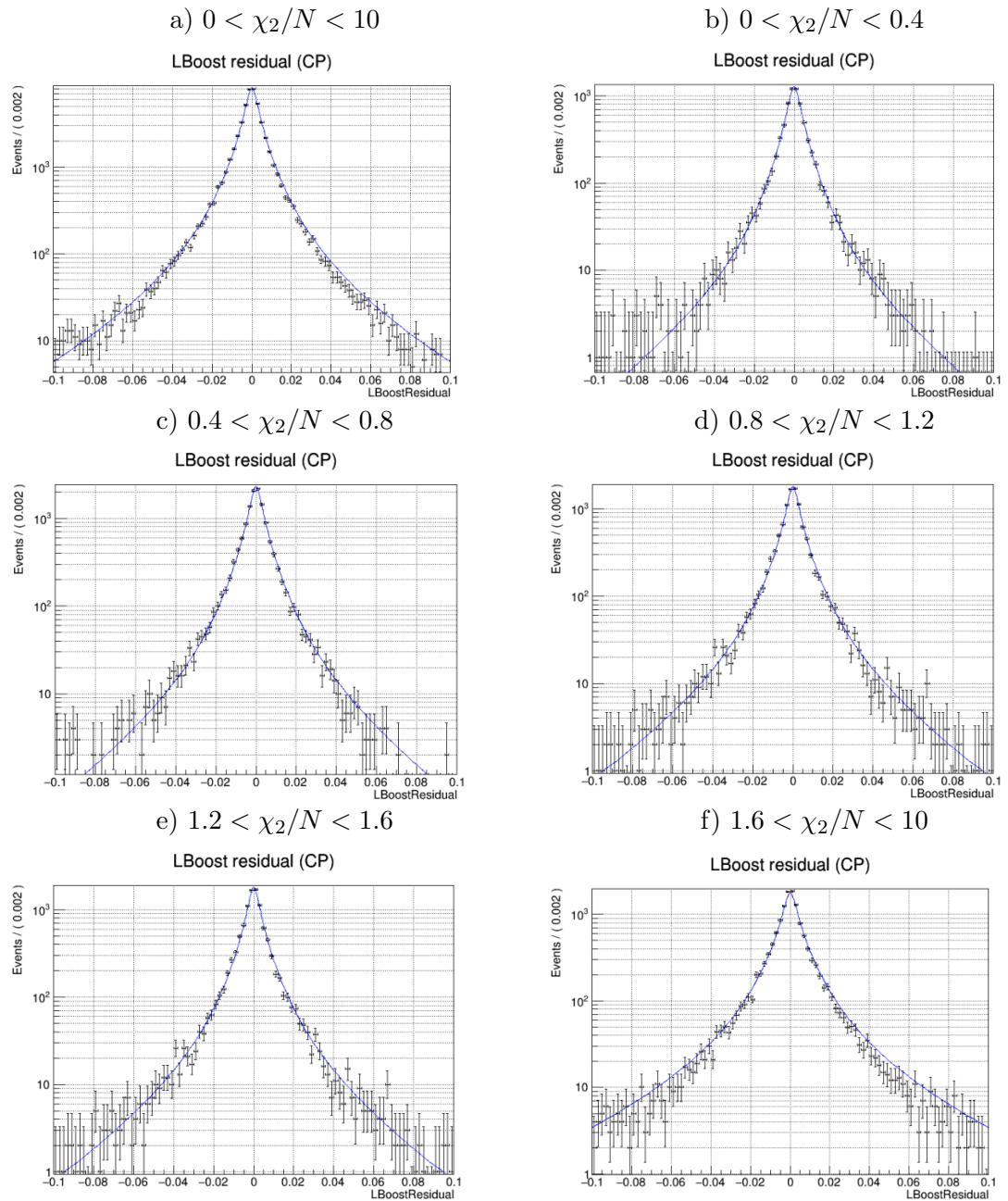


Figure 5-2: Resolution functions on *CP*-side, which shows dependence on the χ_2/N

are used for tag-side vertexing are primary tracks, the resolution will only be affected by the detectors' effect. The vertex position difference is defined as Equation 5.10. Therefore, the effects from both detectors and non-primary tracks contributes to the total resolution on tag-side as Equation 5.11 shows.

$$\begin{aligned} z_{tag} - z'_{tag} &= (z'_{tag} + \delta z_{tag}^{det} + \delta z_{tag}^{np}) - z'_{tag} \\ &= \delta z_{tag}^{det} + \delta z_{tag}^{np} \end{aligned} \quad (5.10)$$

$$R_{tag}(z_{tag} - z'_{tag}) = R_{det}^{tag}(\delta z_{tag}^{det}) \otimes R_{np}^{tag}(\delta z_{tag}^{np}) \quad (5.11)$$

Similarly to CP -side resolution function, detectors' effect is presented in Equation 5.12

$$R_{det}^{tag}(\delta z_{tag}^{det}) = (1 - f_{tag}^{tail})G(0, s_{tag}^{main} \cdot \sigma_{z_{tag}}) + f_{tag}^{tail}G(0, s_{tag}^{tail} \cdot \sigma_{z_{tag}}) \quad (5.12)$$

where main and tail Gaussian functions have the same central value at zero, but the standard deviation is scaled by χ_{tag}^2/N on the tag-side as shown in Equation 5.13.

$$s_{tag}^{main/tail} = s_0^{main/tail} + s_1^{main/tail} \cdot \chi_{tag}^2/N \quad (5.13)$$

Technically R_{det}^{tag} can be fitted with MC samples of which tag-side tracks are all from primary vertex. After obtaining the fitted parameters of R_{det}^{tag} , R^{tag} will only be dependent on R_{np}^{tag} . The fit model of R_{np}^{tag} is shown in Equation 5.14. It consists of three functions, including one Dirac δ function and two single-side exponential functions E_p and E_n . The $E_p(x, \tau_p) = (1/\tau_p)e^{-x/\tau_p}$ when $x > 0$ and the $E_n(x, \tau_n) = (1/\tau_n)e^{x/\tau_n}$ when $x < 0$. The exponential factors in both positive and negative components are scaled by the tag-side vertex uncertainty $\sigma_{z_{tag}}$.

$$R_{np}^{tag}(\delta z_{tag}^{np}) = f_\delta \delta(\delta z_{tag}^{np}) + (1 - f_\delta)[f_p E_p(\delta z_{tag}^{np}, \tau_p \cdot \sigma_{z_{tag}}) + (1 - f_p)E_n(\delta z_{tag}^{np}, \tau_n \cdot \sigma_{z_{tag}})] \quad (5.14)$$

Also, since tag-side has no dependence on how CP -side is reconstructed, the res-

olution functions on tag-side are almost mode-independent. We use the parameters that is obtained by fitting to the control sample data. The details about control sample study are here[39]. The fit plots for tag-side resolution functions are shown in Figure 5-3 and 5-4. The parameters obtained from the fit are listed in Table 5.2 and Table 5.3.

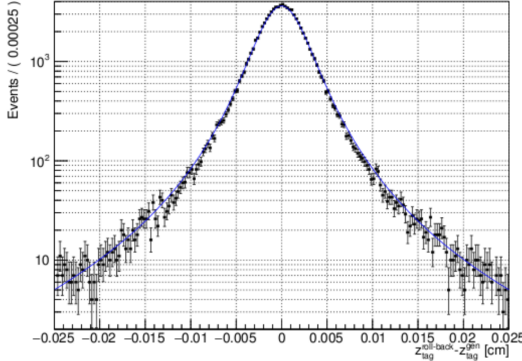


Figure 5-3: R_{det}^{tag} fit

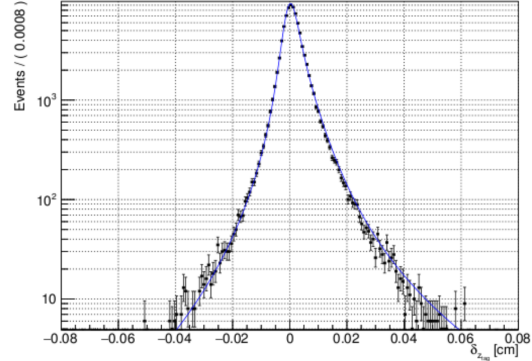


Figure 5-4: R_{np}^{tag} fit

Table 5.2: Parameters in R_{det}^{tag}

f_{tag}^{tail}	0.0523 ± 0.0025
s_0^{main}	1.1446 ± 0.0061
s_1^{main}	0.0443 ± 0.0022
s_0^{tail}	3.4480 ± 0.0897
s_1^{tail}	0.2666 ± 0.0276

Table 5.3: Parameters in R_{np}^{tag}

f_δ	0.6256 ± 0.0049
f_p	0.8316 ± 0.0051
τ_n	2.9141 ± 0.0758
τ_p	2.4846 ± 0.0269

The boost direction of each event is not constant event-by-event, so the position of vertex may not be optimized by calculating $\Delta t_i = \Delta z / \beta \gamma c$. This effect can be reduced by replacing vertex position difference on z-axis with the relative distance along the boosting direction, or introducing another resolution function called R_k [40]. The R_k has not been implemented in Belle II resolution model. Therefore, Δz projection on the boosted direction of each event is used for reducing this kinematics effect on resolution function.

5.1.3 Background events Δt distribution

The R_{bkg} is uncorrelated to vertex reconstruction method approximately. Because the background mainly comes from continuum events passing the selection, it's reasonable to model its resolution by a Gaussian-like function. A double-Gaussian with its standard deviation scaled by the measured uncertainties from both sides is used as Equation 5.15. To be noted, unlike resolution functions on CP or tag-side, the standard deviations of the double Gaussian are scaled by both the vertex position uncertainties $\sigma_{z_{cp}}$ and $\sigma_{z_{tag}}$.

$$R_{bkg} = (1 - f_{tail}^{bkg})G(\Delta t_i, \sigma_{main}^{bkg} \sqrt{\sigma_{z_{cp}}^2 + \sigma_{z_{tag}}^2}) + f_{tail}^{bkg}G(\Delta t_i, \sigma_{tail}^{bkg} \sqrt{\sigma_{z_{cp}}^2 + \sigma_{z_{tag}}^2}) \quad (5.15)$$

The background events Δt shapes $\mathcal{P}_{bkg} \otimes R_{bkg}$ can be determined by fitting to side-band data. There are totally seven floating parameters which are listed in Table 5.4 with fitted values using 60 sideband events at $M_{bc} < 5.26$ GeV, shown in Figure 5-5

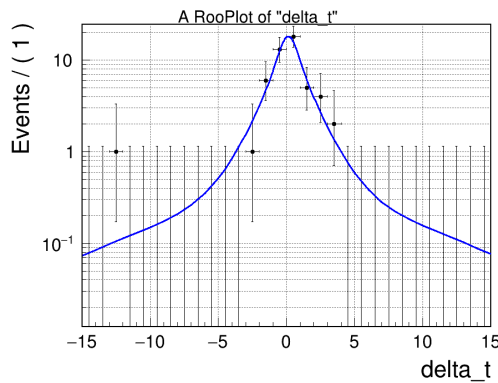


Figure 5-5: $\mathcal{P}_{bkg} \otimes R_{bkg}$ fit using 60 sideband events at $M_{bc} < 5.26$ GeV.

μ_{δ}^{bkg}	0.1310 ± 0.1902
μ_l^{bkg}	0.1638 ± 0.5030
τ_{bkg}	1.0541 ± 0.4370
f_{δ}^{bkg}	0.5861 ± 0.2570
f_{tail}^{bkg}	0.0417 ± 0.0408
σ_{main}^{bkg}	1.4348 ± 0.3940
σ_{tail}^{bkg}	28.0930 ± 8.8221

Table 5.4: Parameters in Background Δt distribution.

5.2 Flavor Tagging

In order to determine the flavor of tag side B^0 , flavor tagging algorithm is being developed. The flavor tagging uses information from μ^\pm, π^\pm, K^\pm and Λ which are categorized into 13 different types as illustrated in Figure 5-6.

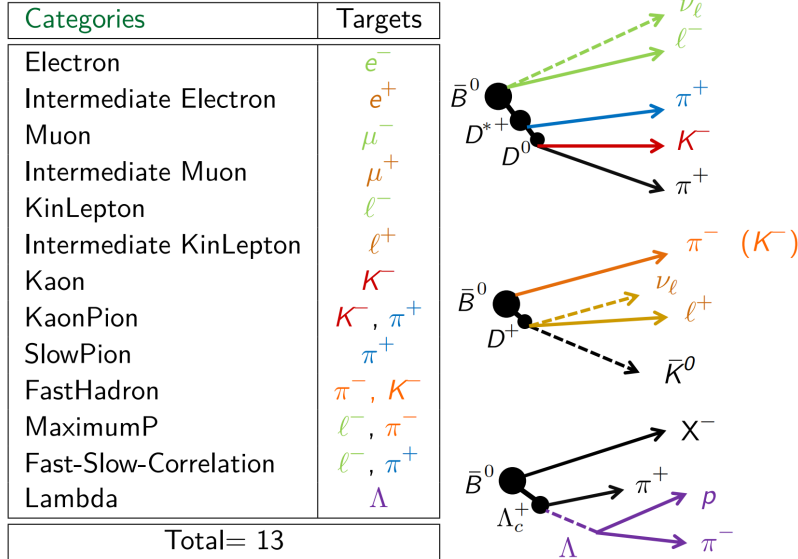


Figure 5-6: Particles and their categories used in flavor tagging algorithm[41].

For each particle that has been used from above categories, PID and kinematics information are extracted and feed to the combiner as training variables, to obtained a classifier response corresponding to each category. Then for all responses from

these categories, a total classifier is trained to present the likelihood of flavor q . This algorithm is called category-based method which is used in this thesis. To be specific, after the reconstruction on the CP -side B^0 is done, the rest-of-events tracks that are used to form the particle lists 5-6 are selected. The FastBDT as the back-end algorithm is chosen for performing training on the classifier of flavor tagging. Targeted variable is true q of tag-side neutral B in MC. To minimize impact of the reconstruction performance on CP -side, MC sample of $B^0 \rightarrow \nu\nu$ is used as the training sample where the final states are completely invisible.

Considering the limited power of flavor tagging accuracy, there is a certain fraction of events that are wrongly tagged, among all events that can be flavor tagged based on the final states. Thus, the flavor tagging efficiency ϵ and wrong tag fraction w are defined, respectively. Taking into account of the performance of flavor tagging, the observed distribution of Equation 5.2 becomes Equation 5.16.

$$\mathcal{P}_{sig}^{obs}(\Delta t, q, \epsilon, w) = \frac{e^{-|\Delta t|/\tau_{B^0}}}{4\tau_{B^0}} \epsilon \left\{ 1 - q \cdot \Delta w + q(1 - 2w) \cdot [\mathcal{S} \sin(\Delta M_d \Delta t) + \mathcal{A} \cos(\Delta M_d \Delta t)] \right\} \quad (5.16)$$

Compared to the original, the term with \mathcal{S} and \mathcal{A} is reduced by factor $r \equiv |1 - 2w|$, defined as the dilution factor.

The statistical uncertainty of \mathcal{S} now receives contribution from ϵ and w : $\delta(\mathcal{S}) \propto \frac{1}{\epsilon(1-2w)N_{rec}}$, which means it's quite important to correctly measure ϵ and w . The uncertainty of w is much larger than ϵ which makes w an important source of systematic uncertainty. The validation of flavor tagger using flavor specific control sample is summarized here: [41]. The w for each single event is defined as a probability which can be presented by the average wrong tag fraction within a close range. The binned values of dilution factor r is defined for the calculation of w as $[0, 0.1, 0.25, 0.5, 0.625, 0.75, 0.875, 1]$, which is called r -bin. For all events that have been successful tagged, they are projected into histogram of r -bin, and w is calculated in each bin by the fraction of events with $q \cdot r$ opposite to its MC flavor. The distribution of $q \cdot r$ is shown in Figure 5-7 using signal MC of $B^0 \rightarrow K_S^0 K_S^0 K_S^0$.

Besides, w can be different between B^0 and \bar{B}^0 , where $\bar{w} = (w_{B^0} + w_{\bar{B}^0})/2$ and

$\Delta w = w_{B^0} - w_{\bar{B}^0}$. Due to the small value of Δw , the contribution from Δw can be safely treated as zero in Equation 5.16. Similarly, for ϵ , the values calculated based on each r -bin are used in Equation 5.16 as well. The difference $\mu = \epsilon_{B^0} - \epsilon_{\bar{B}^0}$ is about 1% to 2% in each r -bin, thus treated as zero, too. The distributions of w , Δw , ϵ , and μ in each r -bin are shown in Figure 5-8.

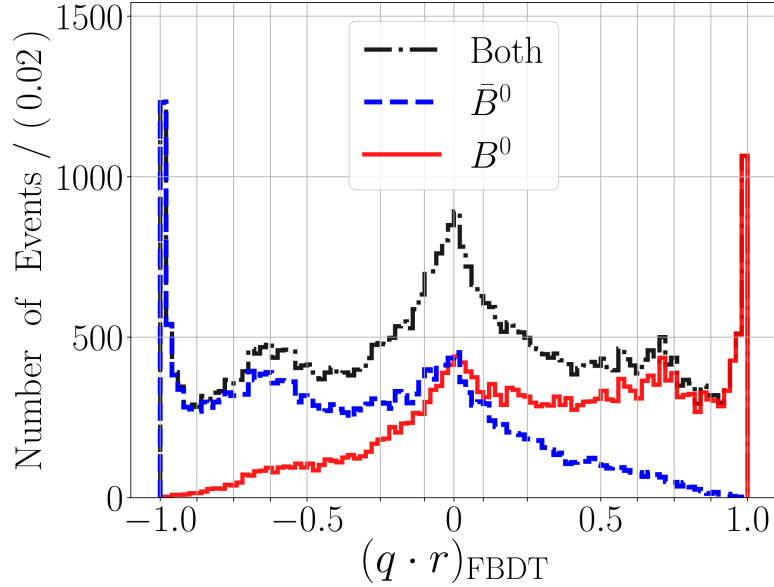


Figure 5-7: The distribution of flavor tagger output ($q \cdot r$) for both tag-side of B^0 and \bar{B}^0

5.3 CP Fitter

The parameters that are needed for measuring \mathcal{S} and \mathcal{A} are studied and obtainable. Using observed Δt distribution from selected events, Equation 5.5 can be fitted using unbinned maximum likelihood fit. The fit takes Δt , signal fraction f_{sig} , the flavor charge q as observables, and in the meantime the vertexing error $\sigma_{z_{cp}}$, $\sigma_{z_{tag}}$ and χ_2/N are used as event-by-event conditional variables. For Belle II, a new CP fitter is developed based on Python (version 3.7) and RooFit, which is naturally easy to use and maintained with BASF2. The fitter requires a configuration files which contains all the parameters' definitions including their ranges, initial values, floating states and uncertainties.

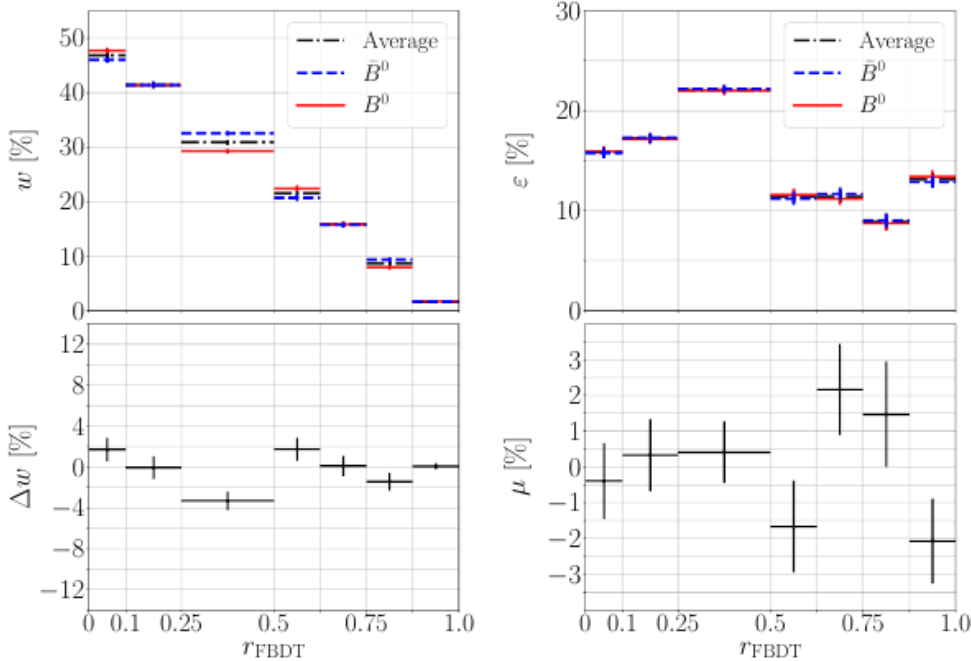


Figure 5-8: The flavor tagging efficiency, wrong tagging fraction, and their difference between different flavors in each of the r -bin.

5.4 Blind analysis and fit

As a required procedure to make sure the CP parameters are measured without bias due to the preconceived results, a blind analysis procedure is conducted before the fit is actually performed using the experimental data. The blind fit procedure includes the CP fit on signal MC and generic MC, with different number of events used. To check the reliability of fit result from CP fitter, a linearity test and toy MC study is also performed.

5.4.1 CP fit on MC samples

Using CP fitter, we first perform the CP fit on events in signal MC and generic MC. The signal and generic MC are generated with phase-space model which contains zero CP violation ($\mathcal{S} = \mathcal{A} = 0$). The events that pass the selections in Table 5.5 are used for CP parameters fit.

We have 10000 (8873 passing selections) events from signal sample and 415 (373

Observables	Selections
Δt	$-70 < \Delta t < 70$ ps
CP -side χ_2/N	$0 < (\chi_2/N)_{cp} < 8$
tag-side χ_2/N	$0 < (\chi_2/N)_{tag} < 50$
$\sigma_{z_{tag}}$	$\sigma_{z_{tag}} < 0.1$ cm
signal region	$5.27 < M_{bc} < 5.29$ GeV and $ \Delta E < 0.1$ GeV

Table 5.5: The selection criteria for events that are used for CP parameters fit.

MC sample (events)	\mathcal{S}	\mathcal{A}
signal MC (8873)	$\sin(2\phi_1) = 0.00 \pm 0.04$	$\mathcal{A} = -0.01 \pm 0.02$
generic MC (373)	$\sin(2\phi_1) = 0.00 \pm 0.21$	$\mathcal{A} = -0.05 \pm 0.07$
generic MC (30)	$\sin(2\phi_1) = 0.20 \pm 0.85$	$\mathcal{A} = -0.06 \pm 0.30$

passing selections) events from 1 ab^{-1} generic MC to fit CP parameters. To mimic the events number expected in data sample, 30 events randomly taken from generic MC are used to perform the fit as well. The fit results are shown in Figure 5-9, 5-10 and 5-11. The fit results of \mathcal{S} and \mathcal{A} are summarized in Table ??

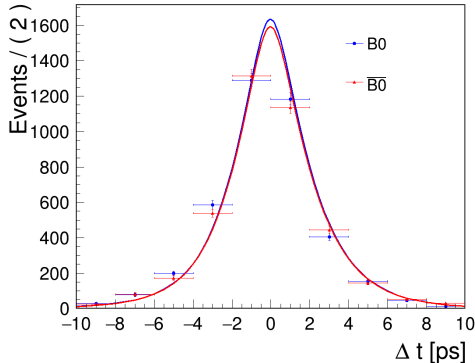


Figure 5-9: CP fit on 8873 signal MC.

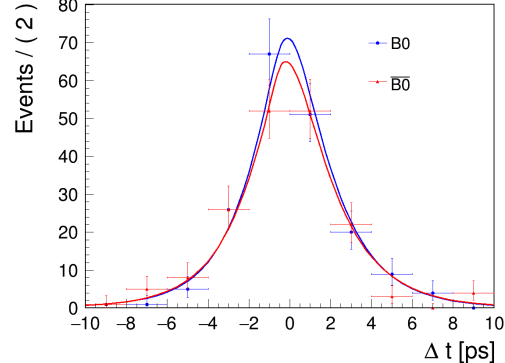


Figure 5-10: CP fit on 373 generic MC.

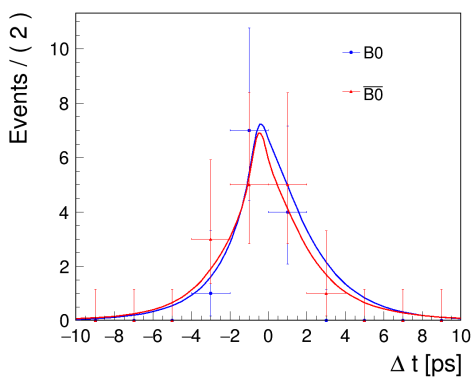


Figure 5-11: CP fit on 30 generic MC.

The fit results are consistent with expectation in non- CP violation from MC input, and the statistical uncertainties has the tendency $\delta \propto 1/\sqrt{N}$ as poission distribution, where N is events number used for CP fit. To test fit on non-zero CP violating MC, the fit on $B^0 \rightarrow J/\psi K_S^0$ signal MC is also done, the details of events selection as well as fit model determination can be found[39]. The fit result over 10000 events is shown in Figure 5-12, which results in $\sin(2\phi_1) = 0.70 \pm 0.05$ and $\mathcal{A} = -0.01 \pm 0.02$. The results agree with the input.

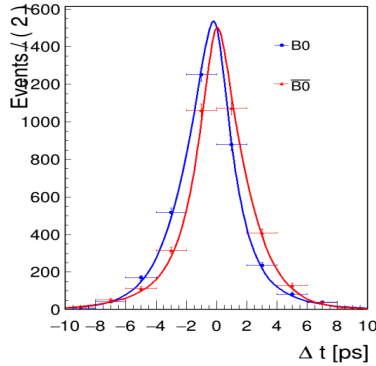


Figure 5-12: CP fit over 10000 $B^0 \rightarrow J/\psi K_S^0$ signal MC.

5.4.2 Linearity Test

To validate the CP fit linearity, a series of toy MC samples is generated, which the χ_2 from vertex fit, events number N and vertex errors on CP and tag-side are sampled from the distribution of signal MC. The resolution functions parameters are kept as same as CP fit on generic MC. The input \mathcal{A} is set to zero while the input value of $\sin(2\phi_1)$ is running from 0.1 to 0.9. Each dataset contains 10000 events. The dependence between input and output are shown in Figure 5-13. The linearity fit shows a good agreement between input and output.

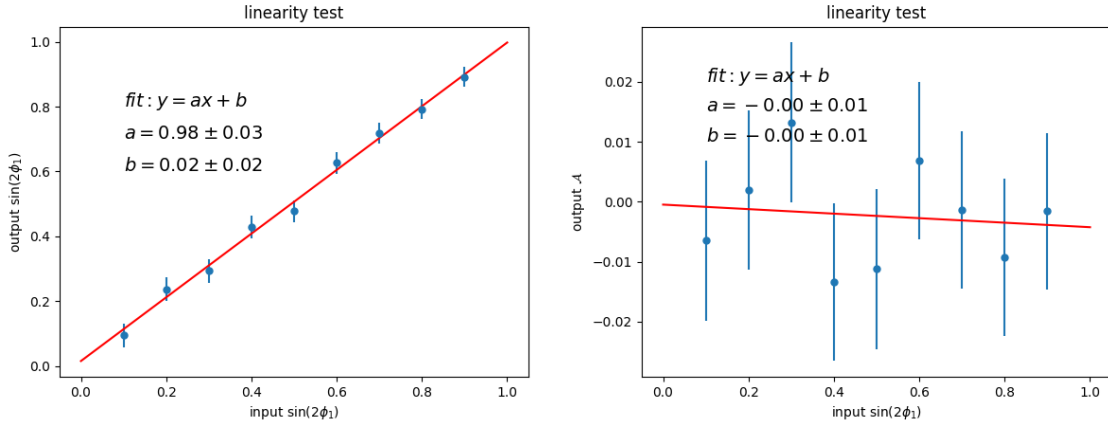


Figure 5-13: Linearity test of CP fit.

Also, we fix $\sin(2\phi_1)$ at zero while floating A from 0.1 to 0.9, the dependence between input and output are as Figure 5-14 shows. The linearity fit shows a good agreement as well.

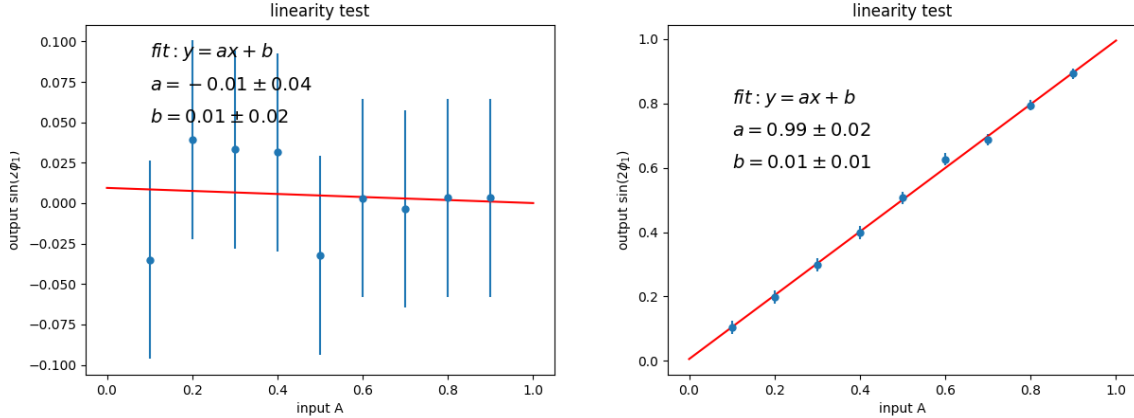


Figure 5-14: Linearity test of CP fit.

5.4.3 Toy MC Fit Pull

In order to check the fit bias with input-output method, a series of 1000 dataset of toy MC has been created containing about 26 events in each. The event number is set based on the expected number from signal region in data after the selection. The χ^2 from vertex fit, events number N and vertex errors on CP and tag-side are sampled from the distribution of data. The fit to dataset is performed with zero input $\sin(2\phi_1)$

and \mathcal{A} as floating parameters. We expect to use the normal distribution to fit the pull of $\sin(2\phi_1)$ and \mathcal{A} .

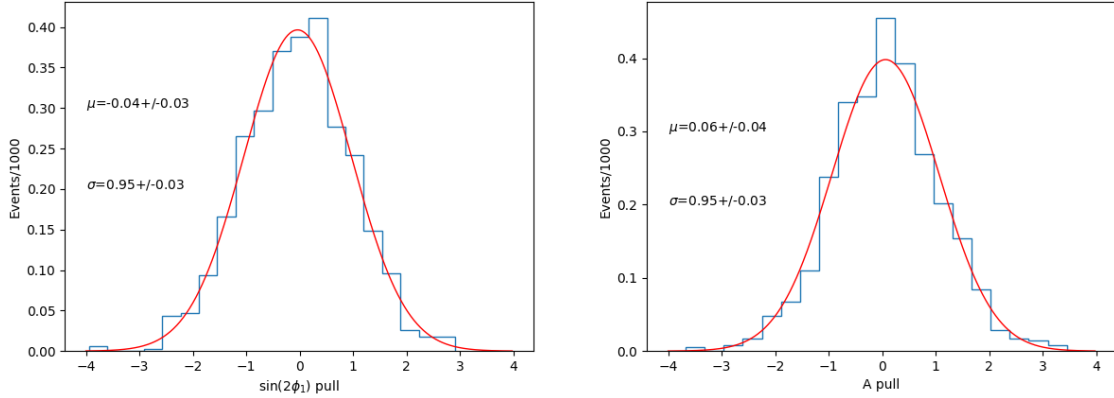


Figure 5-15: Pull of $\sin(2\phi_1)$ and \mathcal{A} fitted with the standard normal distribution.

The fit results shows a good recovery of input $\sin(2\phi_1)$ and \mathcal{A} with no clear bias is spotted.

5.4.4 Lifetime and Δm_d Fit

Before looking at CP parameters in data, we need to check if the physics parameters are consistent when setting the CP fitter to fit them in float. To test lifetime fit, first we use 10000 signal MC events which is generated by $\tau_{B^0} = 1.520$ from PDG value. The $\sin(2\phi_1)$ and \mathcal{A} are fixed at zero during the fit, for which the generator level CP violation is zero. This is equivalent fit to Equation 5.17.

$$\mathcal{P}(\Delta t, \tau_{B^0}) = \frac{e^{-|\Delta t|/\tau_{B^0}}}{4\tau_{B^0}} \quad (5.17)$$

The fit result on signal MC is 1.537 ± 0.024 ps which is consistent with the input. We perform the lifetime fit on data in signal region, and the CP parameters are fixed based on PDG values to: $\sin(2\phi_1) = 0.69$ and $\mathcal{A} = 0$. The fitted lifetime from $B^0 \rightarrow K_S^0 K_S^0 K_S^0$ is 1.431 ± 0.382 ps. The result is consistent with PDG value. The distribution of Δt in lifetime fit is shown as Figure 5-16. The B^0 and B^+ lifetime fit

using control sample is also performed and summarized in here[39]. The results are consistent with PDG values as input in MC generator.

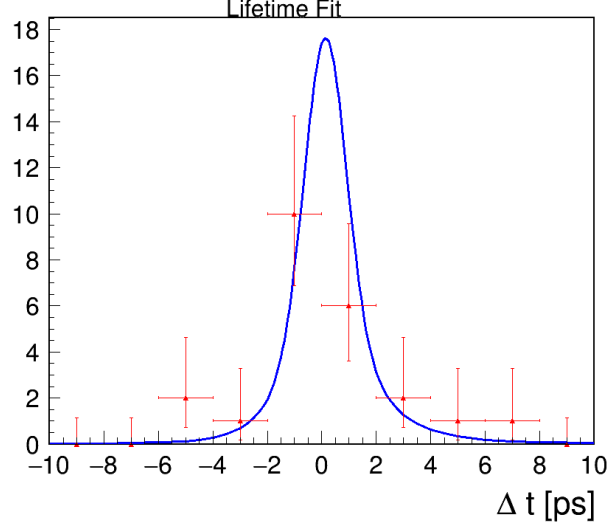


Figure 5-16: Lifetime fit on data

To test the fit on physics parameter Δm_d , we generate 200 toy MC sets of $B^0 \rightarrow K_S^0 K_S^0 K_S^0$ with input $\Delta m_d = 0.507 \text{ GeV}/c^2$ where each set contains 26 events as same as data. The fit result is close to normal distribution and the pull of Δm_d is shown in Figure 5-17.

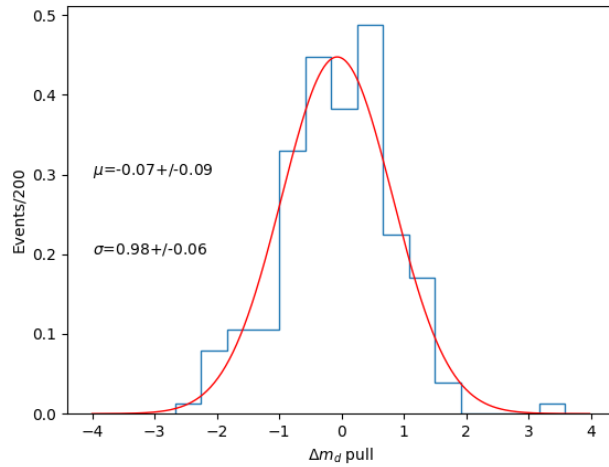


Figure 5-17: Pull of Δm_d

5.5 CP fit on data

After the CP fit procedures are reviewed by Belle II collaboration, the permission of measuring CP parameters using 62.8 fb^{-1} Belle II data is granted. The events number used for the CP fit is 26, and the fit result is shown Figure 5-18.

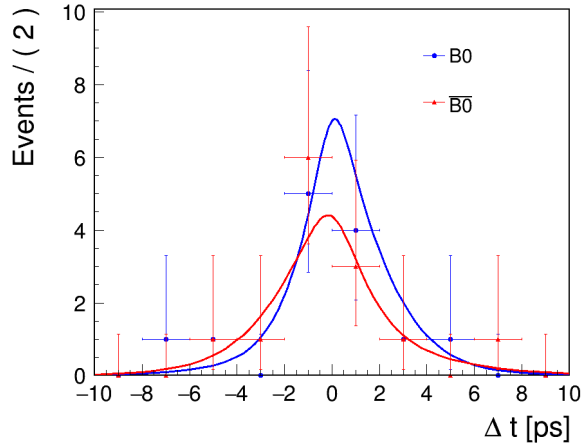


Figure 5-18: The CP fit from data.

The results of CP parameters are:

$$\begin{aligned} \sin(2\phi_1) &= 0.82 \pm 0.85(\text{stat}) \\ \mathcal{A} &= -0.21 \pm 0.28(\text{stat}) \end{aligned} \tag{5.18}$$

5.6 Systematic Uncertainty

The systematic uncertainty that affects the fit results may come from many aspects of the measurement setup. The contributions that matter at the current stage of Belle II are summarized as Table 5.6.

For the listed sources of systematic uncertainty, if the parameters are defined with MC study, we float the value by $\pm 2\sigma$ of their uncertainty, and if the parameters are defined by data, we float the value by $\pm 1\sigma$, to have a more robust estimation of impact on fit results. The impact of CP parameters are separately estimated from each sources with positive and negative differentials. With sum of the quadrature of

Sources	$\delta\mathcal{S}$	$\delta\mathcal{A}$
signal fraction	0.04	0.04
background Δt shapes (data)	0.04	0.04
signal Δt resolution (MC)	0.03	0.01
fit bias	0.01	0.01
flavor tagging	0.004	0.004
physics parameters	0.007	0.001
KsFinder impact on data	0.004	0.001
vertex reconstruction	0.019	0.021
Total	0.07	0.06

Table 5.6: The contributions of each source of systematic uncertainty.

each term, the overall systematic uncertainty is obtained.

The signal resolution functions' parameters are determined from MC study for signal component. The impact on fit results is summarized as follows Table 5.7.

Table 5.7: systematic uncertainty from signal Δt shapes

source	$+\delta\mathcal{S}$	$+\delta\mathcal{A}$	$-\delta\mathcal{S}$	$-\delta\mathcal{A}$
f_{cp}^{tail}	-0.000096	-0.000057	0.000014	0.000056
s_0^{main}	0.005443	0.001299	-0.005675	-0.001404
s_1^{main}	0.019934	-0.000903	-0.020204	0.000633
s_0^{tail}	-0.003233	-0.001623	0.00327	0.001596
f_{tag}^{tail}	0.00314	-0.001257	-0.003117	0.001266
s_0^{main}	0.002011	-0.001395	-0.001956	0.001398
s_1^{main}	0.005059	-0.00084	-0.004969	0.000825
s_0^{tail}	-0.000135	-0.000393	0.00010	0.000435
s_1^{tail}	0.000101	0.000027	-0.000472	0.000129
f_δ	-0.007248	-0.000552	0.007231	0.000591
f_p	0.003037	0.004347	-0.003069	-0.004314
τ_n	-0.00101	-0.002841	0.000937	0.00294
τ_p	0.004497	0.002502	-0.004648	-0.002478

The background Δt shapes' parameters are determined from data sideband $M_{bc} < 5.26$ GeV. The impact on fit results is summarized as follows:

Table 5.8: systematic uncertainty from background Δt shapes

source	$+\delta\mathcal{S}$	$+\delta\mathcal{A}$	$-\delta\mathcal{S}$	$-\delta\mathcal{A}$
μ_δ^{bkg}	-0.014294	-0.016581	0.006758	0.006537
μ_l^{bkg}	-0.002798	-0.012567	0.003789	0.012783
τ_{bkg}	0.001377	0.001689	-0.004159	0.000085
f_δ^{bkg}	-0.011315	0.001365	0.011187	-0.001395
f_{tail}^{bkg}	-0.002661	0.00153	0.00248	-0.001368
σ_{main}^{bkg}	0.0207015	0.022041	-0.0236175	-0.01569
σ_{tail}^{bkg}	-0.000275	-0.000159	0.000179	0.000141

The flavor tagging parameters wrong tagging fraction w in each rbin is determined from signal MC. The impact in each rbin on fit results is summarized as follows:

Table 5.9: systematic uncertainty from wrong tagging fraction

source	$+\delta\mathcal{S}$	$+\delta\mathcal{A}$	$-\delta\mathcal{S}$	$-\delta\mathcal{A}$
w_1	-0.0018919	0.001911	0.0018549	-0.002004
w_2	-0.0016448	0.001104	0.0016085	-0.001155
w_3	-0.0004899	0.001344	0.0004726	-0.001341
w_4	0.0006556	0.000264	-0.0006542	-0.000255
w_5	-0.0001228	0.000204	0.0001225	-0.000195
w_6	0.0000948	0.000054	0.0000957	-0.000045
w_7	0.0001911	-0.000396	-0.0001907	0.000402

The physics parameters Δm_d and τ_{B^0} uncertainties are included using the PDG average value. The impact on fit results is summarized as follows:

Table 5.10: systematic uncertainty from physics parameters

source	$+\delta\mathcal{S}$	$+\delta\mathcal{A}$	$-\delta\mathcal{S}$	$-\delta\mathcal{A}$
Δm_d	-0.001767	-0.000687	0.001778	0.000696
τ_{B^0}	-0.004561	-0.000546	0.004565	0.000555

The signal fraction is determined using 2D fit results of M_{bc} and ΔE from data. The impact on fit results is summarized as follows:

Table 5.11: systematic uncertainty from signal fraction

source	$+\delta\mathcal{S}$	$+\delta\mathcal{A}$	$-\delta\mathcal{S}$	$-\delta\mathcal{A}$
mu1_mbc	0.000822	-0.003888	-0.0007965	0.003849
sigma1_mbc	0.0004755	0.008442	-0.000628	-0.008733
m0_argus	-0.000707	0.00414	0.001448	-0.005781
c_argus	-0.005544	0.001449	0.000922	-0.000078
f1_de	0.0278255	0.020589	-0.0192365	-0.008409
f2_de	0.020809	0.017649	-0.0161285	-0.007005
mu1_de	-0.000443	-0.000153	0.0004955	0.000088
mu2_de	-0.000563	0.001446	0.0005905	-0.001446
mu3_de	-0.0031635	-0.000834	0.003354	0.000981
sigma1_de	-0.0001715	-0.000966	0.000206	0.000906
sigma2_de	-0.0031495	0.002958	0.0026345	-0.002475
sigma3_de	-0.001926	-0.00255	0.0024695	0.002985
a0_cheb	0.0009515	0.000057	-0.0008925	-0.000102
N_sig_f	-0.0046395	0.003987	0.004922	-0.003504

The fit bias uncertainties is determined by the fit error of 100k signal MC events, which is $\delta\mathcal{S} = 0.009817$ and $\delta\mathcal{A} = 0.005702$.

Table 5.12: systematic uncertainty from fit bias

source	$\delta\mathcal{S}$	$\delta\mathcal{A}$
fit bias	0.009817	0.005702

Applying KsFinder cut at 0.74 based on MC study may introduce small impact on data due to the different response on the classifier between data and MC. Therefore the contribution of systematic uncertainty from KsFinder is considered. At cut threshold 0.74, the R_B presenting MC and data signal yield ratio is $R_B = 1.027 \pm 0.033$,

where the up and low limit for MC correction is 1.06 and 0.994, respectively. These two ratios are applied on the signal fraction obtained by data to repeat the fit, and the difference of fit results compared to the original values are used as systematic uncertainty, see Table 5.13.

Table 5.13: systematic uncertainty from KsFinder.

source	$\delta\mathcal{S}$	$\delta\mathcal{A}$
$R_B = 1.06$	0.004826	-0.000606
$R_B = 0.994$	-0.000508	0.000007

For the contributions from vertex reconstruction, the impacts from the selections in Table 5.5 are considered. Given the fact that cut values in Table 5.5 are very loose and the statistics from data is very limited, the changing of these values doesn't affect events collected from data so that systematic uncertainty can not be reflected correctly. Therefore, 1 ab^{-1} generic MC is used with the modified ranges to estimate the potential systematic uncertainty from vertex reconstruction. Besides, due to the absence of IP constraint in vertex fit, the impact from the IP constraint options as well as the potential bias are not considered. The summarized systematic uncertainties are listed in Table 5.14.

Table 5.14: systematic uncertainty from vertex reconstruction

source	$\delta\mathcal{S}$	$\delta\mathcal{A}$
$\sigma_{z_{tag}} < 0.05 \text{ cm}$	0.004369	-0.003599
$\sigma_{z_{tag}} < 0.15 \text{ cm}$	0.000000	0.000000
$\chi_2/N(CP) < 3$	0.018197	-0.020242
$\chi_2/N(CP) < 13$	0.000000	0.000000
$\chi_2/N(tag) < 40$	0.000000	0.000000
$\chi_2/N(tag) < 60$	0.000000	0.000000
$ \Delta t < 50 \text{ ps}$	0.003325	-0.000396
$ \Delta t < 90 \text{ ps}$	0.000000	0.000000
IP constraint	0.000000	0.000000

Chapter 6

Conclusion and Prospect

The Belle II experiment is built upon the success of its predecessor Belle and many other great efforts of exploring the mysteries of flavor physics, which have expand our knowledge and understanding of elementary particle physics. One of the most outstanding outcome of these efforts is the Standard Model, which it's capable of well describing a variety of experimental results in a large energy scale and fine precision for the past few decades. And yet open questions that still draws attention from particle physicists remain, wait to be discovered as New Physics. One of the most important question is that why the universe is mass-dominated while anti-matter seems to be vanished.

Belle II is aimed to search for New Physics through the precise measurements of related topics in heavy flavor physics at the world-record luminosity frontier. SuperKEKB accelerator is designed with asymmetric beam energies to provide a boost to the center-of-mass system and thereby allow for time-dependent CP symmetry violation measurements. The products of collision is in a very clean environment, with 40 times higher luminosity of peak at Belle. This create excellent opportunities for physicists to look for the undiscovered source of CP violation, for which the existing explanation from the complex phase of CKM matrix can't described the observed level of asymmetry in our universe.

$b \rightarrow s$ transition is an important flavor coupling process to be examined in search for New Physics. The CP violation in such process was first observed after the

precise measurement in $b \rightarrow c$ with a small tension. So far the precision of the measurement of CP parameter \mathcal{S} in $b \rightarrow s$ is still in an arguable difference with tree-level process considering the existing uncertainty, which allows a decent margin for New Physics. The representative processes of $b \rightarrow s$ are resonant decay such as $B^0 \rightarrow \eta' K_S^0$, $B^0 \rightarrow \phi K_S^0$ and decay like $B^0 \rightarrow K_S^0 K_S^0 K_S^0$, on which Belle II experiment will have an excellent prospective sensitivity.

This thesis presents the first attempt to study the time-dependent CP violation in $B^0 \rightarrow K_S^0 K_S^0 K_S^0$ using early phase 3 data of Belle II and latest MC sample. In order to reconstruct clean signal sample of B^0 , K_S^0 reconstruction performance is critical because of the unique characteristics of this decay. A KsFinder based on FastBDT classification algorithm is developed to offer a goodness indicator of traditional cut-based reconstruction of K_S^0 . The performance of this new KsFinder is validated to have a great background rejection power at with small signal loss in the maximum FOM case. B^0 are reconstructed with a good significance even with very low statistics with a good agreement with MC prediction and Belle experience. The overall efficiency of B^0 is slightly improved than Belle with slightly higher beam background condition in current Belle II. The measurement of the CP fit is conducted based on the reconstruction. The CP fit using artificial model containing resolution functions from different sources are built with precise study of MC signal samples and the data sideband . As for flavor tagging information, wrong fraction as mandatory parameters in signal Δt distribution, are implemented too. The coefficient of signal and background in the CP fit model is determined by the signal extraction 2D fit over M_{bc} and ΔE . For each event, the signal fraction is calculated based on the M_{bc} and ΔE using the 2D fit model, which is used as a discrete observable in CP fit model.

Before performing CP fit on data, blind fit study and fit pull/linearity test are conducted to validate the fit model and procedures. In MC fit test, fit results for CP parameters are consistent with the generation level input. The linearity and fit pull test shows the reasonably good performance of extracting \mathcal{S} and \mathcal{A} . The validation of data using CP fitter to fit B^0 lifetime and mass width are also in a good agreement with PDG value in this low statistics case.

After the CP fit procedures are validated and the permission from Belle II collaboration of fitting on data is given, the CP parameters \mathcal{S} and \mathcal{A} measurement using Belle II early phase 3 data (2019 and 2020 Spring/Summer) is performed with the result as below:

$$\begin{aligned}\mathcal{S} &= -\sin(2\phi_1) = -0.82 \pm 0.85(stat) \pm 0.07(syst) \\ \mathcal{A} &= -0.21 \pm 0.28(stat) \pm 0.06(syst)\end{aligned}\tag{6.1}$$

The result is in a consistent with the PDG value and the prediction of the Standard Model, and also with the previous results from Belle and Babar as Chapter 1 described. The systematics study is also performed considered on the majority of contributing sources at this moment. The result is primary limited in precision due to the large statistical uncertainties from very low data collection.

What is worth of noticing is, many analysis tools that are required by performing the CP measurement on this channel is in a good stage of development. The decay mode being successfully re-discovered under very low data collection mostly thank to the newly developed K_S^0 classification software, KsFinder, which will also be an essential asset in neutral particles dominated channels like $B^0 \rightarrow K_S^0 K_S^0 K_S^0$. The Belle II experiment is crucial in these channels because of the cleaner background environment and better sensitivity compared with LHCb. Besides, an artificial model on the vertex resolution, or called Δt resolution has been finely studied using MC sample and sideband data. Several important dependence or behaviors of vertexing tools in the Belle II detector is understood to a good extension in the early phase of Belle II. Further, a new CP fitter which is based on these studies is built and being validated, which will provide a multi-functional analysis tool for Belle II time-dependent CP violation study in future.

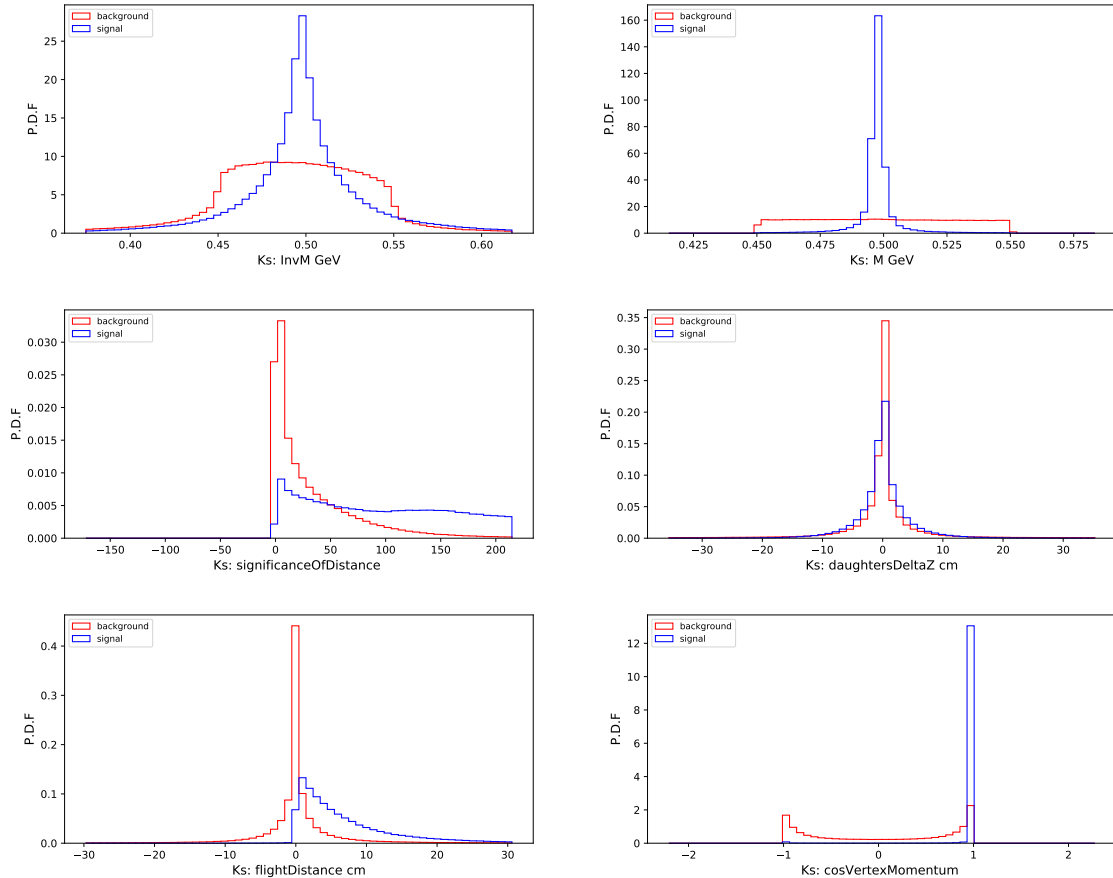
This study has shown a good potential of performing CP measurement in Belle II for the incoming years with more and more data recorded. The precision on \mathcal{S} in $b \rightarrow s$ penguin-modes is highly depending on the large luminosity as Fig 1-9 shows, which the current precision fits in the expectation. Along with the data collection

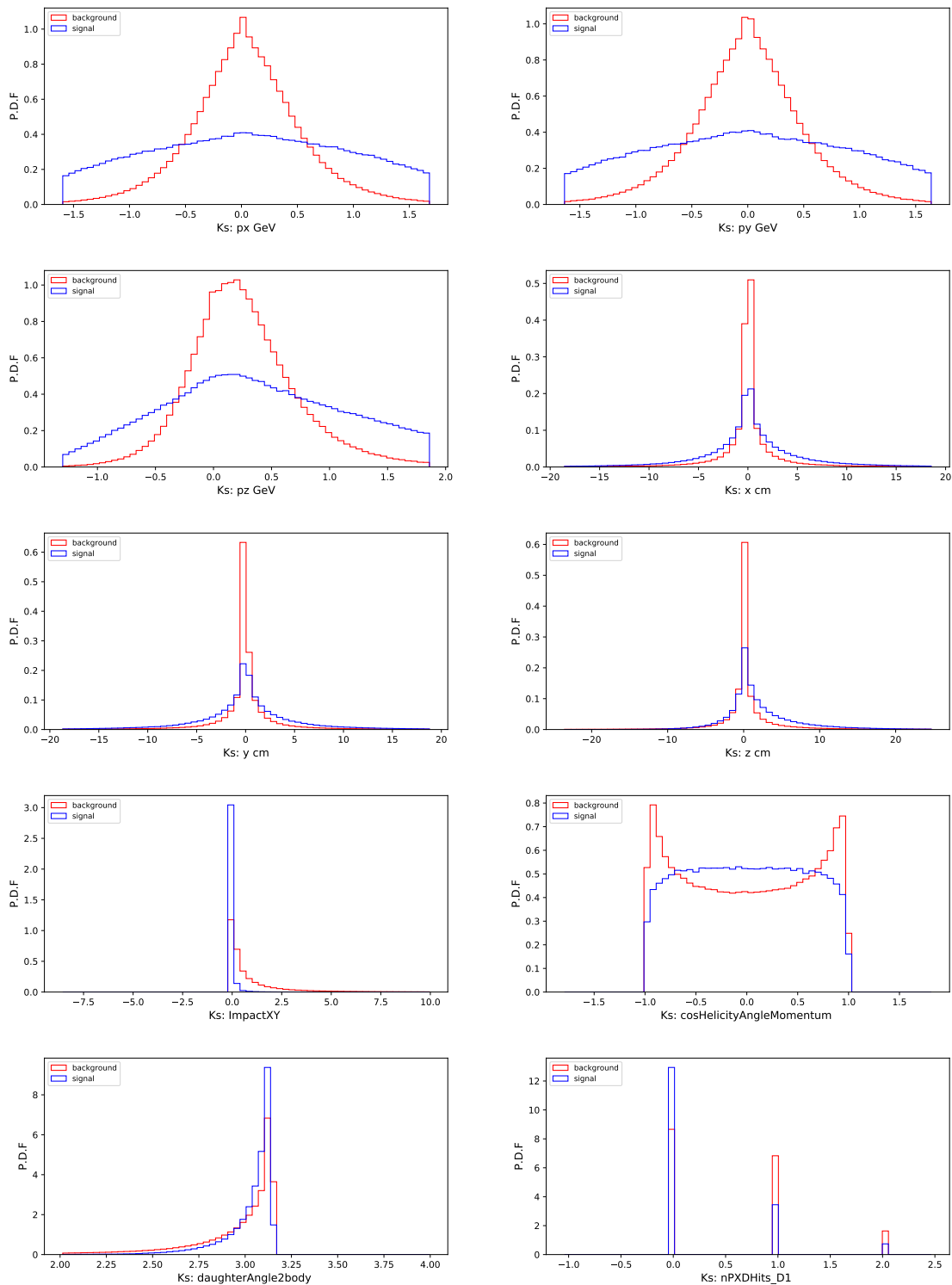
continues, we will be able to finely test and improve the analysis strategies and tools to a better stage using data, such as improving the reconstruction efficiency and purity of B^0 when the luminosity ramps up to much higher level with much higher backgrounds. At integral luminosity at 50 ab^{-1} level, the statistical uncertainty of this decay on $\Delta\mathcal{S}$ would be trimmed down to a comparable value around 0.03 which is close the Standard Model correction, offering a much better probe on whether New Physics is influential at this level of precision. The progress that has been made so far in this thesis paves a well-constructed and solid path towards future results. From the current result, the chance of having a much precised measurement in the next a few years on this channel is very promising and searching New Physics effect in penguin-mode $b \rightarrow s$ transition from Belle II is proven to be an exciting and important topic.

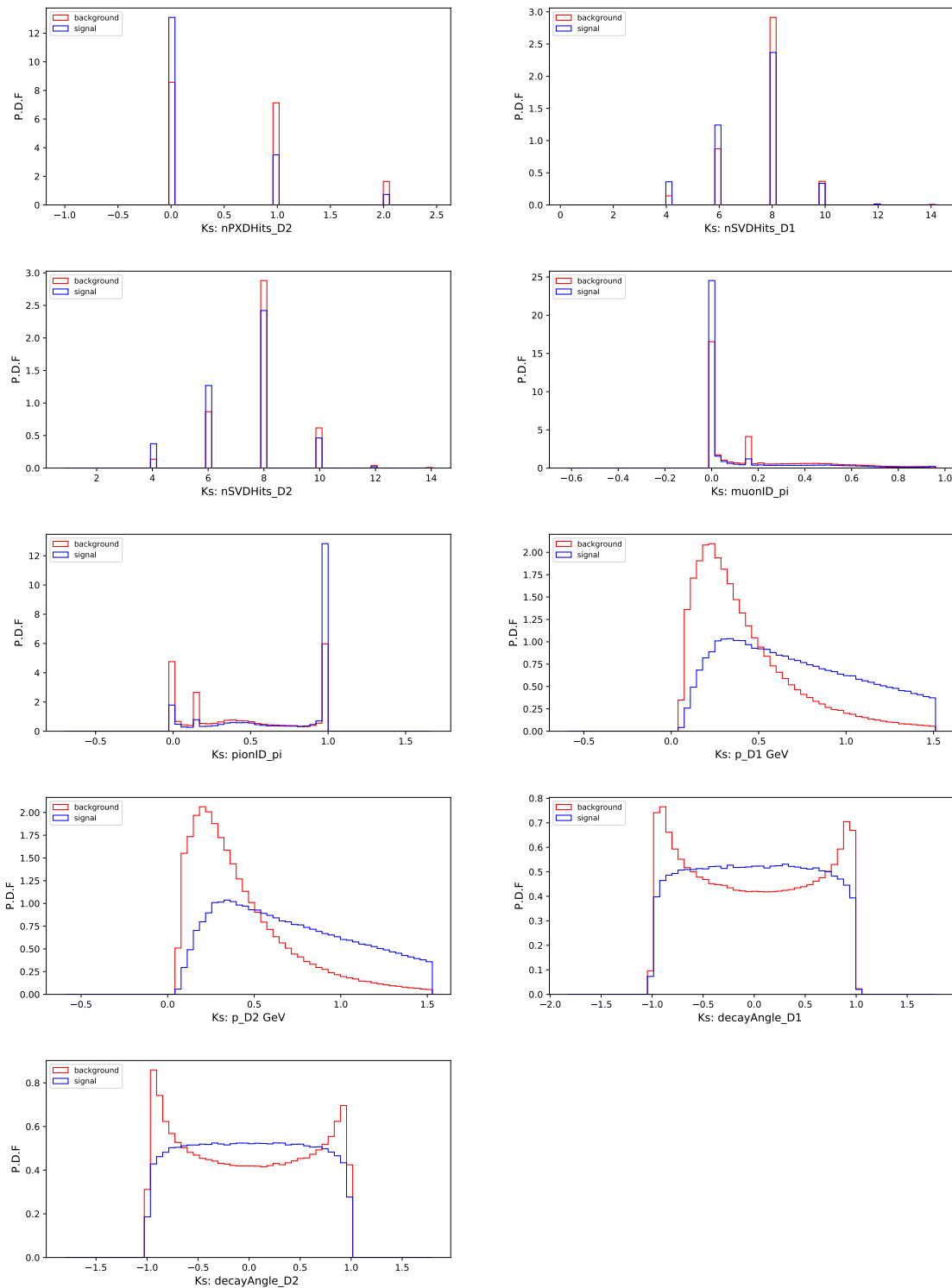
Appendix A

Training Observables for K_S^0 Classifier

Figure A-1: The distribution of input variables in signal MC for KsFinder. The red is the from fake K_S^0 and the blue is from true K_S^0



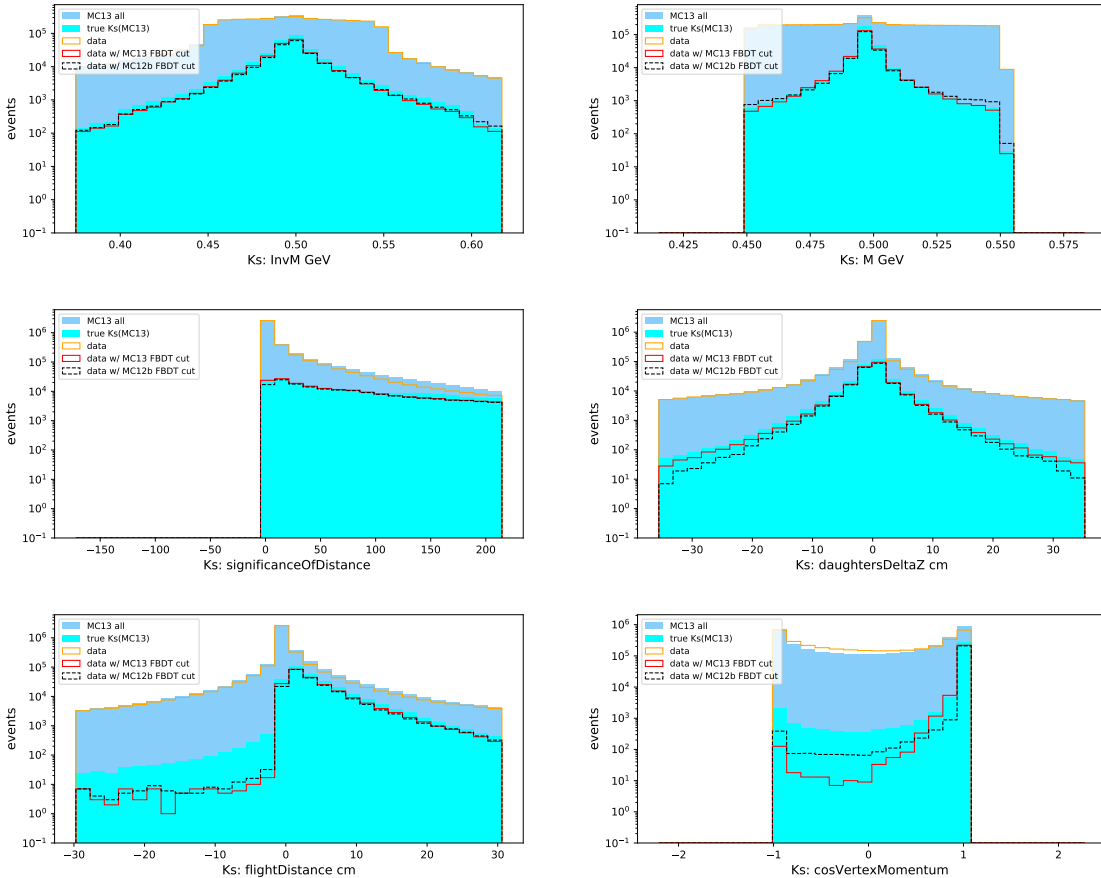


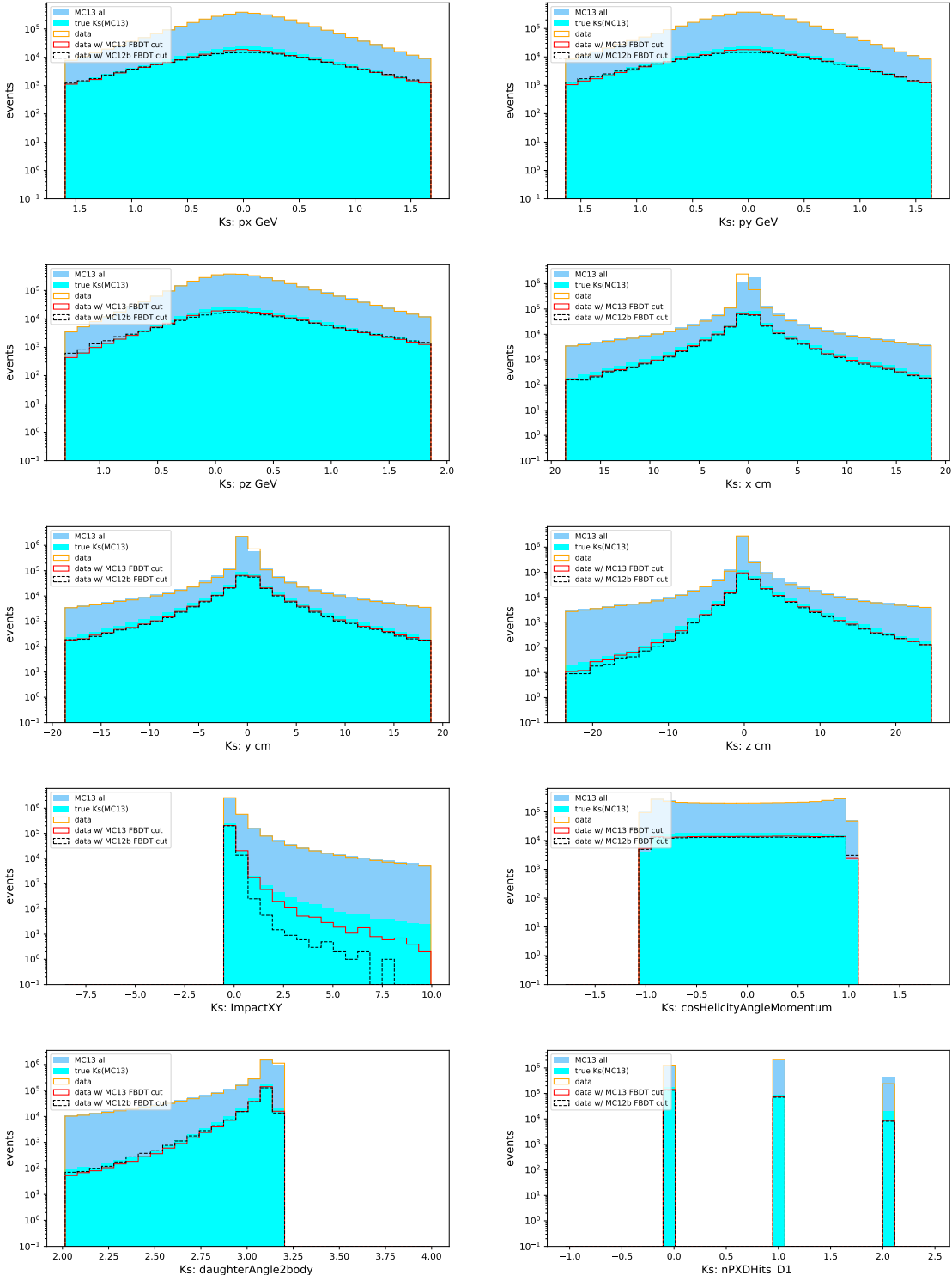


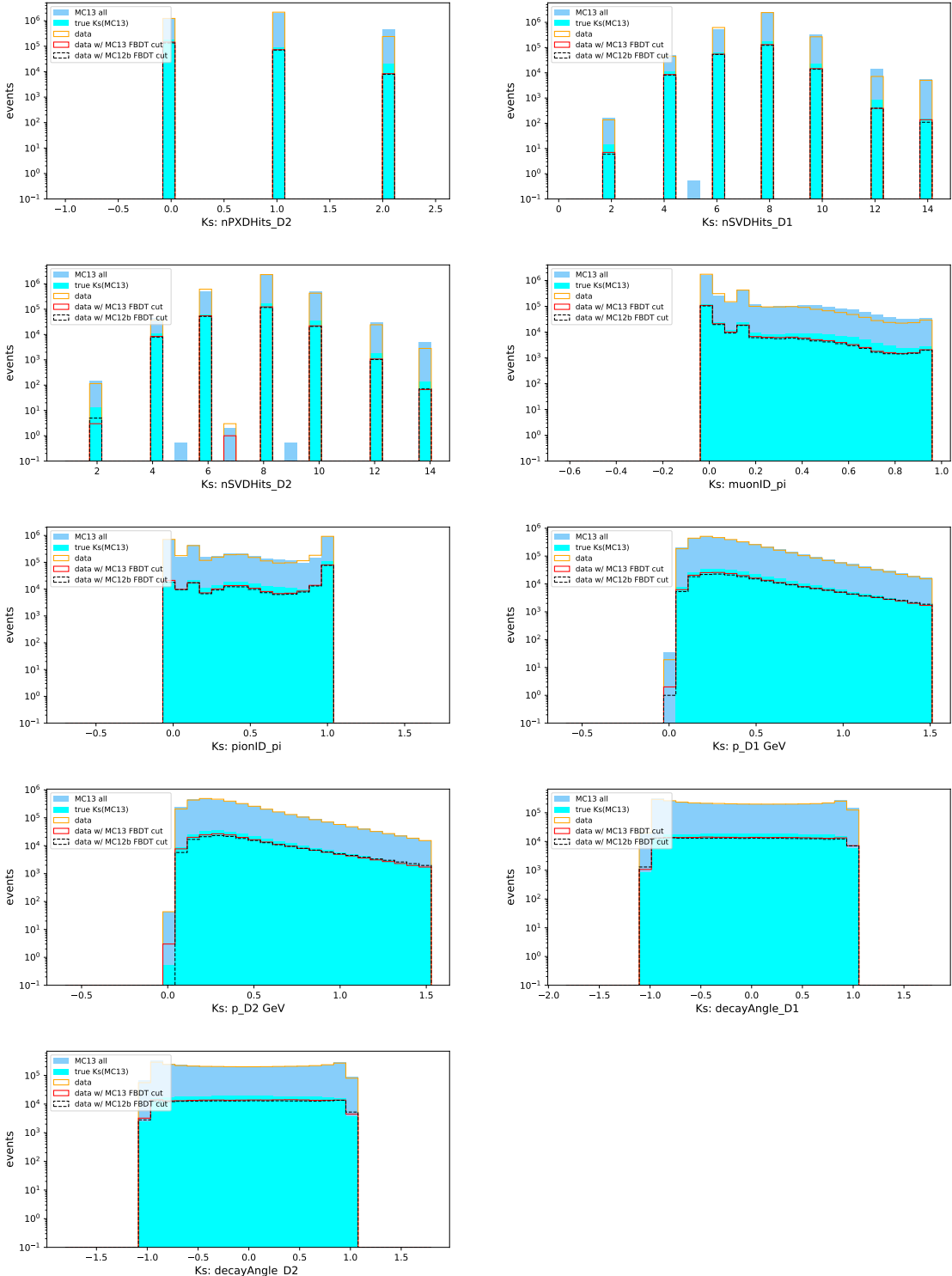
Appendix B

Data Validation Plots for K_S^0

Figure B-1: The distribution of variables used in KsFinder classification. The variables abbreviation can be referenced from Table III. The yellow solid lines are K_S^0 from data without KsFinder, and red solid lines are K_S^0 with KsFinder using MC13a for training. The black dashed lines are K_S^0 with KsFinder using MC12b (run-dependent). Blue histogram is from MC13a without KsFinder and cyan histogram is from MC13a with KsFinder.





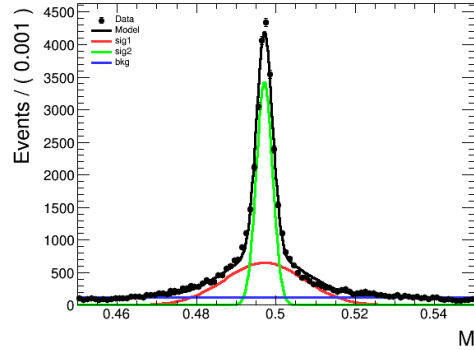


Appendix C

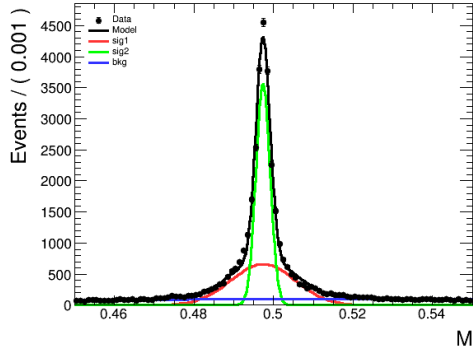
K_S^0 mass fit with varied cut value

Figure C-1: Double-gaussian shape and 1st-poly are used for fitting signal and background K_S^0 invariant mass under varies KsFinder cut values respectively. The data and MC are separately fitted to compared the yield in each cut, which defines the correction.

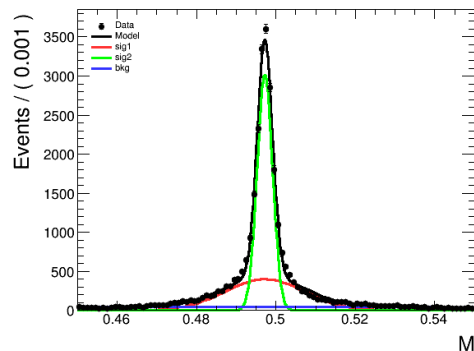
a) Data, cut=0.2



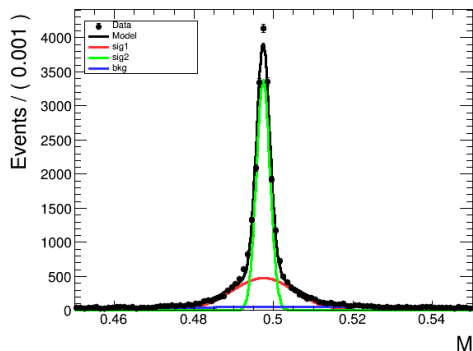
b) MC, cut=0.2



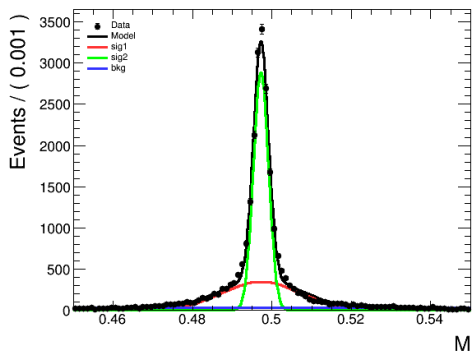
c) Data, cut=0.4



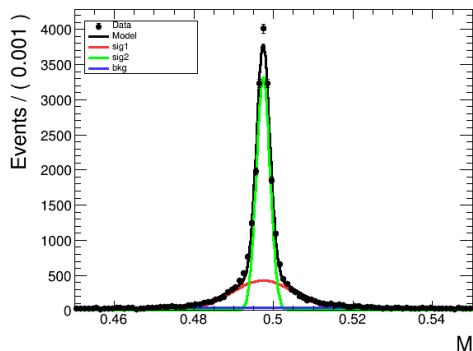
d) MC, cut=0.4



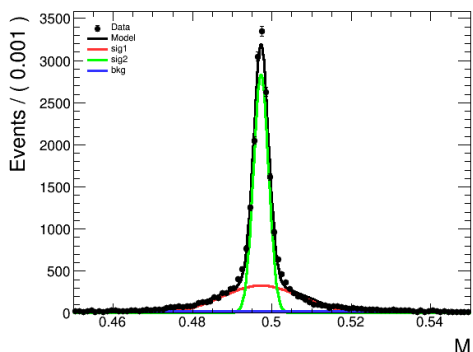
e) Data, cut=0.5



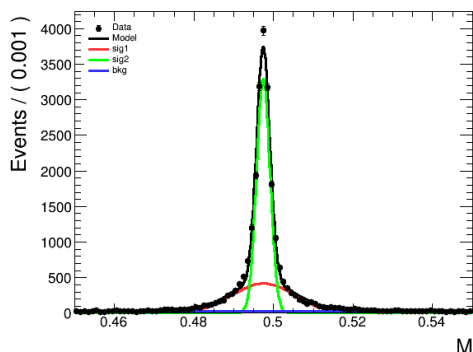
f) MC, cut=0.5



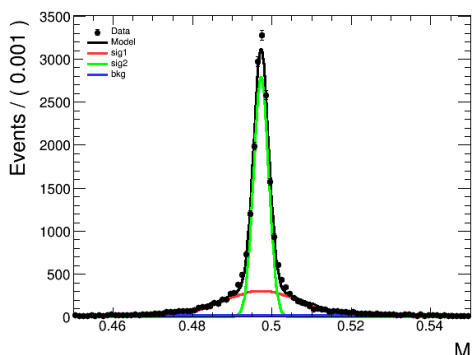
g) Data, cut=0.55



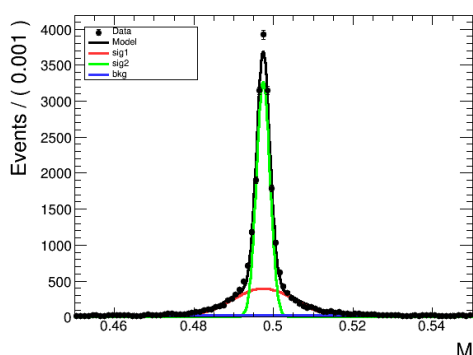
h) MC, cut=0.55



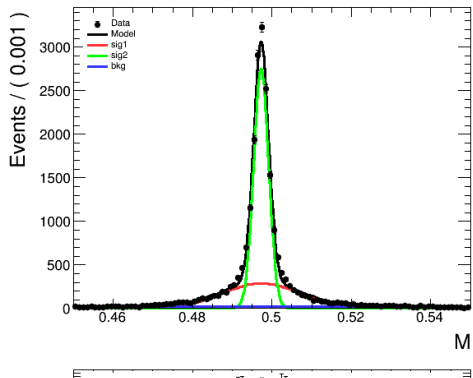
i) Data, cut=0.6



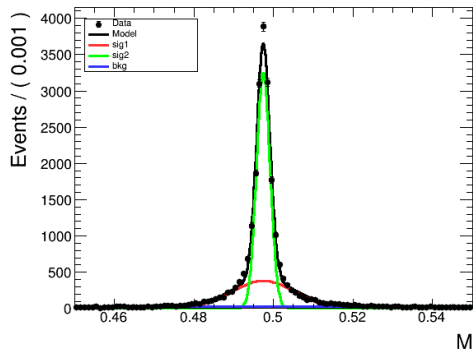
j) MC, cut=0.6



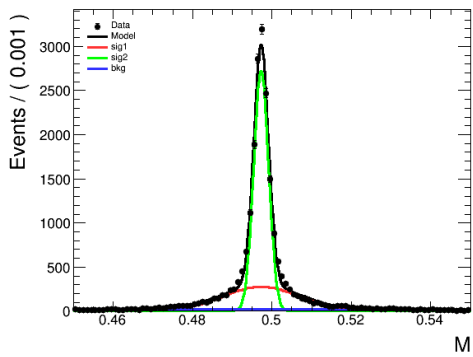
k) Data, cut=0.65



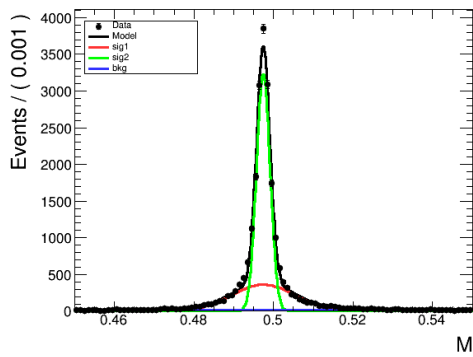
l) MC, cut=0.65



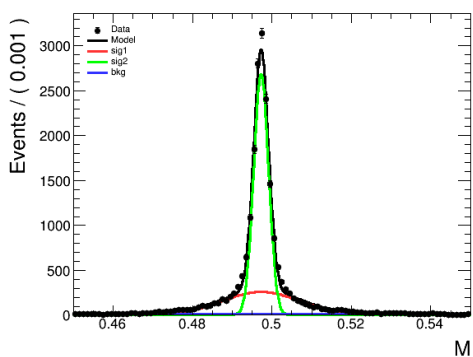
m) Data, cut=0.7



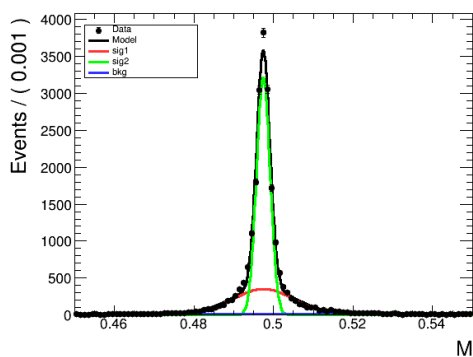
n) MC, cut=0.7



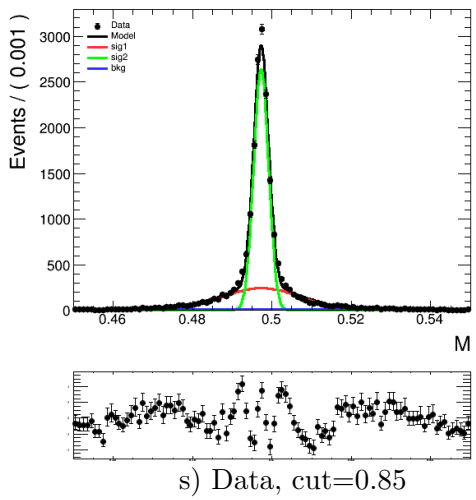
o) Data, cut=0.75



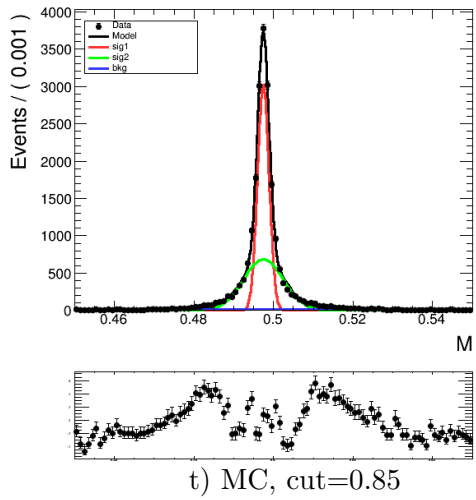
p) MC, cut=0.75



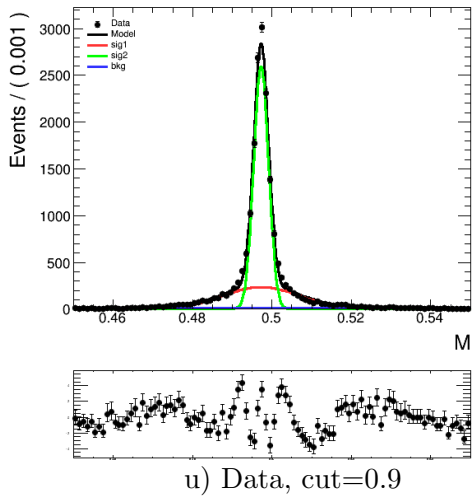
q) Data, cut=0.8



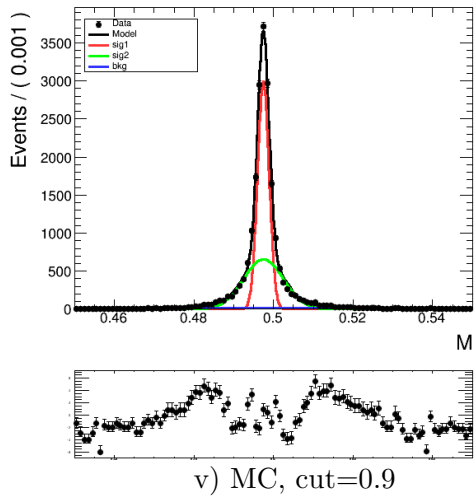
r) MC, cut=0.8



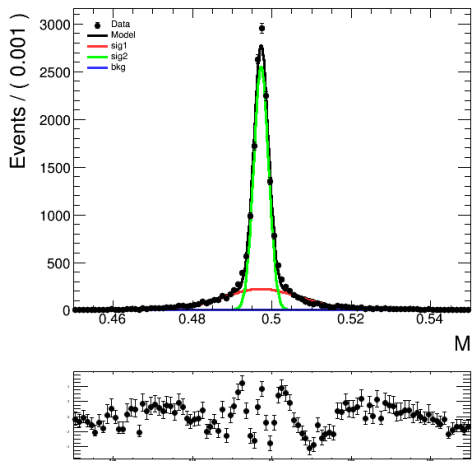
s) Data, cut=0.85



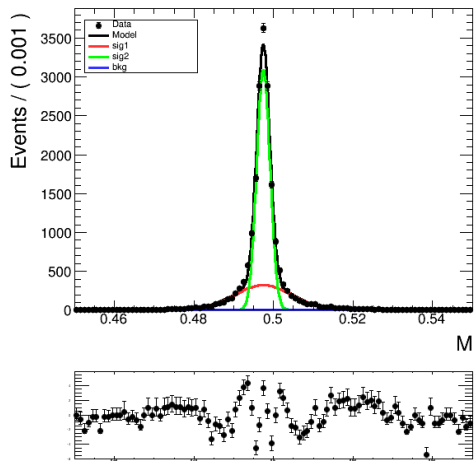
t) MC, cut=0.85



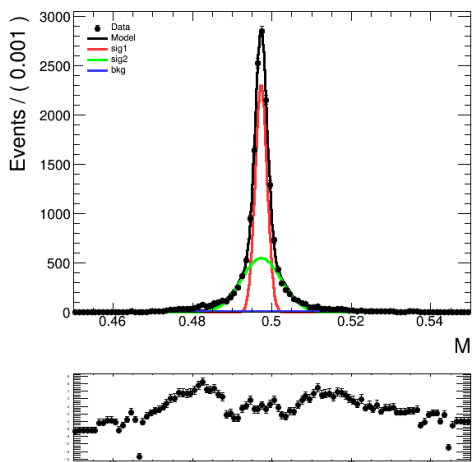
u) Data, cut=0.9



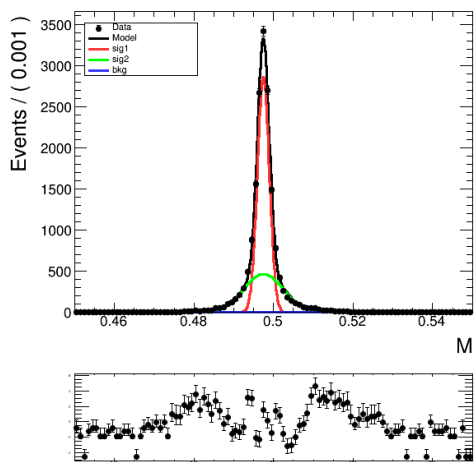
v) MC, cut=0.9



w) Data, cut=0.95



x) MC, cut=0.95



Appendix D

$2K_S^0$ invariant mass distribution

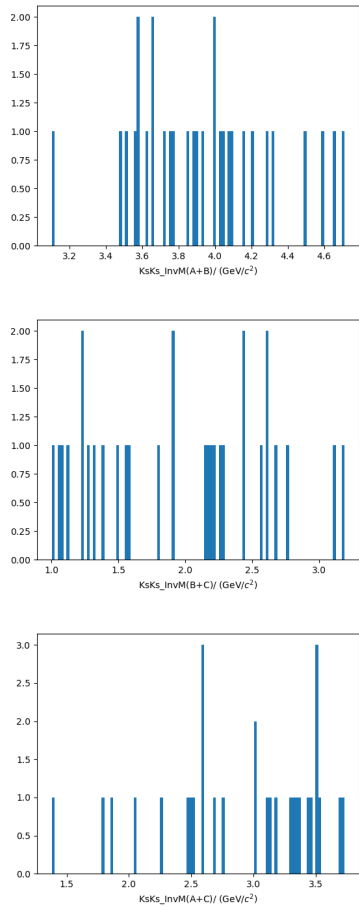


Figure D-1: Experiment data in signal region

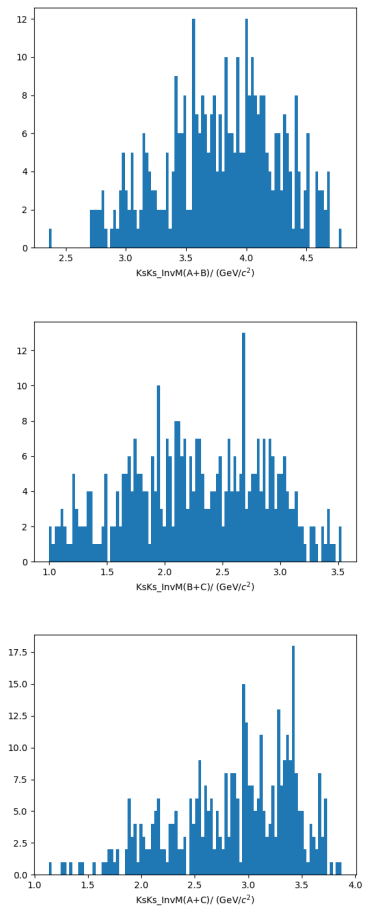


Figure D-2: Generic MC in signal region.

Bibliography

- [1] Georges Aad, Tatevik Abajyan, B Abbott, J Abdallah, S Abdel Khalek, Ahmed Ali Abdelalim, R Aben, B Abi, M Abolins, OS AbouZeid, et al. Observation of a new particle in the search for the standard model higgs boson with the atlas detector at the lhc. *Physics Letters B*, 716(1):1–29, 2012.
- [2] wikipedia. Elementary particles in the Standard Model. https://en.wikipedia.org/wiki/File:Standard_Model_of_Elementary_Particles_Anti.svg, 2012.
- [3] T. D. Lee and C. N. Yang. Question of parity conservation in weak interactions. *Phys. Rev.*, 104:254–258, Oct 1956. doi:10.1103/PhysRev.104.254. URL <https://link.aps.org/doi/10.1103/PhysRev.104.254>.
- [4] URL [https://commons.wikimedia.org/wiki/File:Parity_Violation_principle_Wu_experiment_\(English\).jpg](https://commons.wikimedia.org/wiki/File:ParityViolation_principle_Wu_experiment_(English).jpg).
- [5] James H Christenson, Jeremiah W Cronin, Val L Fitch, and René Turlay. Evidence for the 2π decay of the K^0 meson. *Physical Review Letters*, 13(4):138, 1964.
- [6] Makoto Kobayashi and Toshihide Maskawa. CP-Violation in the Renormalizable Theory of Weak Interaction. *Progress of Theoretical Physics*, 49(2):652–657, 02 1973. ISSN 0033-068X. doi:10.1143/PTP.49.652. URL <https://doi.org/10.1143/PTP.49.652>.
- [7] Yoshiki Teramoto. Cp violation in b physics at belle. 2002.
- [8] David Lange. Study of cp violation at babar.
- [9] Ikaros I Bigi, Valery A Khoze, NG Uraltsev, and AI Sanda. The question of cp noninvariance—as seen through the eyes of neutral beauty. In *CP Violation*, pages 175–248. World Scientific, 1989.
- [10] Marc Sher. Electroweak higgs potential and vacuum stability. *Physics Reports*, 179(5-6):273–418, 1989.
- [11] Augusto Ceccucci. The ckm quark-mixing matrix. 2008.

- [12] ckmfitter. Results of the global CKM fit in the large complex plane. http://ckmfitter.in2p3.fr/www/results/plots_summer19/ckm_res_summer19.html, 2019.
- [13] Amol Dighe, Tobias Hurth, Choong Sun Kim, and Tadashi Yoshikawa. The width difference of b_d mesons, 2001.
- [14] Julian Tarek Wishahi. *Measurement of CP Violation in $B^0 \rightarrow J/\psi K_S^0$ Decays with the LHCb Experiment*. PhD thesis, Dortmund U., 2014.
- [15] E Kou, P Urquijo, W Altmannshofer, F Beaujean, G Bell, M Beneke, I I Bigi, F Bishara, M Blanke, C Bobeth, and et al. The belle ii physics book. *Progress of Theoretical and Experimental Physics*, 2019(12), Dec 2019. ISSN 2050-3911. doi:10.1093/ptep/ptz106. URL <http://dx.doi.org/10.1093/ptep/ptz106>.
- [16] K-F Chen, K Hara, M Hazumi, T Higuchi, K Miyabayashi, Y Nakahama, K Sumisawa, O Tajima, Y Ushiroda, Y Yusa, et al. Observation of time-dependent cp violation in $b^0 \rightarrow \eta' k^0$ decays and improved measurements of cp asymmetries in $b^0 \rightarrow \varphi k^0$, $k_s k_s k_s$ and $b^0 \rightarrow j/\psi k^0$ decays. *Physical review letters*, 98(3):031802, 2007.
- [17] Tim Gershon and Masashi Hazumi. Time-dependent cp violation in $b^0 \rightarrow p_0 p_0 x_0$ decays. *Physics Letters B*, 596(3-4):163–172, 2004.
- [18] Martin Beneke. Corrections to $\sin(2\beta)$ from cp asymmetries in $b^0 \rightarrow (\pi^0, \rho^0, \eta, \eta', \omega, \phi) k^0$ decays. *Physics Letters B*, 620(3-4):143–150, 2005.
- [19] KH Kang, H Park, T Higuchi, K Miyabayashi, K Sumisawa, I Adachi, JK Ahn, H Aihara, S Al Said, DM Asner, et al. Measurement of time-dependent cp violation parameters in $b^0 \rightarrow k_s k_s k_s$ decays at belle. *arXiv preprint arXiv:2011.00793*, 2020.
- [20] J. P. Lees et al. Amplitude analysis and measurement of the time-dependent CP asymmetry of $B^0 \rightarrow K_S^0 K_S^0 K_S^0$ decays. *Phys. Rev. D*, 85:054023, 2012. doi:10.1103/PhysRevD.85.054023.
- [21] T. Abe et al. Belle II Technical Design Report. 2010. arXiv:1011.0352.
- [22] Giacomo De Pietro. First data at belle ii and dark sector physics. *arXiv preprint arXiv:1808.00776*, 2018.
- [23] Caitlin MacQueen, Belle II collaboration, et al. Dark sector physics at belle ii. In *Journal of Physics: Conference Series*, volume 1468, page 012047. IOP Publishing, 2020.
- [24] URL <https://root.cern/>.

- [25] T. Kuhr, C. Pulvermacher, M. Ritter, T. Hauth, and N. Braun. The belle ii core software. *Computing and Software for Big Science*, 3(1), Nov 2018. ISSN 2510-2044. doi:10.1007/s41781-018-0017-9. URL <http://dx.doi.org/10.1007/s41781-018-0017-9>.
- [26] URL <https://evtgen.hepforge.org/doc/models.html>.
- [27] Sea Agostinelli, John Allison, K al Amako, John Apostolakis, H Araujo, P Arce, M Asai, D Axen, S Banerjee, G 2 Barrand, et al. Geant4—a simulation toolkit. *Nuclear instruments and methods in physics research section A: Accelerators, Spectrometers, Detectors and Associated Equipment*, 506(3):250–303, 2003.
- [28] URL <https://pdglive.lbl.gov/Particle.action?init=0&node=S042&home=XXXX045>.
- [29] URL <https://confluence.desy.de/display/BI/Phase+3+luminosity+monitoring>.
- [30] J-F Krohn, F Tenchini, P Urquijo, F Abudinén, S Cunliffe, T Ferber, M Gelb, J Gemmler, P Goldenzweig, T Keck, et al. Global decay chain vertex fitting at belle ii. *Nuclear Instruments and Methods in Physics Research Section A: Accelerators, Spectrometers, Detectors and Associated Equipment*, 976:164269, 2020.
- [31] M Feindt and U Kerzel. The neurobayes neural network package. *Nuclear Instruments and Methods in Physics Research Section A: Accelerators, Spectrometers, Detectors and Associated Equipment*, 559(1):190–194, 2006.
- [32] Thomas Keck. Fastbdt: A speed-optimized and cache-friendly implementation of stochastic gradient-boosted decision trees for multivariate classification. *arXiv preprint arXiv:1609.06119*, 2016. URL <https://arxiv.org/pdf/1609.06119>.
- [33] L Breiman J Friedman RA Olshen and CJ Stone. Classification and regression trees. statistics/probability series, 1984.
- [34] Jerome H Friedman. Stochastic gradient boosting. *Computational statistics & data analysis*, 38(4):367–378, 2002.
- [35] Jerome H Friedman. Greedy function approximation: a gradient boosting machine. *Annals of statistics*, pages 1189–1232, 2001. URL https://projecteuclid.org/download/pdf_1/euclid-aos/1013203451.
- [36] Tenchini, Francesco and Krohn, Jo-Frederik. Decay chain reconstruction at belle ii. *EPJ Web Conf.*, 214:06023, 2019. doi:10.1051/epjconf/201921406023. URL <https://doi.org/10.1051/epjconf/201921406023>.
- [37] A. J. Bevan, B. Golob, Th. Mannel, S. Prell, B. D. Yabsley, H. Aihara, F. Annulati, N. Arnaud, T. Aushev, M. Beneke, and et al. The physics of the b factories. *The European Physical Journal C*, 74(11), Nov 2014. ISSN 1434-6052.

- doi:10.1140/epjc/s10052-014-3026-9. URL <http://dx.doi.org/10.1140/epjc/s10052-014-3026-9>.
- [38] *BELLE-II-NOTE-TE-2019-010* (2020). URL https://docs.belle2.org/record/1384/files/belle2-note-resol_belle.pdf.
- [39] URL <https://docs.belle2.org/record/1941/files/BELLE2-NOTE-PH-2020-027.pdf>.
- [40] H Tajima, H Aihara, T Higuchi, H Kawai, T Nakadaira, J Tanaka, T Tomura, M Yokoyama, M Hazumi, Y Sakai, et al. Proper-time resolution function for measurement of time evolution of b mesons at the kek b-factory. *Nuclear Instruments and Methods in Physics Research Section A: Accelerators, Spectrometers, Detectors and Associated Equipment*, 533(3):370–386, 2004.
- [41] URL https://docs.belle2.org/record/1905/files/BELLE2-NOTE-PH-2020-013_v3.2.pdf?version=1.